RATIONAL DESIGN OF PROTOCOLS FOR THE SHAPE-CONTROLLED SYNTHESIS OF PALLADIUM NANOCRYSTALS

A Dissertation
Presented to
The Academic Faculty

by

Legna M. Figueroa-Cosme

In Partial Fulfillment
of the Requirements for the Degree
of Doctor of Philosophy in the
School of Chemistry and Biochemistry

Georgia Institute of Technology
May 2018

RATIONAL DESIGN OF PROTOCOLS FOR THE SHAPE-CONTROLLED SYNTHESIS OF PALLADIUM NANOCRYSTALS

Approved by:

Prof. Younan Xia, Advisor
Department of Biomedical Engineering
Georgia Institute of Technology

Prof. Mostafa A. El-Sayed
School of Chemistry and Biochemistry
Georgia Institute of Technology

Prof. Angus P. Wilkinson
School of Chemistry and Biochemistry
Georgia Institute of Technology

Prof. Zhiqun Lin
School of Material Science and Engineering
Georgia Institute of Technology

Prof. Christopher W. Jones
School of Chemical and Biomolecular Engineering
Georgia Institute of Technology

Date Approved: March 7th, 2018

A todas las manos puertorriqueñas
que se levantan, resisten y trabajan para reconstruir la madre patria

ACKNOWLEDGEMENTS

At the culmination of my career as a doctoral student, I would like to express my deepest gratitude to all the people who have contributed to both my scientific and personal development. First, I would like to thank my thesis advisor, Prof. Younan Xia, for giving me the opportunity to be a graduate student in his research group. I am thankful for the tools he provided me to perform scientific research in a state-of-the-art laboratory, allowing me to do interesting science and work with highly qualified scientists.

To the members of my thesis committee: Prof. Angus Wilkinson, Prof. Christopher Jones, Prof. Mostafa El-Sayed, and Prof. Zhiqun Lin for offering their time to serve in my Ph.D. thesis committee.

To my coworkers and friends: Dr. Aleksey Ruditskiy for his friendship and unconditional help during graduate school, from assisting me in finding chemicals and training me with equipment, to giving me academic and moral support. To Dr. Xuan Yang for helping and teaching me how to operate the instruments for electrochemical characterizations. To Mrs. Jessica Shang for her friendship and excellent work as administrative personal in our laboratory. To Dr. Kyle Gilroy, Dr. Zach Hood, Dr. Thenner Rodrigues, Dr. Anderson da Silva, Dr. Robson da Silva, Mr. Chi-Ta Lee, and Dr. Madeline Vara for sharing their time, knowledge, and friendship with me.

To the staff members of the Materials Characterization Facilities at the Institute of Electronics and Nanotechnology, specially to Dr. David Tavakoli who trained and assisted me with the X-ray diffraction instruments, and to Mr. Todd Walters and Mr. Eric Woods for their constant help with the transmission electron microscope.

Also, I would like to thank the *Bill and Melinda Gates Foundation* for their support in the process of accomplishing my academic goals. In August 2008, I was awarded with the Gates Millennium Scholarship, which has since supported me financially throughout my entire education, starting from the bachelor up until now, ending with my doctoral degree. This invaluable financial support has taken care of a large portion of my registration and academic service fees, including book, housing, food, and transportation costs. In terms of the big picture, the Gates Foundation encouraged and made possible my representation as a Latino and woman working in the Sciences. Since I have no way of returning all the help they provided me, I commit myself to dedicate my time and efforts, whenever possible, to encourage and support the participation of minorities in the Sciences as I feel it is my duty to work towards the development of a scientific community that is more diverse and complete.

To my close friends: Mr. Juan C. Lebrón-Vázquez, Mr. Ricardo Cruz-Acuña, Mrs. Erika García, Mr. Angel Santiago-López, Mr. Arnaldo Negrón-Marty, and Mrs. Melanie Santos-Marrero for the endless support and happiness they brought to my life during good and bad days. Without them, I would have not completed this journey.

Last and most importantly, there are no words to express my gratitude to my father Mr. Luis C. Figueroa-Sánchez, my mother Mrs. Milagros Cosme-Borrás, and my sisters, Ms. Darinelys and Ms. Sharlene. I am thankful for their unconditional love, constant support, patience, advise, and words of encouragement during the past few years. Without them, I would have not finish graduate school, the most difficult personal challenge I have encountered so far in my life journey. They are and will always be the reason I keep moving forward.

AGRADECIMIENTOS

En la culminación de mi trayecto como estudiante doctoral quisiera expresar mi más sincera gratitud a todos los que han aportado a mi desarrollo como científico y ser humano. En primer lugar, quiero agradecer a mi tutor de tesis, el profesor Younan Xia, por permitirme ser alumna doctoral en su laboratorio de investigación. Agradezco las herramientas que me brindó para realizar investigación en un laboratorio de alta calidad y por permitirme trabajar con un equipo de científicos muy capaz. A los miembros de mi comité de tesis: Prof. Angus Wilkinson, Prof. Christopher Jones, Prof. Mostafa El-Sayed y Prof. Zhiqun Lin por su compromiso con la comunidad científica al regalar su tiempo para servir en mi comité de evaluación de grado.

A mis amigos y compañeros de laboratorio: Dr. Alex Ruditskiy, por su amistad y ayuda incondicional durante escuela graduada, desde mostrarme dónde estaban los reactivos para los experimentos, hasta el apoyo académico y emocional brindado durante el doctorado. Al Dr. Xuan Yang por ayudarme e instruirme con caracterizaciones electroquímicas. A la Srta. Jessica Shang por su amistad y excelente trabajo como personal administrativo de nuestro laboratorio. Al Dr. Kyle Gilroy, Dr. Zach Hood, Dr. Thenner Rodrigues, Dr. Anderson Silva, Dr. Robson Rosa da Silva, Sr. Chi Ta Lee y a la Dra. Madeline Vara por compartir su tiempo, conocimiento y amistad conmigo.

A los miembros del laboratorio de Caracterización de Nanomateriales en el Instituto de Electrónicos y Nanotecnología, muy en especial al Dr. David Tavakoli por entrenarme y asistir con el uso del instrumento de Difracción de Rayos-X, al Sr. Todd Walters y al Sr. Eric Woods por su ayuda con el Microscopio de Transmisión Electrónica.

Quisiera también agradecer a la fundación *Bill y Melinda Gates* por hacer posible una de mis metas académicas más importantes. En agosto de 2008 fui seleccionada para recibir la Beca Gates Millennium otorgada por la fundación *Bill y Melinda Gates*. Esta beca sostuvo económicamente mi carrera educativa desde el bachillerato hasta el doctorado, proveyendo año tras año ayuda financiera no solo para costos de registro y cuotas de servicios académicos, sino también para libros, vivienda, comida y transportación. En términos generales, la fundación Gates asistió e hizo posible mi representación como latino y mujer en el campo de las ciencias. Me comprometo con ellos a reciprocar su ayuda con servicio a la comunidad, en especial a grupos minoritarios, pues siento que es mi responsabilidad trabajar hacia el desarrollo de una comunidad científica más diversa y completa.

A mis amigos íntimos: Sr. Juan C. Lebrón-Vázquez, Sr. Ricardo Cruz, Srta. Erika García, Sr. Ángel Santiago-López, Sr. Arnaldo Negrón-Marty y a la Srta. Melanie Santos-Marrero por el apoyo y la alegría que dieron a mi vida durante los días buenos y malos. Sin ellos, no hubiese llegado al final de esta travesía.

Por último, no existen palabras suficientes para expresar mi más profundo agradecimiento hacia mi padre el Sr. Luis C. Figueroa-Sánchez, mi madre la Sra. Milagros Cosme-Borrás y a mis hermanas las Srtas. Darinelys y Sharlene. Agradezco el amor incondicional, el apoyo constante, la paciencia, los consejos y las palabras de aliento durante los pasados años. Sin ellos, no hubiese culminado éste, el reto personal más grande al que me he enfrentado en el trayecto de mi vida. Ellos fueron, son y siempre serán mi motivo de seguir adelante y cumplir mis sueños.

TABLE OF CONTENTS

LIST OF TABLES

LIST OF FIGURES

LIST OF SYMBOLS AND ABBREVIATIONS

DOS	density of states
LSPR	localized surface plasmon resonance
PEMFC	proton-exchange membrane fuel cell
PVP	poly(vinylpyrrolidone)
HCHO	formaldehyde
ICP-MS	inductively-coupled plasma mass spectrometry
TEM	transmission electron microscopy
CA	citric acid
ORR	oxygen reduction reaction
ECSA	electrochemical surface area
$j_{k,specific}$	specific activity
$j_{k,mass}$	mass activity
NaAsc	sodium Ascorbate
HAsc	ascorbic acid
HQ	hydroquinone
HAADF-STEM	high-angle annular dark-field scanning TEM
HRTEM	high-resolution transmission electron microscopy
XRD	X-ray diffraction
UV/vis	ultraviolet/visible
k	rate constant
E_a	activation energy

A	pre-exponential factor
ΔS_a	activation entropy
FA	formic acid
NIR	near infrared
TTEG	tetraethylene glycol
R_0	initial reduction rate
EG	ethylene glycol
LbL	layer-by-layer
XPS	X-ray photoelectron spectroscopy
EDX	energy-dispersive X-ray
FT	Fourier transform
E_{diff}	energy barrier to diffusion

SUMMARY

The utilization of noble metals extends far into our industrial and social structures since they are valuable in fields including investments, jewelry, medicine, catalysis, and more. Reducing the size and controlling the shape of noble metals to the nanoscale has proven to be a strategy that allows the efficient use of the metals while tailoring and even generating new features in their properties. This dissertation covers a number of strategies for controlling the size and shape of noble-metal nanocrystals, and scale-up approaches for the future commercial viability of these nanomaterials. I begin by introducing a simple and reliable method for the scalable production of Pd nanoplates. The success of my protocol relies on the use of hydroxylamine as a reductant, which allows for the nucleation and growth of well-defined nanoplates containing stalking faults. In the second project, I implement the use of dual reductants in an effort to program the reduction kinetics and regulate both, the nucleation and growth processes, to attain shape control of Pd nanocrystals. I proceed to explore a new concept based on geometric and stoichiometric analyses, to increase the production volume of a colloidal synthesis of Pd and Pd@Pt nanocrystals *via* seed-mediated growth. Finally, my coworkers and I report, for the first time, a facile synthesis of Ir nanocrystals with well-controlled facets. The essence of our approach was to coat an ultrathin, conformal shell of Ir on a Pd seed with a well-defined shape. In all, this work provides mechanistic insights on the nucleation and growth of noble-metal nanocrystals, enhances our understanding of the structure-property relationship, and propose scale up methods that could further improve the commercial viability of these nanomaterials.

CHAPTER 1

INTRODUCTION

1.1 Noble-Metal Nanocrystals and Their Applications

Noble metals are a special group of transition metals composed of ruthenium, rhodium, palladium, silver, osmium, iridium, platinum, and gold. These metals exhibit unique chemical and physical properties such as resistance to corrosion and oxidation, ductility, and malleability, and are among the rarest elements in the Earth's crust reaching the part-per-billion levels.[1] The utilization of such elements extends far into our industrial and social systems since they are vital for the smooth functioning of many enterprises, including the fields of investments, jewelry, medicine, energy, catalysis, electronics, and more.[2] The average market price per oz. for some noble metals fluctuates around $119 for Ruthenium, and $1380 for Rhodium (see Table 1.1).[3, 4] Due to their extremely low contents along with their high costs, it is of vital importance to develop strategies that enable the greatest utilization efficiency for these elements.

Table 1.1. Abundance of precious metals in the Earth's crust reported in parts-per-billion, and their current market price in USD per oz. of metal.

Precious Metal	Earth's Crust Content (ppb)[1]	Market Cost (USD per oz.)[3-4]
Ruthenium	1.0	$118.97
Platinum	5.0	$953.20
Iridium	1.0	$969.62
Palladium	15	$979.53
Gold	4.0	$1347.27
Rhodium	1.0	$1,379.59

1.1.1 From Bulk to Nano

Simply reducing the size of a metal to the nanoscale has proven to be an effective strategy that not only allows for efficient use of the material but more importantly, enables the control and generation of new features in the properties of the metal.[5-7] In general terms, metallic crystals can be described as an array of structurally packed atoms that donate one or more electrons to form a delocalized electron cloud.[8] When reducing at least one spatial dimension of the crystal to 1-100 nm, the physical barrier that confines the atoms, and so the electrons, becomes extremely influential in the energy bands of the metal. This change in the spatial dimensions transform the electron density of states (DOS) of the valence and conduction bands from continuous to discrete, thus changing the chemical and physical properties of the material.[5-9]

An example of this phenomenon can be found in gold. As a bulk material, gold exhibits a bright metallic yellow and it is considered the least reactive metal in the periodic table. However, when the size of gold crystals is reduced to the nanoscale, their chemical and physical properties change.[10] The interaction of light with gold nanocrystals induce the collective excitation of the conduction electrons, also known as a localized surface plasmon resonance (LSPR), and this produces distinctive colors anywhere from blue to red in the colloidal suspension.[10-12] As shown in Figure 1.1, the photon absorption depends on the size, shape, and composition of the gold nanocrystals. Moreover, light can also be scattered after interacting with the nanocrystals, and this can affect the overall color of the suspension. Both the light scattering and absorption are particularly useful in medical applications such as imaging and photothermal cancer treatment.[10,12]

Figure 1.1. Gold nanoparticles commonly applied in biomedical applications. (a) Gold nanorods, (b) silica–gold core–shell nanoparticles, and (c) gold nanocages. The different colors of these suspensions arise from the collective excitation of their conduction electrons, or localized surface plasmon resonance modes. The photon absorption varies with (a) aspect ratio, (b) shell thickness, and/or (c) galvanic displacement by gold. (Reprinted with permission from [10]. Copyright 2012 *Royal Society of Chemistry*)

In the field of heterogeneous catalysis, noble metals play a pivotal role in many industrially relevant reactions. For example, Pd is currently used in catalytic converters to assist the conversion of hazardous gases such as CO and NO into less harmful products such as CO_2 and N_2.[13,14] This metal is also used for catalyzing a myriad of organic reactions, including those involved in hydrogenation, dehydrogenation, and carbon-carbon bond formation (*e.g.*, Heck/Suzuki coupling), which are particularly useful in the pharmaceutical industry.[15-18]

Platinum on the other hand, is the most effective catalytic material for both the oxygen reduction and hydrogen oxidation reactions in a fuel cell.[19,20] This metal also serves as an excellent catalyst for the oxidation of small organic molecules such as formic acid and

ethanol,[21] production of nitric acid,[22] and refining of petroleum.[23] It is widely used for the decomposition of hydrogen peroxide,[24] hydrosilylation reactions, which are particularly useful in the silicone industry,[25] and it is the main catalyst in the automobile industry for catalytic converters.[26,27]

Other metals such as ruthenium, iridium, and rhodium have also been used as catalytic materials in many reactions. Iridium is particularly interesting for its ability to catalyze reactions such as selective hydrogenation of alkenes, aldehydes, unsaturated aldehydes, and ketones.[28-32] And it has been used in the reduction of imines to the corresponding amines, an important reaction in the pharmaceutical and agrochemical industries.[33] Ruthenium and Ru-based nanocrystals have demonstrated great catalytic performance towards reactions including aromatic hydrogenation, CO oxidation, ammonia synthesis, and CO_2 methanation.[34-38] And rhodium is used in the fabrication of three-way catalytic converters in automobiles, catalyzing both reduction and oxidation reactions.[39,40]

The reactions aforementioned, involve the interaction of reactant molecules with the surface of a catalyst. In a bulk crystal, the relative contribution of surface atoms is minimal, but when shrunk to the nanoscale, the surface-to-volume ratio increases so drastically that the relative participation of surface atoms becomes dominant and extremely valuable.[5,6] The use of nanocrystals in catalysis can potentially enhance the catalytic properties of the metal, allowing us to develop more efficient methods for the use of these precious metals.

1.1.2 Not Just Nano, but Nano Shaped

Experimental and theoretical studies have demonstrated that not only the size of a metal nanocrystal controls its properties, but the shape can also greatly affect its electronic,

optical, mechanical, and magnetic properties.[41-44] One of the pioneering studies that reported structure-function relationship was presented by El-Sayed and coworkers, in which they investigated the catalytic activity of Pt nanocrystals towards the electron-transfer reaction between hexacyanoferrate(III) and thiosulfate ions.[45] They found that the activation energy for this reaction increased in the order of tetrahedral > cubic > spherical Pt nanocrystals.[45] In another example, Liu and coworkers demonstrated that Pd octahedra enclosed by {111} facets were more efficient than Pd cubes enclosed by {100} facets for the aerobic oxidation of 5-hydroxymethyl-2-furfural.[46] Also, our group investigated the catalytic activity of Pd nanocrystals towards formic acid oxidation and demonstrated that {100} facets had substantially enhanced activity over {111} facets for single-crystal catalysts.[47] More importantly, it was shown that twin defects improve even further the activity of Pd nanocrystals for this reaction.[47] These examples made evident the clear relationship between the surface structure of noble-metal nanocrystals and their functionality.

1.2 Controlling the Shape, Size, and Composition of Nanocrystals

The formation of metal nanocrystals can be broadly divided into three major steps: (1) formation of fluctuating clusters of metal atoms and/or ions, (2) subsequent evolution of the metastable clusters into seeds, and (3) growth of the seeds into well-defined nanocrystals.[6] During the first stage of crystallization, metal atoms produced by the reduction or decomposition of a metal precursor nucleate to form a non-stable clusters of atoms and ions.[6] Once the cluster exceeds a critical size, the morphological fluctuations become highly unfavorable so the new phase is confined to a well-defined structure known

as seed.[6] Both the type of seed and its evolution determine the shape and facets exhibited by the final nanocrystals.[48] In the following sections, I would like to discuss the mechanistic insights regarding nucleation and growth, the formation of different crystal defect structures, as well as a case study based on palladium.

1.2.1 Fundamentals of Nucleation and Growth

The quest towards understanding the formation of colloidal nanoparticles was pioneered by LaMer and Dinegar during the 1950's.[49] They proposed a general nucleation theory after studying the synthesis of monodisperse sulfur colloids by treating $Na_2S_2O_2$ with HCl.[49,50] During the study, LaMer and Dinegar observed that the rate of nucleation was sensitive to the concentration of sulfur in the solution.[49] The observations they made during this study have been generalized and used to partially explain the nucleation of metal nanocrystals.[6,50] In a typical synthesis, a metal precursor is reduced or decomposed to generate metal atoms. Once the concentration of atoms reaches supersaturation, they undergo homogeneous nucleation to form fluctuating clusters or nuclei. As the nuclei form, the concentration of atoms rapidly decreases below supersaturation, preventing the formation of more nuclei. Despite the lowered atom concentration, the barrier to heterogeneous nucleation support seed-mediated growth where atoms are added to the nuclei and/or seeds.[6, 50]

The seeds can exhibit different internal defect structures such as single-crystal, singly twinned, multiply twinned, and stacking-fault-lined, all which can evolve into nanocrystals with different shapes (see Figures 1.2 and 1.3).[6,48,50,51] For example, single-crystal seeds can evolve into cubes, cuboctahedra, or octahedra depending on the

relative growth rates of the facets.[48] To ultimately obtain a narrow distribution for the shapes of nanocrystals, one must control the population of the different seeds formed during nucleation. But, how to control the formation of seeds with a specific internal defect structure? The answer lies between the principles of thermodynamics and kinetics.

In a system driven entirely by thermodynamics, the most favored structures are the ones that minimize the total free energy of the nanocrystal.[50] The classical nucleation theory, developed by Gibbs, establishes that the free energy associated with nucleation depends on two variables: a volume term, and a surface area term.[50,52] For single-crystal seeds in vacuum, the structure formed is a truncated octahedron known as Wulff shape, a nanocrystal with a quasi-spherical profile that minimizes its energy by including both {100} and {111} facets.[6,50] However, theoretical calculations, and later on experimental evidence, demonstrated that the thermodynamically stable shape will depend on the overall size (technically speaking, the number of atoms in the structure).[50] For example, at small particle size, the predominant shape is icosahedra. As the particle size increases, one can obtain decahedra and single-crystals (Figure 1.2A). Gilroy and coworkers showed experimentally that the presence of twin structures in Ag nanocrystals could be controlled by heating and subsequent cooling nanoparticles of different sizes until they reach thermodynamic equilibrium.[53] Icosahedral, decahedral, and single-crystal structures were observed when the size of the nanoparticles increased form below 7 nm, to 7-11 nm, and above 11 nm, respectively.[53]

On the other hand, experimental studies have demonstrated that the formation of seeds with different internal defect structures can be controlled using kinetics.[51,54,55] Simply, by tuning the initial reduction rate of a precursor, one can manipulate the number

of twin defects formed in a seed. When the initial reduction rate varies from fast, to moderate, and slow, nanocrystals with single-crystal, multiply twinned, and stacking fault-lined structures, are formed correspondingly (Figure 1.2B).[51]

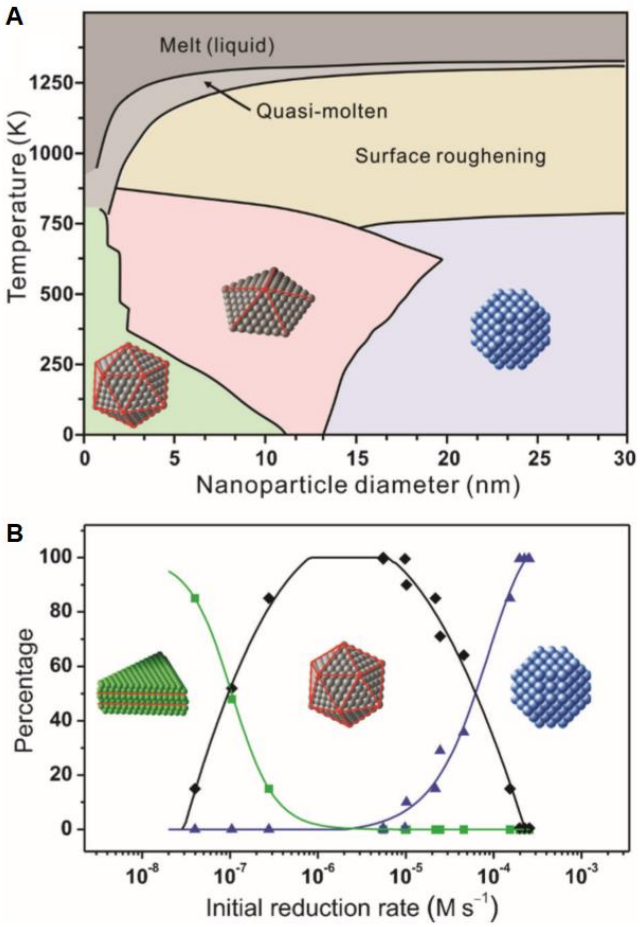

Figure 1.2. (A) Phase diagram for Au nanocrystals as a function of size and temperature. (B) Plot displaying the percentage of plate-like (green curve), icosahedral (black curve), and single-crystal (blue curve) seeds formed as a function of the initial reduction rate. (Reprinted with permission from [50]. Copyright 2017 *Wiley-VCH*)

Once the seeds are formed, they can further participate in heterogeneous nucleation for the newly formed atoms to produce nanocrystals with distinctive shapes or facets. One of the most important factors determining the type of facet (therefore the shape) of a nanocrystal is the relative rates at which different crystal planes grow.[6] In a sense, slow

growing facets will dominate at the expense of the faster growing ones.[6] Such dynamic evolution is often responsible for the formation of nanocrystals with different geometries as presented in Figure 1.3.[6,48]

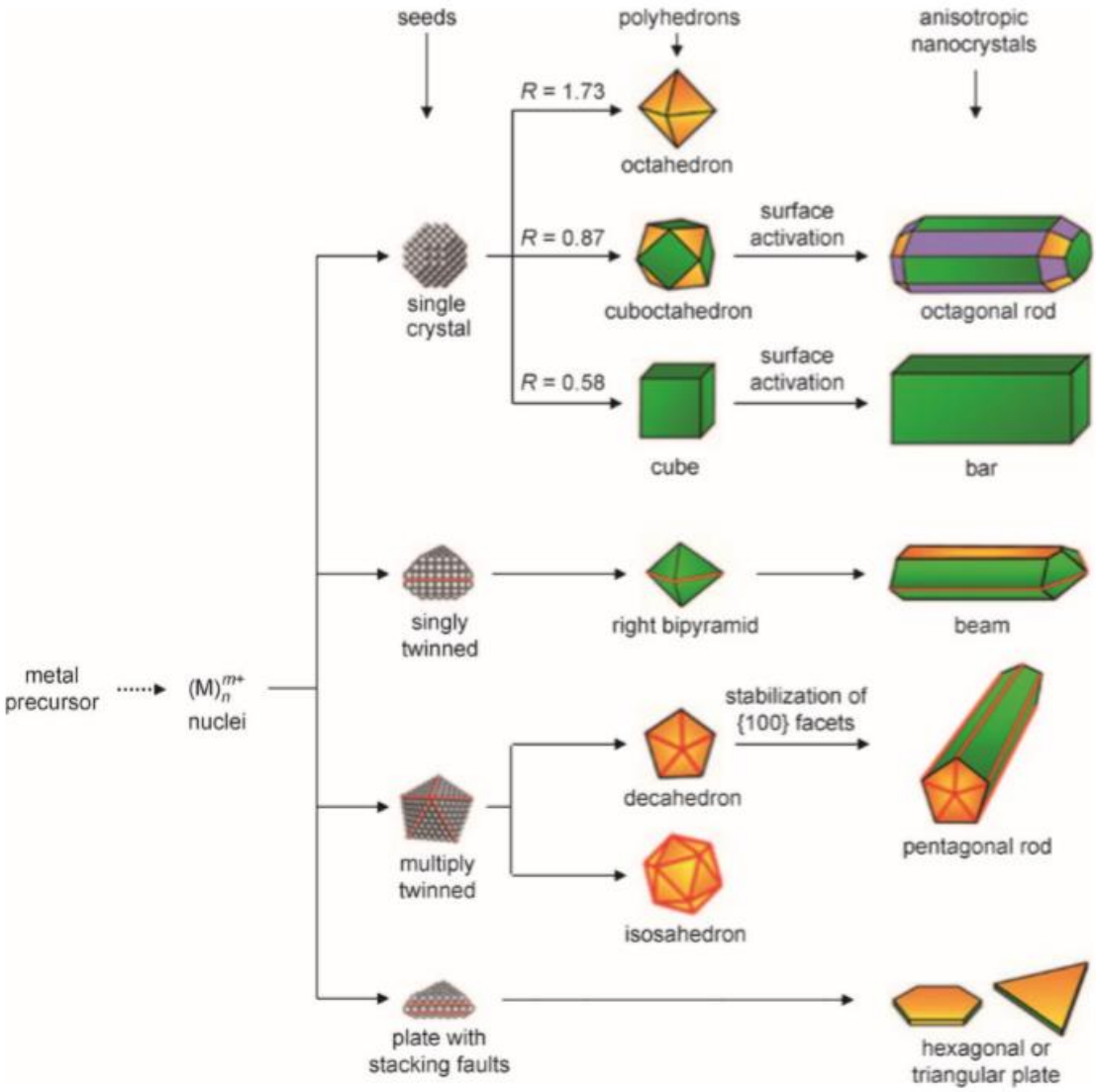

Figure 1.3. Reaction pathways that lead to fcc metal nanocrystals having different shapes. First, a precursor is reduced or decomposed to form the nuclei (small clusters). Once the nuclei have grown past a certain size, they become seeds with a single-crystal, singly twinned, or multiply twinned structure. If stacking faults are introduced, then plate-like seeds will be formed. The green, orange, and purple colors represent the {100}, {111}, and {110} facets, respectively. Twin planes are delineated in the drawing with red lines. The parameter R is defined as the ratio between the growth rates along the [100] and [111] directions. (Reprinted with permission from [48]. Copyright 2007 *Wiley-VCH*).

One way to change the relative grow rate of the facets is to alter their specific surface free energies by introducing ionic species, small molecules, or macromolecules that can selectively bind to different facets.[6] When introducing these species into a reaction solution, the capped facet will be more stable, thus taking a lower specific surface free energy. In other words, the capped surface will take a slower growth rate and consequently a greater proportion on the surface, leading to the formation of a shape with the facet preferentially expressed.[6] Poly(vinyl pyrrolidone) (PVP) is often used for as both capping agent and stabilizer of the Ag and Pd {100} facets. Other capping agents include: bromide and chlorine ions for the Pd {100} facets, and citric acid for the {111}.[56,57,58]

It is important to point out that tuning the reaction kinetics and reduction rates it is a complicated process. In a typical synthesis, the aforementioned surfactants and capping agents are present in the solution along with the metal precursor complexes.[54,59,60] These molecules, as well as the solvent, could undergo ligand exchange with the precursor, influencing the kinetics of reaction.[59,61] It is well known that metal precursors in water hydrolyze to create metal complexes with different stability.[59,61] For example, an aqueous solution of the Pd(II) complex $PdBr_4^{2-}$ and $PdCl_4^{2-}$ will produce different hydrolyzed compounds with the respective general form of $[PdBr_n(H_2O)_{4-n}]^{2-n}$ and $[PdCl_n(H_2O)_{4-n}]^{2-n}$ ($n \leq 4$).[59,61] The stability of both complexes, therefore their relative degree of hydrolysis and reduction potential are very different. For instance, it was demonstrated that Pd(II) complexes based on Br^- and Cl^- undergo different kinetic pathways to produce nanocrystals with different shapes.[54,62]

The mechanism of electron transfer also plays an important role in determining the rate of reaction. Marcus theory suggests that for processes involving a redox reaction, factors such as Coulombic interactions between the ionic reactants and the solvation of the ions, affect the rate of reaction.[63-65] Equally important, reduction pathways can determine the rate of reaction. For example, reduction may occur in solution or on the surface of a pre-formed seed.[54,55,66-68] As discussed by Watzky and Finke, autocatalytic reduction influences the kinetics of formation of a metal cluster.[66,67] Our group quantitatively analyzed the kinetics of autocatalytic surface reduction in the process of controlling the evolution of nanocrystals into predictable shapes. [68] As presented in Figure 1.4, our kinetic measurements demonstrated that the activation energy barrier to autocatalytic surface reduction was highly dependent on both the type of facet and the presence of twin boundaries, leading to distinctive growth patterns and products.[68]

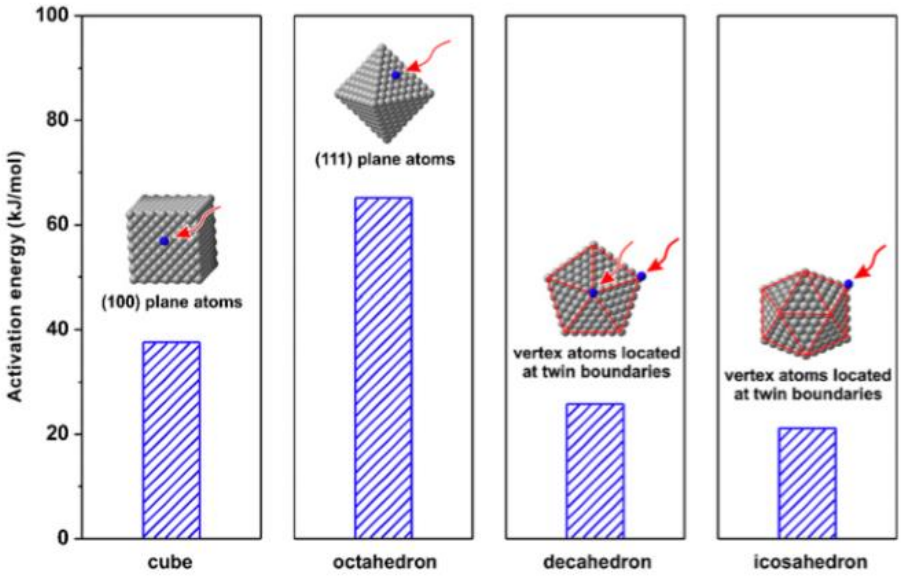

Figure 1.4. Comparison of the activation energy (Ea) for autocatalytic surface reduction on Pd seeds with different but well-defined facets and twin structures. (Insets) Preferential sites for the nucleation and deposition of Pd atoms through autocatalytic surface reduction, in which the precursor adsorbs onto these sites, followed by chemical reduction to atoms for their incorporation into the surface layer of the seed. (Reprinted with permission from [67]. Copyright 2017 *National Academy of Science*)

It is through kinetic control that one can attain structures thermodynamically non-favorable.[68] Figure 1.5 shows an illustration that has been used in literature to explain the concept of thermodynamic *versus* kinetic control. The global minimum in the Gibbs free energy represents the most stable product (thermodynamically controlled).[68] As aforementioned, single-crystal seeds in vacuum form a Wulf polyhedron.[6,68] However, when the synthesis is conducted under kinetically controlled conditions, the product could be trapped in states (or shapes) corresponding to a local minimum, allowing for the dominance of less stable shapes.[68] Contrary to a thermodynamic control which only focus on the final state rather than the process, kinetic control is all about the exact progression of reaction which allows one to manipulate experimental conditions to generate different non-stable products.[68]

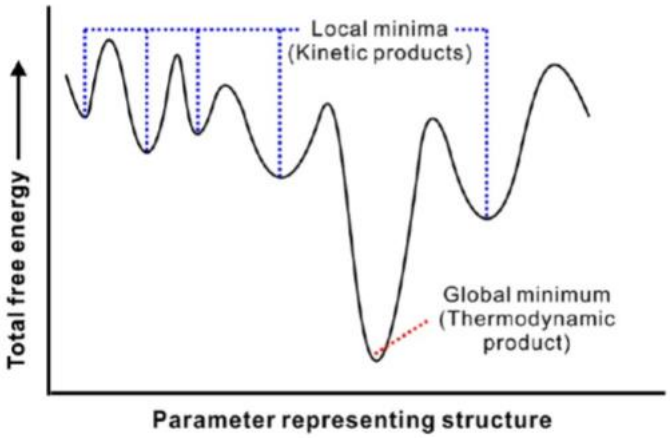

Figure 1.5. Schematic illustrations of two different scenarios of thermodynamic versus kinetic control that involve sequential reactions. The thermodynamic product, the one at global minimum, could be most conveniently accessed by raising the reaction temperature. (Reprinted with permission from [68]. Copyright 2015 *American Chemical Society*.)

1.2.2. The Case of Nanoplates

Crystals with a close-packed lattice can experience a disruption in the stacking sequence of atomic layers, generating two common types of crystal defects: (1) a stacking

fault, and (2) a twin region.[69] For example, stacking faults can be formed when the stacking sequence of a cubic-close-packed lattice (*e.g.* ABCABCABC) is changed by removing or adding a layer (*e.g.* ABCABABC).[6,50] In terms of the energy associated with these defects, the stacking fault correlates positively with twin-boundary energy.[50]

Interestingly, the formation of seeds that contain stacking faults (*e.g.*, nanoplates) is not favored under thermodynamics at any size due to the high surface energy.[50] In general, synthesis of nanoplates requires a kinetically controlled process that has been achieved by decreasing the reduction rate through the use of weak reductants such as citrate and PVP, or by slowly injecting the metal precursor (*e.g.*, using a syringe pump at low pumping rates). Also, one could intentionally use metal complexes with strong ligands such that the reduction kinetics is slow enough to allow the formation and growth of stalking faulted structures.[70-74]

Determining the exact mechanism of formation for such defects remain to be a grand challenge for nanochemists and nanomaterial scientists. It has been proposed that stacking faults formed at the early stages of a reaction are the underline event for the formation of nanoplates.[50, 73] Since the formation of nuclei is extremely difficult to observe in real space due to the lack of experimental tools with the capability of resolving at such a small scale, we rely on kinetic studies along with simulations to understand this complicated mechanism of formation.[6]

1.2.3 Seed-Mediated Growth and Pd@M Bimetallic Nanocrystals

Wet-chemical methods that are used to control the shape of nanocrystals have traditionally focused on the reduction of a metal precursor by a reductant in the presence

of a capping agent and/or colloidal stabilizer. In such syntheses, homogeneous nucleation and growth occur simultaneously, which in some cases represent a limitation because the reduction kinetics necessary for controlling nucleation is different from what is needed to direct the shape evolution during a growth process.[50,75,76] This drawback can lead to the formation of polydispersed nanocrystals in terms of size and shape, as well as the presence of structures with different crystallinity or internal defect structure within the same synthesis.[50] To mitigate this issue, many groups have adopted the seed-mediated route, an attractive approach that allows to circumvent the complicated and poorly understood nucleation step. The hallmark of seed-mediated growth is the utilization of pre-formed seeds as nucleation sites for the deposition of newly formed atoms.[50] An example is presented in the use of Pd nanocubes as seeds for the heterogeneous nucleation of the newly formed Pd atoms and thus the formation of Pd octahedra.[75-77]

One of the advantages of the seed-mediated approach is the ability to control the structure of different metals through the replication of a seed surface.[50, 78-81] Seeds can be used to deposit a specific number of atomic layers of another metal, which not only provides an ideal route to control the amount of material used in synthesis, but it could potentially avoid the waste of precious metals. A good example can be found in the preparation of Pt-based nanocrystals using palladium as seed for the deposition of Pt atoms to generate Pd@Pt_{nL} (where L = atomic layers). Xia and coworkers, have successfully prepare Pd@Pt_{nL} nanocubes, octahedra, decahedra, and icosahedra (Figure 1.6 A-D).[78-81] All these syntheses uses slow injection of a Pt precursor into a solution held at high temperatures (approximately 200 °C) so that the deposition and diffusion rates of the adatoms onto the seed surface can produce conformal layers of Pt atoms.[82] All protocols

are based polyol reduction, (usually EG or DEG) and involve the use of Pd seeds, capping agents, and colloidal stabilizers. The thickness of the Pt shells could be readily controlled by regulating the amount of Pt precursor introduced into the system.[78-81]

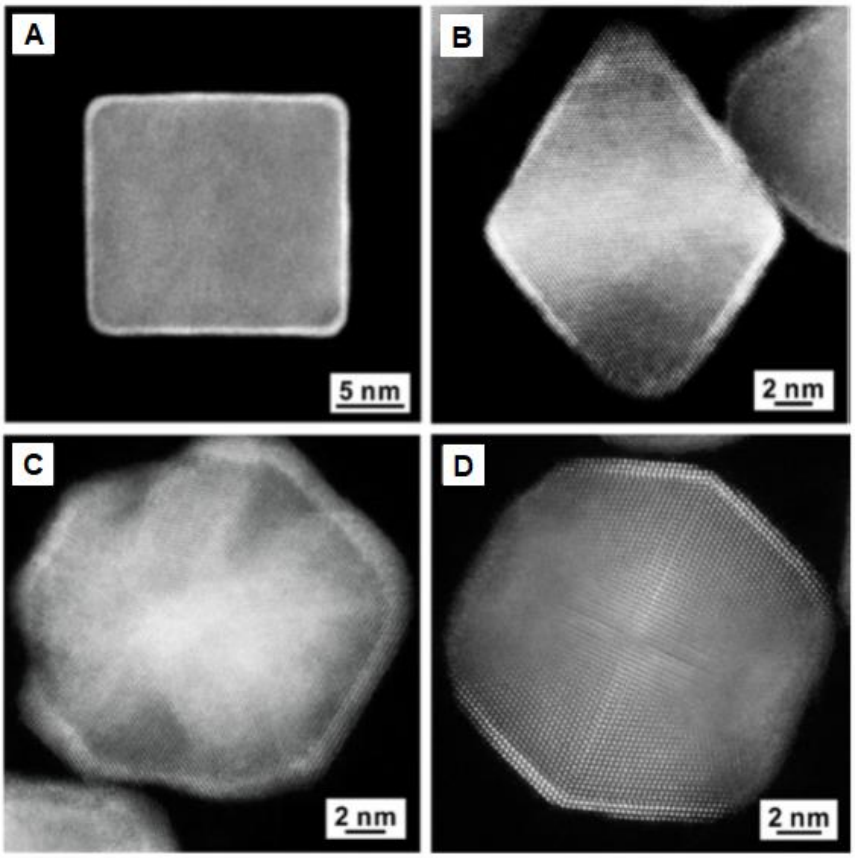

Figure 1.6. HAADF-STEM images of Pd@PtnL (n =1 −6) nanocrystals with different shapes: (A) cubic, (B) octahedral, (C) decahedral, and (E) icosahedral. (Reprinted with permission from [50]. Copyright 2017 *Wiley-VCH*.)

1.3 Towards the Industrial Production of Shape-Controlled Nanocrystals

It is still a grand challenge to use nanocrystals with controlled shapes in industrial applications due to the limitation imposed by the production scale. In essence, the vast majority of syntheses are conducted in batch reactors such as flasks or vials, and it takes about 6-7 hours to just produce a few milligrams of material per batch.[83] This amount is barely enough for initial bench testing and characterization, and simply not enough for pilot

studies, which is the very first step toward any industrial use. While the syntheses can be refined to obtain products in high quality, they may exhibit batch-to-batch irreproducibility, and attempting to scale up these syntheses raise issues such as poor uniformity and loss of both size and shape controls.[83] The formation of a nanocrystal is extremely sensitive to experimental conditions, such as the concentrations of reagents, reaction temperature, and reaction volume, among others. Therefore, when the volumes or concentrations of reagents are scaled up in a synthesis, issues such as spatial heterogeneity of temperature and chemical composition will be augmented, negatively affecting the formation of nanocrystals with well-defined size, shape, and composition.[83,84]

Alternative methods have been reported for addressing these issues. For instance, we reported an approach based on milliliter-sized droplet reactors in order to scale up the production of Pd, Au, and Pd-M nanocrystals.[83] The fluidic device shown in Figure 1.7 was assembled as a reactor where droplets of 0.25 mL in volume were produced in a continuous flow to achieve a nanocrystal production on a scale of 1−10 g per hour.[83] However, more work needs to be done towards optimizing and applying the successful operation of these devices in industrial sector. Such techniques still use excess of reagents needed for the formation of the nanocrystals, and generates large amounts of waste.

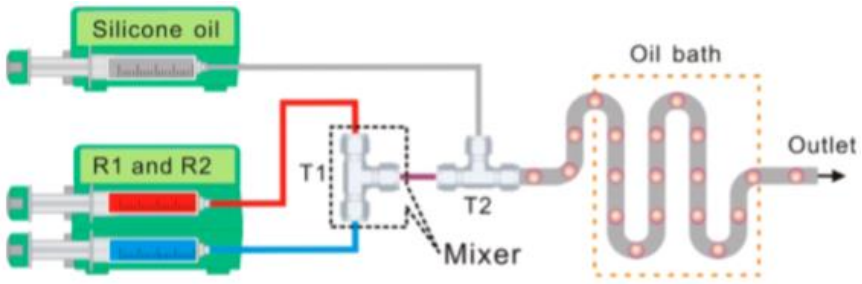

Figure 1.7. Schematic illustration of the device used for generating milliliter-sized droplets. The device is assembled from commercially available syringe pumps, T connectors, and PTFE tubes with different inner diameters. (Reprinted with permission from [83]. Copyright 2014 *American Chemical Society*.)

1.4 Scope of This Work

The aim of the work presented in this dissertation is to develop robust protocols that be used to further understand the mechanisms responsible for the size, shape, and structural evolution of colloidal noble-metal nanocrystals. While significant progress has been made over the past decade, the synthesis of noble-metal nanocrystals still relies on a trial-and-error approach. A better understanding of the underlying forces guiding the formation and development of noble-metal nanocrystals will help avoid the waste of time and materials, and ultimately accelerate the adoption of these nanomaterials in widespread applications. This dissertation focusses on the development of simple, robust, and scalable methods for the synthesis of palladium-based nanocrystals as guided by kinetic considerations, and the use of such Pd nanocrystals as seeds for the synthesis of better catalysts based on platinum and iridium.

In Chapter 2, I introduce a simple and reliable method for the scalable production of Pd nanoplates containing stacking faults. The success of my protocol was reliant on the use of hydroxylamine as a reducing agent, which allowed for the nucleation and growth of well-defined Pd nanoplates with an average edge length of 24.5 ± 6.6 nm and thickness of 4.7 ± 0.4 nm. I conducted a kinetic analysis to validate the importance of an appropriate initial reduction rate in determining the formation of seeds lined with stacking faults. To demonstrate the robustness of this synthesis, I conducted a set of control experiments under different experimental conditions such as acidity, temperature, and chemical environment and demonstrated that Pd nanoplates could be obtained as the final products. I further extended the batch-based synthesis to the continuous flow setting, moving one step closer toward high-volume production. Taken together, this method offered both simplicity and

reproducibility for the synthesis of Pd nanoplates, which will enable future mechanistic studies and applications.

In Chapter 3, I introduce the use of a dual-reductant approach to the shape-controlled synthesis of colloidal metal nanocrystals. Traditional methods involve the reduction of a metal precursor by a single reductant, followed by homogeneous nucleation to generate nuclei and then seeds, that subsequently grow into nanocrystals. In general, it is a grand challenge to optimize such an approach because the kinetic requirement for nucleation tends to be drastically different from what is needed for guiding the growth process. In this work, I introduce a new strategy of synthesis based on the simultaneous use of strong and weak reductants in the same reaction solution. By controlling their amounts to program the reduction kinetics, the strong reductant only regulates the homogeneous nucleation process to generate the desired seeds, and once consumed, the weak reductant will take over to control the growth pattern and thereby the shape of the resulting nanocrystals.

In Chapter 4, I provide a new perspective on increasing the volume of production during a synthesis of colloidal nanocrystals *via* seed-mediated growth. I demonstrate that the yield of Pd octahedra and Pd@$Pt_{3–4L}$ (L: atomic layers) core–shell octahedra with different sizes can be increased from *ca.* 2 mg to over 500 mg without compromising the product quality. Specifically, I applied geometric and stoichiometric analyses to calculate the minimum amounts of reagents needed for the complete evolution of Pd cubic seeds into Pd octahedra, and subsequently for the formation of Pd@$Pt_{3–4L}$ core–shell octahedra through conformal Pt coating. The simple analyses of geometry and stoichiometry allowed

me to obtain uniform products by avoiding homogeneous nucleation while minimizing the waste of reagents.

In Chapter 5, in collaboration with Dr. Xiaohu Xia, we reported, for the first time, a simple method based on seed-mediated growth for the facile synthesis of Ir nanocrystals with well-controlled facets. The essence of this approach was to coat an ultrathin conformal shell of Ir on a Pd seed with a well-defined shape at a relatively high temperature to ensure the fast surface diffusion of Ir atoms. In this way, the facets on the initial Pd seed were faithfully replicated in the resultant Pd@Ir core–shell nanocrystal. With 6 nm Pd cubes and octahedra encased by {100} and {111} facets, respectively, as the seeds, we successfully generated Pd@Ir cubes and octahedra covered by Ir{100} and Ir{111} facets. The Pd@Ir cubes showed higher H_2 selectivity (31.8% vs 8.9%) toward the decomposition of hydrazine compared with Pd@Ir octahedra with roughly the same size.

1.5 References

[1] https://en.wikipedia.org/wiki/Precious_metal

[2] S. Kallmann, *Anal. Chemi.* **1984**, 56, 1020.

[3] http://www.platinum.matthey.com/prices/price-charts

[4] https://www.moneymetals.com/precious-metals-charts/gold-price

[5] M. A. Boles, D. Ling, T. Hyeon, D. V. Talapin, *Nature Mater.* **2016**, *15*, 141.

[6] Y. Xia, Y. Xiong, B. Lim, S. E. Skrabalak, *Angew. Chem. Int. Ed.* **2009**, *48*, 60.

[7] F. Baletto, R. Ferrando, *Rev. Mod. Phys.* **2005**, 77, 3771.

[8] G. A. Ozin, A. C. Arsenault, L. Cademartiri, *Nanochemistry A Chemical Approach to Nanomaterials, 2nd Ed.* RCS, Royal Society of Chemistry, Cambridge, UK, **2006**, p.11–14.

[9] W. P. Halperin, *Rev. Mod. Phys.* **1986**, *58*, 533.

[10] E. C. Dreaden, A. M. Alkilany, X. Huang, C. J. Murphy, M. A. El-Sayed, *Chem. Soc. Rev.* **2012**, 41, 2740.

[11] E. Hutter, J. H. Fendler, *Adv. Mater*. **2004**, *16*, 1685.

[12] S. E. Skrabalak, L. Au, X. Li and Y. Xia, *Nat. Protoc.* **2007**, 2, 2182.

[13] J. Kašpar, P. Fornasiero, N. Hickey, *Catal. Today* **2003**, 77, 419.

[14] M. Zhang, M. Jin, Y. Xia, *Chem. Soc. Rev.* **2012**, *41*, 8035.

[15] M. Crespo-Quesada, A. Yarulin, M. Jin, Y. Xia, L. Kiwi-Minsker, *J. Am. Chem. Soc.* **2011**, *133*, 12787.

[16] M. T. Reetz, E. Westermann, *Angew. Chem. Int. Ed.* **2000**, *112*, 170.

[17] J. Zhang, Q. Jiang, D. Yang, X. Zhao, Y. Dong, R. Liu, *Chem. Sci.* **2015**, *6*, 4674.

[18] L. Yin, J. Liebscher, *Chem. Rev*. **2007**, *107*, 133.

[19] Gasteiger, H. A.; Kocha, S. S.; Sompalli, B.; Wagner, F. T. *Appl. Catal., B* **2005**, *56*, 9.

[20] Shao, M. *Electrocatalysis in Fuel Cells: A Non- and Low-Platinum Approach*; Springer: London, 2013.

[21] N. Tian, Z.-Y. Zhou, S.-G. Sun, Y. Ding, Z. L. Wang, Science **2007**, *316*, 732.

[22] H. Connor, *Platinum Metals Rev.* **1967**, *11*, 60.

[23] G. Ertl, *Handbook of Heterogeneous Catalysis*, Wiley-VCH, Weinheim, 2008.

[24] I. Katsounaros, W. B. Schneider, J. C. Meier, U. Benedikt, P. U. Biedermann, A. A. Auer, K. J. J. Mayrhofer, *Phys. Chem. Chem. Phys.* **2012**, *14*, 7384.

[25] L. N. Lweis, J. Stein, Y. Gao, R. E. Colborn, G. Hutchins, *Platinum Metals Rev.* **1997**, *41*, 66.

[26] L. M. Falicov, G. A. Somorjai, *Proc. Natl. Acad. Sci. USA* **1985**, *82*, 2207.

[27] A. -C. Shi, R. I. Masel, *J. Catal.* **1989**, *120*, 421.

[28] C. A. Stowell, B. A. Korgel, *Nano Lett.* **2005**, *5*, 1203.

[29] Y. Lin, R. G. Finke, *Inorg. Chem.* **1994**, *33*, 4891.

[30] C. K. Yee, R. Jordan, A. Ulman, H. White, A. King, M. Rafailovich, J. Sokolov, *Langmuir* **1999**, *15*, 3486.

[31] V. Mevellec, A. Roucoux, E. Ramirez, K. Phillippot, B. Chaudret, *Adv. Synth. Catal.* **2004**, *346*, 72.

[32] G. S. Fonseca, J. D. Scholten, J. Dupont, *Synlett.* **2004**, *9*, 1525.

[33] S. Kainz, A. Brinkman, W. Leitner, A. Pfaltz, *J. Am. Chem. Soc.* **1999**, *121*, 6429.

[34] A. F. Westerhaus, B. Wendt, A. Dumrath, G. Wienhofer, K. Junge, M. Beller, *ChemSusChem* **2013**, *6*, 1001.

[35] K. Liu, A. Wang, T. Zhang, *ACS Catal.* **2012**, *2*, 1165.

[36] S. H. Joo, J. Y. Park, J. R. Renzas, D. R. Butcher, W. Huang, G. A. Somorjai, *Nano Lett.* **2010**, *10*, 2709.

[37] K. Honkala, A. Hellman, I. N. Remediakis, A. Logadottir, A. Carlsson, S. Dahl, C. H. Christensen, J. K. Norskov, *Science* **2005**, *307*, 555.

[38] H. Y. Kim, H. M. Lee, J. N. Park, *J. Phys. Chem. C* **2010**, *114*, 7128.

[39] R. Heck, R. Farrauto, *Catalytic Air Pollution Control: Commercial Technology*. Van Nostrand Reinhold: New York, 1995.

[40] Y. Yuan, N. Yan, P. J. Dyson, *ACS Catal.* **2012**, *2*, 1057.

[41] W. P. Halperin, *Rev. Mod. Phys.* **1986**, *58*, 533.

[42] E. Hutter, J. H. Fendler, *Adv. Mater*. **2004**, *16*, 1685.

[43] N. L. Okamoto, S. Fujimoto, Y. Kambara, M. Kawamura, Z. M. T. Chen, H. Matsunoshita, K. Tanaka, H. Inui, E. P. George, *Sci. Rep.* **2016**, *6*, 1.

[44] Y. -W. Jun, Y. -M. Huh, J.-S. Choi, J.-H. Lee, H.-T. Song, S. Kim, S. Yoon, K. -S. Kim, J.-S. Shin, J.-S. Suh, J. Cheon, *J. Am. Chem. Soc.* **2005**, *127*, 5732.

[45] R. Narayanan, M. A. El-Sayed, *Nano Lett.* **2004**, *4*, 1343.

[46] Z.-N. Xu, J. Sun, C.-S. Lin, X.-M. Jiang, S.-Y. Peng, M.-S. Wang, G.-C. Guo, *ACS Catal.* **2013**, *3*, 118.

[47] S.-I. Choi, J. A. Herron, J. Scaranto, H. Huang, Y. Wang, X. Xia, T. Lv, J. Park, H.-C. Peng, M. Mavrikakis, Y. Xia, *ChemCatChem* **2015**, *7*, 2077.

[48] Y. Xiong, Y. Xia, *Adv. Mater.* **2007**, *19*,3385.

[49] V. K. LaMer, R. H. Dinegar, *J. Am. Chem. Soc.* **1950**, *72*, 4847.

[50] Y. Xia, K. D. Gilroy, H.-C. Peng, X. Xia, *Angew. Chem. Int. Ed.* **2017**, *56*, 60.

[51] Y. Wang, H.-C. Peng, J. Liu, C. Z. Huang, Y. Xia, *Nano Lett.* **2015**, *15*, 1445.

[52] J. W. Gibbs, *Trans.Connect.Acad. Sci.* **1876**, *3*, 108.

[53] K. D. Gilroy, J. Puibasset, M. Vara, Y. Xia, *Ange. Chem. Int. Ed.* **2017**, *56*, 8647.

[54] T.-H. Yang, H.-C. Peng, S. Zhou, C.-T. Lee, S. Bao, Y.-H. Lee, J.-M. Wu, Y. Xia, *Nano Lett.* **2017**, *17*, 334.

[55] T.-H. Yang, K. D. Gilroy, Y. Xia. *Chem. Sci.* **2017**, *8*, 6730.

[56] B. Wiley, Y. Sun, B. Mayers, Y. Xia, *Chem. Eur. J.* **2005**, *11*, 454.

[57] M. Jin, H. Liu, H. Zhangm Z. Xie, J. Liu, Y. Xia, *Nano Res.* **2011**, *4*, 83.

[58] B. Lim, Y. Xiong, Y. Xia, *Angew. Chem. Int. Ed.* **2007**, *46*, 9279.

[59] C. J. le Roux, R. J. Kriek, *Hydrometallurgy* **2017**, *169*, 447.

[60] F. Ketterman, M. Wuithschick, G. Caputo, R. Kraehnert, N. Pinna, K. Rademann, J. Polte, *CrystEngComm* **2015**, *17*, 1865.

[61] L. I. Elding. *Inorganica Chim. Acta*, **1972**, *6*, 647.

[61] M. Vara, P. Lu, X. Yang, C.-T. Lee, Y. Xia, *Chem. Mater.* **2017**, *29*, 4563.

[62] R. A. Marcus, *J. Chem. Phys.* **2004**, *24*, 966.

[63] R. A. Marcus, *J. Chem. Phys.* **1957**, *26*, 867.

[64] R. A. Marcus, *J. Chem. Phys.* **2004**, *26*, 872.

[65] E. E. Finney, R. G. Finke, *J.* **2007**, *317*, 351.

[66] M. A. Watzky, R. G. Finke, *Chem. Mater.* **1997**, *9*, 3083.

[67] T.-H. Yang, S. Zhou, K. D. Gilroy, L. Figueroa-Cosme, Y.-H. Lee, J.-M. Wu, Y. Xia. *Proc. Natl. Acad. Sci. USA* **2017**, *114*, 13619.

[68] Y. Xia, X. Xia, H.-C. Peng, *J. Am. Chem. Soc.* **2015**, *137*, 7947.

[69] https://www.nde-ed.org/EducationResources/CommunityCollege/Materials/Structure/planar_defects.htm

[70] S. S. Shankar, A.Rai, B. Ankamwar, A.Singh, A. Ahmad, M. Sastry, *Nat. Mater.* *2004*, *3*, 482

[71] S.P.Chandran, M. Chaudhary, R.Pasricha, A.Ahmad, M. Sastry, *Biotechnol. Prog.* **2006**, *22*, 577.

[72] Y. Xiong, J. M. McLellan, J. Chen, Y. Yin, Z.-Y. Li and Y. Xia, *J. Am. Chem. Soc.*, **2005**, *127*, 17118.

[73] Y. Xiong, I. Washio, J. Chen, H. Cai, Z.-Y. Li and Y. Xia, *Langmuir*, **2006**, *22*, 8563.

[74] I. Washio, Y. Xiong, Y. Yin, Y. Xia, *Adv. Mater.* **2006**, *18*,1745.

[75] M. Jin, H. Zhang, Z. Xie, Y. Xia, *Energy Environ. Sci.* **2012**, 5, 6352.

[76] H. Zhang, M. Jin, Y. Xiong, B. Lim, Y. Xia, *Acc. Chem. Res.* **2012**, 46, 1783.

[77] S. Bao, X. Yang, M. Luo, S. Zhou, X. Wang, Z. Xie, Y. Xia, *Chem. Comm.* **2016**, *52*, 12594.

[78] S. Xie, S.-I. Choi, N. Lu, L. T. Roling, J. A. Herron, L. Zhang, J. Park, J. Wang, M. J. Kim, M. Mavrikakis, Y. Xia, *Nano Lett.* **2014**, *14*, 3570.

[79] J. Park, L. Zhang, SI. Choi, L. Roling, N. Lu, J. Herron, S. Xie, J. Wang, M. Kim, M. Mavrikakis, Y. Xia, *ACS Nano*.

[80] X. Wang, M. Vara, M. Luo, H. Huang, A. Ruditskiy, J. Park, S. Bao, J. Liu, J. Howe, M. Chi, Z. Xie, Y. Xia, *J. Am. Chem. Soc.* **2015**, *137*, 15036.

[81] X. Wang, S.-I. Choi, L. T. Roling, M. Luo, C. Ma, L. Zhang, M. Chi, J. Liu, Z. Xie, J. A. Herron, M. Mavrikakis, Y. Xia, *Nature Comm.* **2015**, *6*, 7594.

[82] X. Xia, S. Xie, M. Liu, H.-C. Peng, N. Lu, J. Wang, M. J. Kim, Y. Xia, *Proc. Natl. Acad. Sci. USA* **2013**, *110*, 6669.

[83] L. Zhang, G. Nui, N. Lu, J. Wang, L. Tong, L. Wang, M. Kim, Y. Xia, *Nano Lett.* **2014**, 14, 6626.

[84] L. Zhang, Y. Xia, *Adv. Mater.* **2014**, *26*, 2600.

CHAPTER 2

FACILE, ROBUST, SCALABLE SYNTHESIS OF PALLADIUM NANOPLATES WITH HYDROXYLAMINE AS REDUCTANT AND THE MECHANISTIC INSIGHTS FROM KINETIC ANALYSIS

2.1 Introduction

Noble-metal nanocrystals are finding use in a myriad of applications ranging from optical sensing to plasmonic waveguiding, biomedical research, photovoltaics, and heterogeneous catalysis.[1-5] Similar to other metals, the physicochemical properties of a Pd nanocrystal are strongly correlated with its size, shape, and internal defect structure.[6] For example, in the context of heterogeneous catalysis, the surface-to-volume ratio increases rapidly, as does the utilization efficiency of surface atoms, when the size of Pd nanocrystals is reduced.[6] As for plasmonics, Pd nanocrystals with a spherical shape only exhibit localized surface plasmon resonance (LSPR) in the UV region.[7] To make Pd nanocrystals useful for photocatalytic applications that rely on sunlight for excitation, the morphology can be modified to generate highly anisotropic nanorods or nanoplates and thereby obtain LSPR peaks in the visible and near infrared (NIR) regions. To this end, it was shown that Pd nanoplates exhibit LSPR peaks in the visible while Zheng *et al.* reported the synthesis of Pd hexagonal nanosheets displaying strong LSPR in the NIR region.[7-9] As evident from these and other examples, the availability of synthetic methods capable of engineering the shape of Pd nanocrystals will be beneficial to the expansion of their properties and thus enhancement of their performance toward various applications.

During the last few decades, several groups have worked diligently to elucidate the underlying mechanisms that control the shape evolution of noble-metal nanocrystals.[10-

13] When synthesized in a wet-chemical setting through homogeneous nucleation, it is generally accepted that the final shapes taken by the nanocrystals have strong correlations with the seeds formed in the very early stage, in which metal atoms agglomerate together to form fluctuating nuclei and then well-defined structures known as seeds.[14] The seeds typically exhibit one or more of the following types of internal structures, including single-crystal, singly twinned, multiply twinned, and stacking-fault-lined.[10] Recent studies have shown that both kinetics of the reaction (*e.g.*, initial reduction rate of the metal precursor)[11,12] and structural thermodynamics (*e.g.*, relative stability of the surface and volume between the various nanostructures)[15,16] play important roles in determining the types of seeds formed during the initial stage of a synthesis. For example, one can control the production of Pd nanocrystals with shapes ranging from cuboctahedron (single-crystal) to icosahedron (multiply twinned) and nanoplate (stacking-fault-lined) by tuning the initial reduction rate of a Pd(II) precursor from relatively fast to moderate and slow, respectively.[11,12] This example illustrates how sensitive the nucleation process is to the reduction kinetics and also points to the origin of irreproducibility that troubles many nanocrystal syntheses.

Among the nanocrystals with various shapes, nanoplates are favorable in a slow reduction process and have only been obtained under kinetic control. Such highly anisotropic nanostructures are intrinsically higher in energy than other thermodynamically favored shapes such as polyhedra. Factors such as the rate of precursor reduction, atom deposition, and surface diffusion can all force the nanocrystal to evolve into a non-equilibrium shape such as the nanoplate.[10,14] Accordingly, several groups have synthesized Pd nanoplates using methods based on both polyol and aqueous systems. For

example, Xia group synthesized Pd triangular nanoplates by controlling the reduction rate using tetraethylene glycol (TTEG) as a relatively weak reducing agent.[12] Additionally, there are reports of aqueous methods that involve the use of surfactants and reducing agents such as PVP,[7] relatively long reaction times,[7,8] and/or hazardous gases such as carbon monoxide.[9,17] All these methods have a limited window of reduction kinetics and require a fine control over experimental parameters to obtain the nanoplates. For example, if the reaction rate was slightly faster, or the concentration of reagent was not optimal, the purity and quality of the Pd nanoplates would be negatively impacted. In addition, the nature of these methods (presence of gases, polyol, long reaction times) imposes a limitation on their potential scalability and reproducibility.

In this work, I report a simple and robust method for the synthesis of Pd nanoplates using hydroxylamine as the reducing agent. Hydroxylamine is an oxygenated derivative of ammonia widely used as a reducing agent in organic syntheses but relatively unexploited in the synthesis of colloidal metal nanocrystals. Due to its good chemical stability, easy preparation, and mild reducing power, here I extend the use of hydroxylamine to the synthesis of Pd nanoplates, and also examine the effects of experimental parameters on the final product. A kinetic analysis is also conducted to shed light on the mechanistic understanding.

2.2 Results and Discussion

For the synthesis of Pd nanoplates, I used Na_2PdCl_4 as a salt precursor, hydroxylamine as the primary reducing agent, PVP as a surfactant, and CA as a capping agent toward Pd(111) surface. In a standard protocol, an aqueous solution containing PVP,

hydroxylamine, and CA was prepared at room temperature. Subsequently, an aqueous solution of Na_2PdCl_4 was added in one-shot under magnetic stirring, followed by heating at 100 ºC in an oil bath.

Figure 2.1A shows the TEM image of a typical sample of Pd nanoplates, which had an average edge length of 24.5 ± 6.6 nm and thickness of 4.7 ± 0.4 nm. In this sample, I have both hexagonal (~70%) and triangular (~30 %) nanoplates. I used HRTEM to analyze the atomic structure of the Pd nanoplates. The individual hexagonal plate shown in Figure 2.1B was oriented along its [111]-zone axis, as evident by the hexagonal geometry and packing of atoms as highlighted in the inset. To determine the thickness and further analyze the crystal structure of the Pd nanoplates, I drop-casted their suspension on a copper TEM grid coated with lacey carbon. I was able to locate individual nanoplates oriented with the edges and {111} facets perpendicular and parallel to the electron beam, respectively. This allowed us to perform HRTEM imaging of atomic columns along the lateral direction of an individual nanoplate (see Figure 2.1C and the red-dashed line that partially highlights the stacking fault line). An enlarged view of the HRTEM can be found in Figure 2.2 of the supporting information. From the HRTEM image, we were able to obtain a *d*-spacing of around 2.25 Å for the (111) planes, a value consistent with the JCPDS datum of 2.24 Å. We also performed an XRD analysis of the Pd nanoplates. Most notably, the (111) peak at $2\theta = 40.2°$ is predominantly stronger than the (200) peak at $2\theta = 46.7°$ and the (220) peak at $2\theta = 68.3°$ (even considering the structure factors), suggesting that most of the nanoplates were oriented such that their large flat {111} faces were parallel to the surface of the sample stage. This result also suggests that our sample was high in purity. From the

XRD pattern we obtained a value of 2.24 Å for d_{111}, which is consistent with the aforementioned JCPDS value.

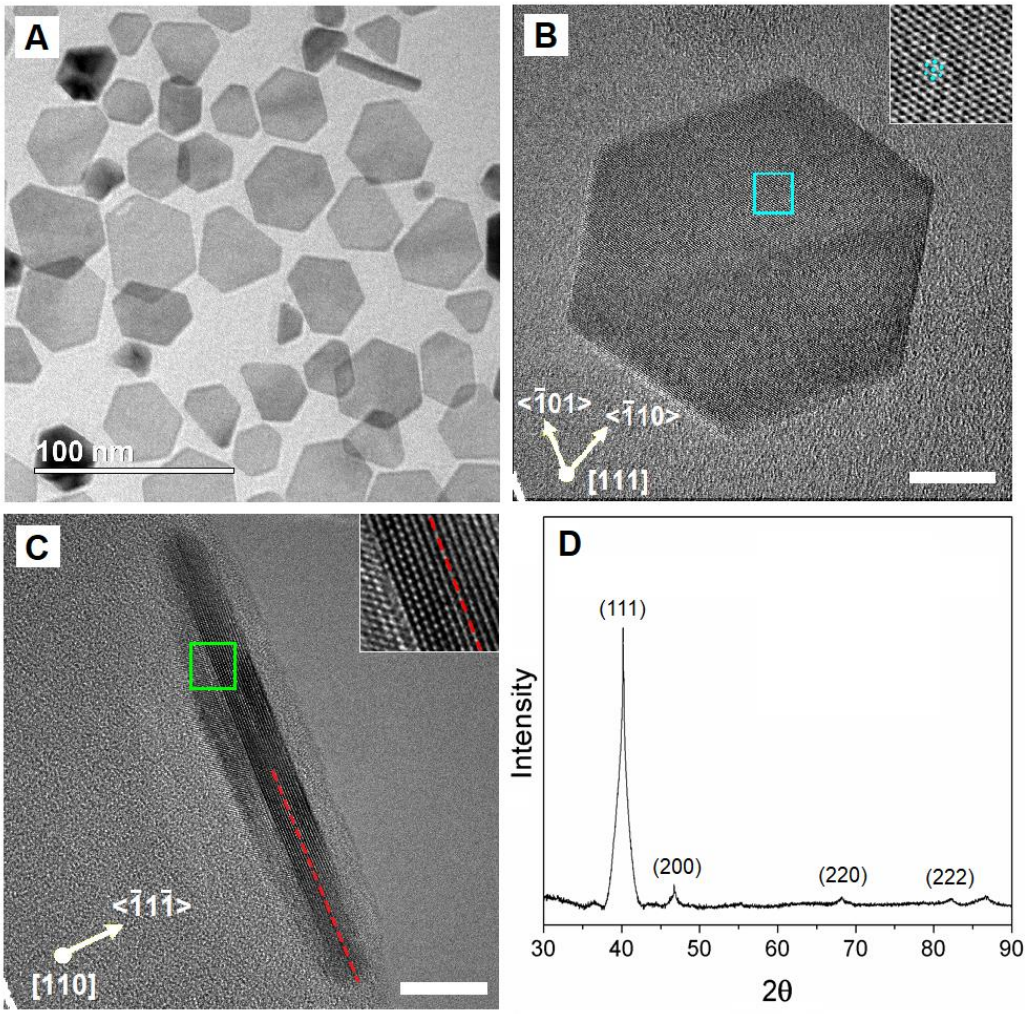

Figure 2.1. (A) TEM image of a typical sample of Pd nanoplates prepared using the standard protocol. (B, C) HRTEM images of an individual nanoplate imaged from (B) the top surface with an orientation along its [111]-zone axis (inset: a magnified view of the boxed region) and (C) the side surface with an orientation along its [110]-zone axis (inset: a magnified view of the atoms in the green box). The red-dashed lines partially mark the stacking-fault plane. (D) X-ray diffraction pattern of the Pd nanoplates, indicating that the nanoplates were crystallized in the *fcc* structure and they tended to lie flat, with (111) planes parallel to the substrate surface, during drop-casting. Scale bars: 10 nm.

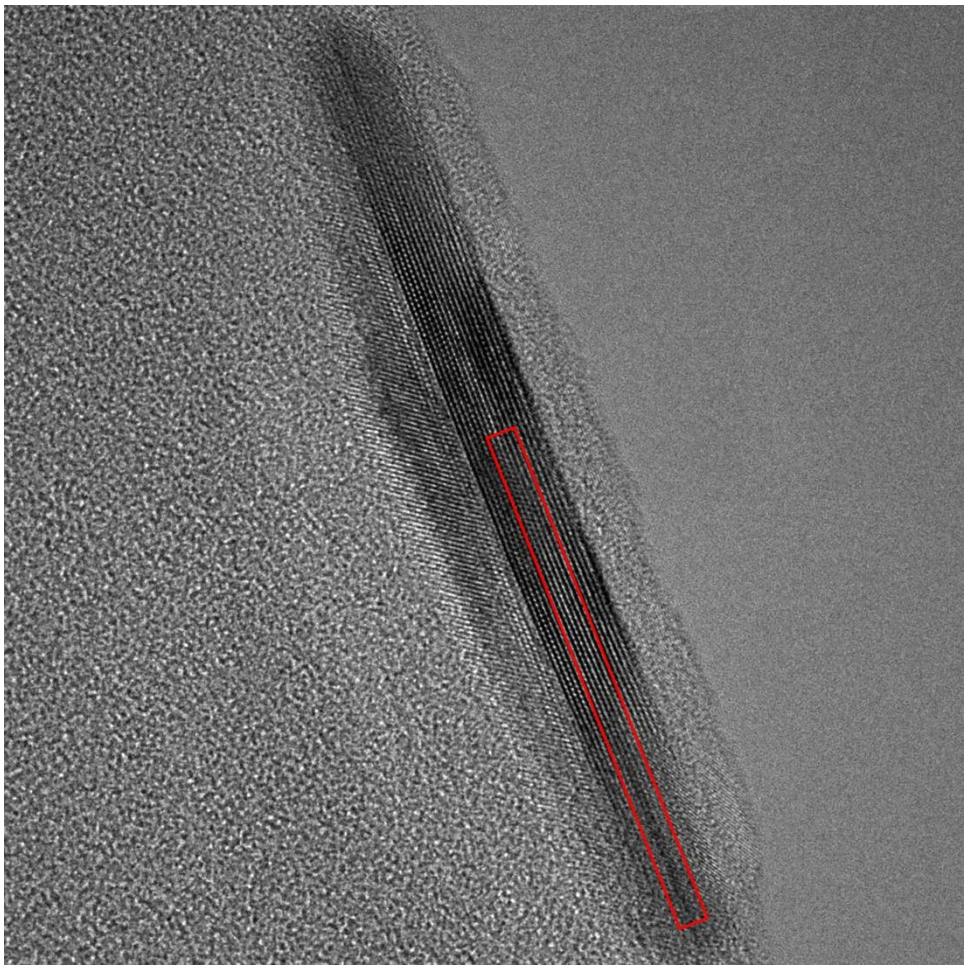

Figure 2.2. A blow-up view of Figure 1c to clearly reveal the stacking fault.

The exact mechanism of nanoplate formation is still unknown and the underlying question is in the nucleation process involved in the formation of the seed. It has been suggested that the key factor for the formation of nanoplates is a relatively slow reduction rate for the generation of stacking faults during seed formation.[18] To test this hypothesis, I monitored the progress of the reaction using UV-vis spectroscopy and then compared the spectra to the product formed at different points during the synthesis. I set up a number of parallel reactions in the same oil bath and simultaneously started the timer (Note: all vials were firmly capped). One reaction vial was taken out from the oil bath at a specific time

point and immediately placed in an ice bath to quench the reduction. After removing the solid products by centrifugation, I analyzed the concentration of Pd(II) in the supernatant using UV-vis spectroscopy. As shown in Figure 2.3A, the intensity of the absorption peak associated with Pd(II) decreased with time, which can be attributed to the reduction by hydroxylamine for the generation of Pd nanoplates. By fitting the linear plot in Figure 2.3B, and using a conversion factor from minute to second, I obtained a rate constant of $k = 3.0 \times 10^{-4}\ s^{-1}$ for the reduction reaction. When combined with the initial concentration of $PdCl_4^{2-}$ in the reaction solution (1.2 mM by taking into account the dilution factor), I obtained an initial reduction rate of $R_0 = 3.6 \times 10^{-7} M \cdot s^{-1}$. This value falls into the range responsible for the formation of stacking faults, in agreement with our previous report.[12]

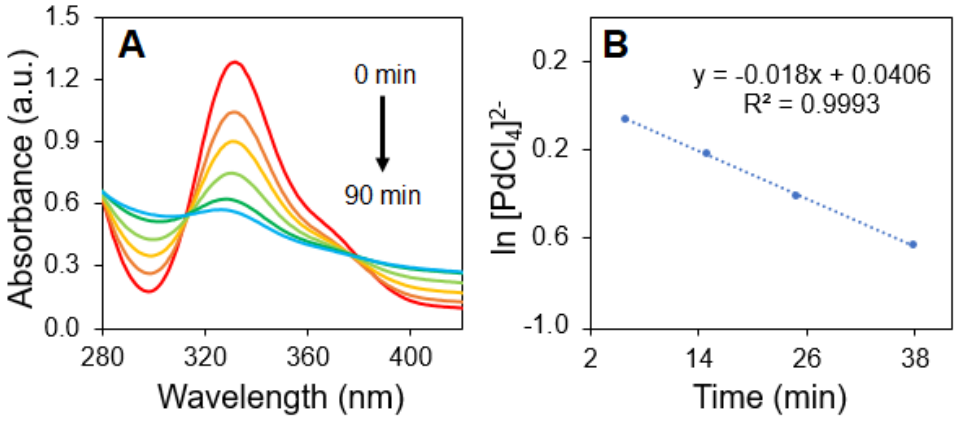

Figure 2.3. (A) UV-vis spectra showing the change in absorbance for the Pd(II) ions over a course of 60 min. (B) Log-plot trending the concentration of the remaining Pd(II) precursor as the reaction proceeds.

To analyze the evolution of the nanoplates, I imaged the nanocrystals formed at 15, 30, 60, and 180 min of a synthesis using TEM. The formation of plate-like structures was evident even at the very beginning of a synthesis (Figure 2.4A), and their average edge length then increased from 4 to 10, 14, and 25 nm (Figure 2.4, B-D). Also, the size

distribution narrowed with reaction time, suggesting that Ostwald ripening played a role in the formation of the relatively large nanoplates. It is worth mentioning that the growth of nanoplates appeared to be preferentially along the lateral directions since the edge length increased from 4.2 nm to 25–30 nm, in contrast to the thickness that remained around 4.7 nm. This trend is also consistent with the proposed mechanism for the formation of Ag nanoplates.[18]

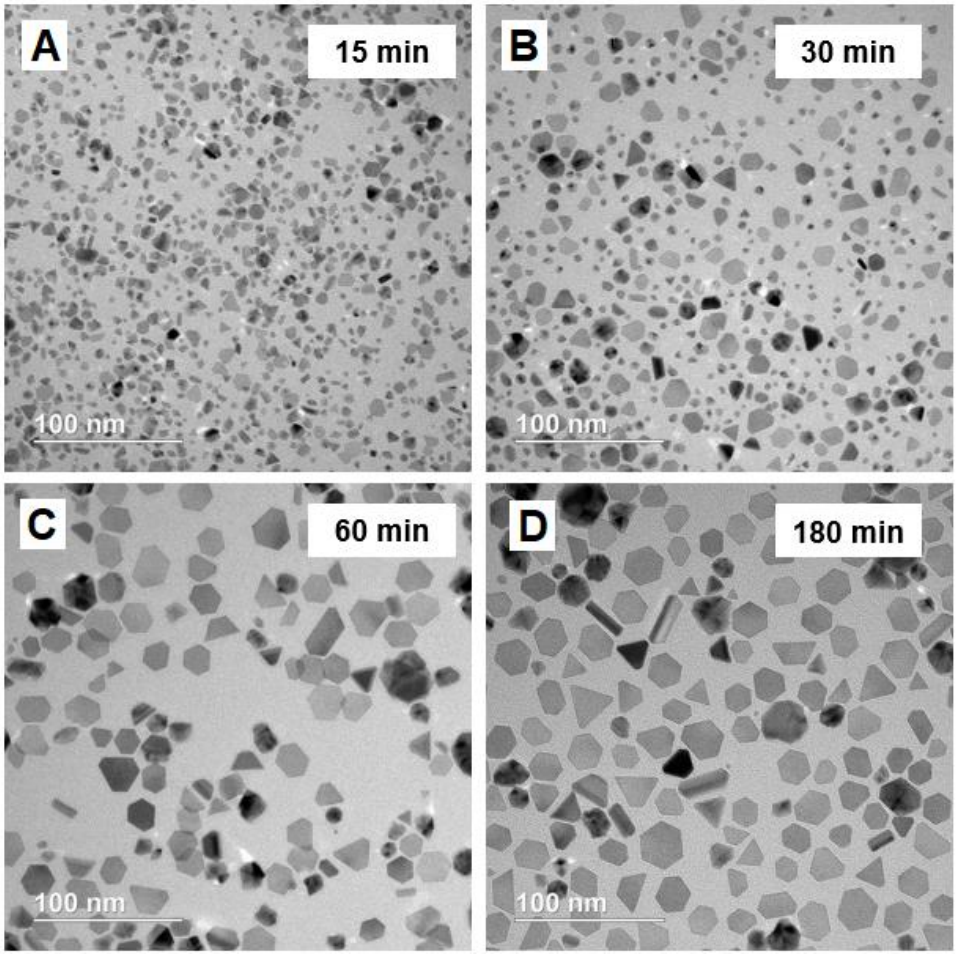

Figure 2.4. TEM images of the products of a standard synthesis when the reduction was quenched after reacting for (A) 15, (B) 30, (C) 60, and (D) 180 min.

Interestingly, when the reaction was performed in a single vial and aliquots were taken at different time points (note: the vial was constantly uncapped in this case), the

reaction kinetics was different and thus the products were also different. As shown in Figure 2.5A and B, the kinetics show a two-step reduction process where the initial reduction occurred very slowly and then suddenly accelerated after 60 min, which could be attributed to the accelerated reduction of metal precursor by auto-catalytic reduction.[12,19] As shown in Figure 2.5C-F, the Pd nanoplates exhibited a rounded profile, which promotes us to ask whether oxidative etching was occurring during the kinetic studies because of the constant exposure to air when extracting aliquots.

I performed additional syntheses to explore the role of the dissolved gases on the final products. Four reaction vials were prepared including: *i*) an uncapped vial and thus constantly exposed to air, *ii*) a capped vial and thus not exposed to air, *iii*) a capped vial purged with pure nitrogen, and *iv*) a capped vial purged with pure oxygen. Note that the syntheses involving nitrogen and oxygen, experiments (iii) and (iv), were purged with the respective gases for 30 min. As shown in Figure 2.6, the morphology of the products under air, oxygen, and nitrogen environment did not differ significantly, which suggests that oxidative etching can be excluded as a cause for the rounding of the nanoplates. A plausible explanation for this observation should thus be attributed to N_2O, the oxidation product of hydroxylamine. The formation of N_2O gas was observed by Bengtsson-Kloo *et al.* when studying the oxidation of hydroxylamine by iron(III).[20-22] I posit that the process of opening the vial for the kinetic measurements may have relieved some of the pressure, allowing the N_2O to escape from the reaction solution, which could have a certain role in controlling the shape of the Pd nanoplates. However, I have to point out that the extent of N_2O production and the exact role of N_2O are yet to be completely determined.

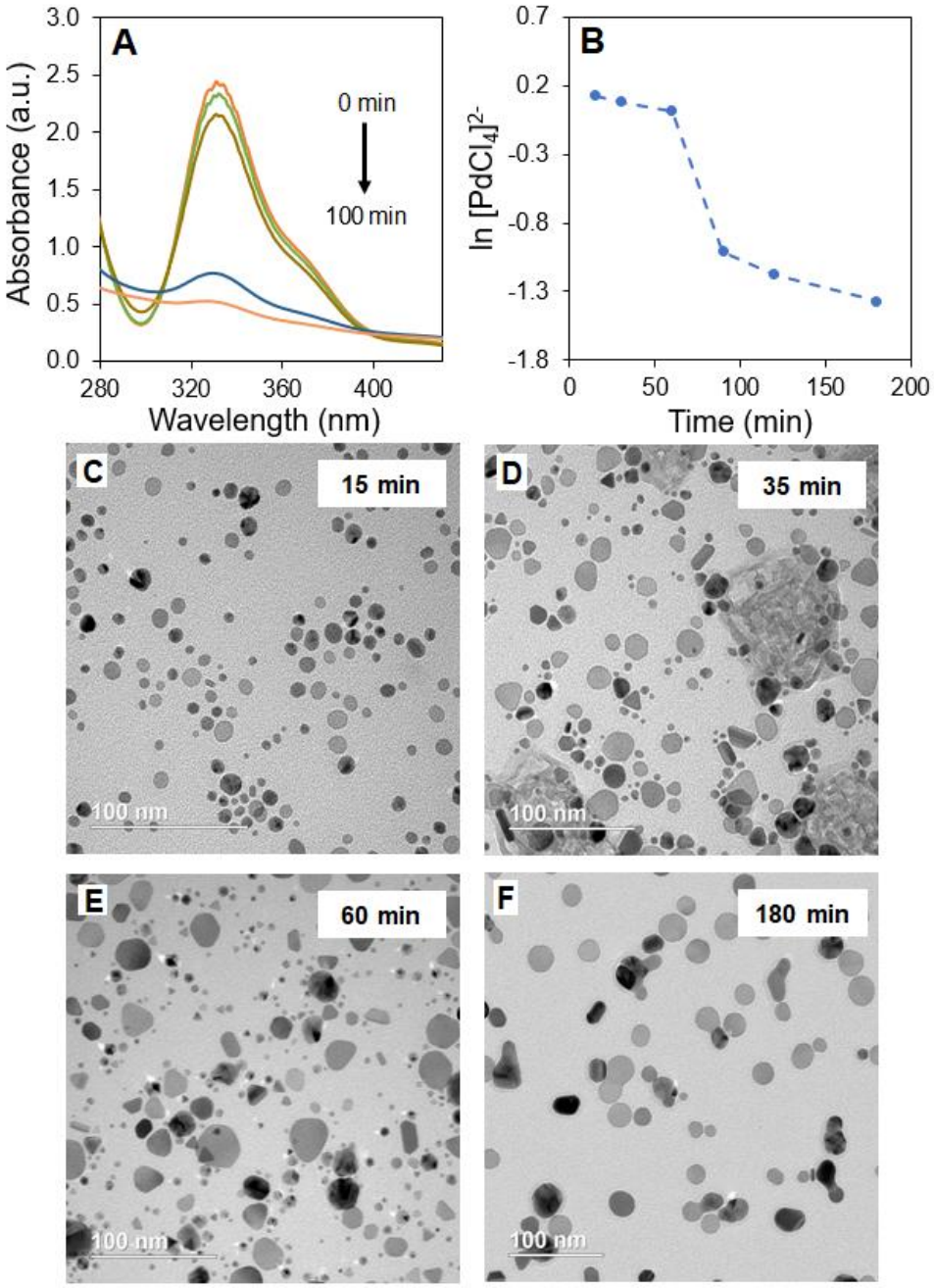

Figure 2.5. (A) UV-vis spectra tracking the change in absorbance for the Pd(II) precursor over a course of 120 min, during which the vial was uncapped to sample aliquots for UV-vis and TEM analyses. (B) Plot trending the concentration of the remaining Pd(II) precursor as a function of reaction time. (C-F) TEM images of the solid products obtained at (C) 15, (D) 35, (E) 60, and (F) 180 min, into the synthesis.

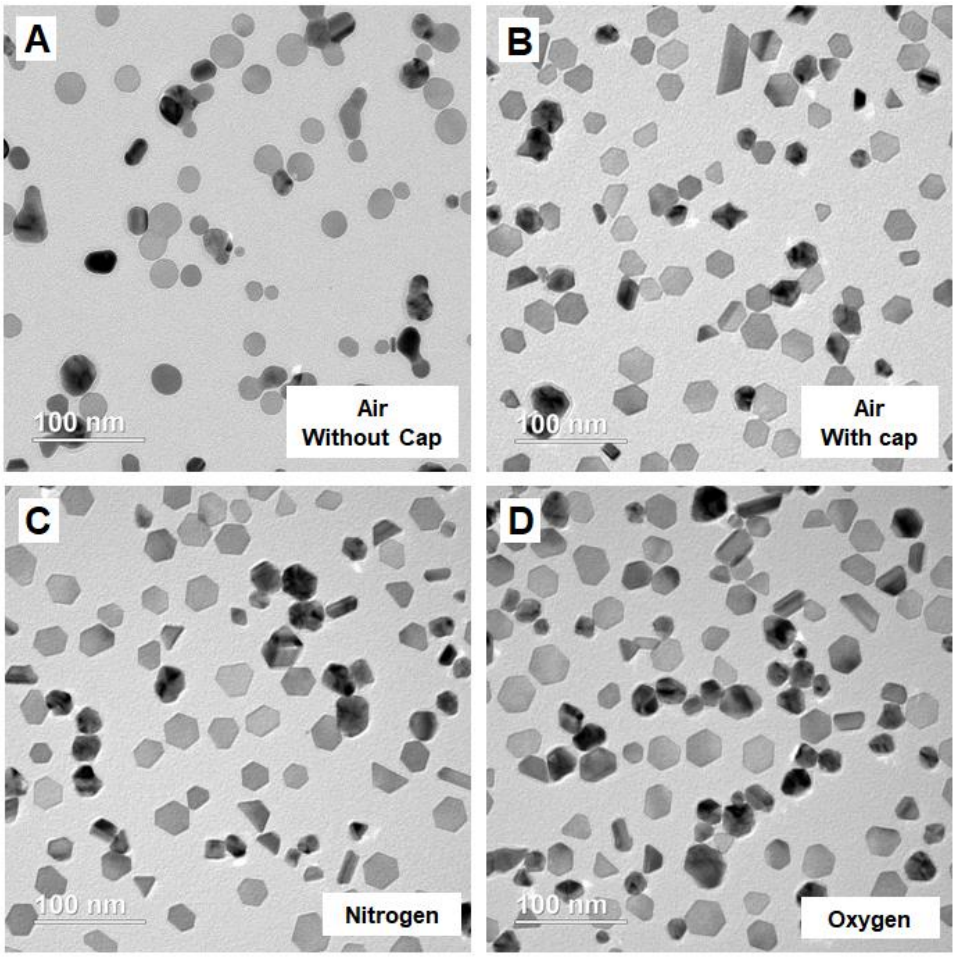

Figure 2.6. TEM images of Pd nanoplates formed under different reaction conditions by varying the gases in the reaction vials: (A) no capping, (B) tightly capped, (C) nitrogen purging and then tightly capping, and (D) oxygen purging and then tightly capped.

The reducing power of hydroxylamine strongly depends on pH,[21] and therefore, even slight changes to the pH are expected to impact the kinetics and correspondingly the shape and structure of the Pd products.[12] For this reason, I determined if the presence of CA would affect the outcome of a synthesis by performing a series of control experiments. When only using hydroxylamine in the reaction solution (*i.e.*, in the absence of CA), the solution pH was 3.8 rather than 2.7, and I observed two populations of particles: Pd nanoplates with an average edge length of 15 ± 4 nm and relatively large (around 75 nm)

particles with unidentifiable internal defect structures, see Figure 2.7A. These results suggest that the change to pH could play a critical role in controlling the final product. It should be noted that CA could also serve as a capping agent since computational calculations have suggested that CA had a strong propensity to bind to Pd(111).[23] To corroborate if the acidic environment was, in fact, assisting the formation of plates, I changed CA to ascorbic acid, a compound commonly used solely as a reducing agent. As shown in Figure 2.7B, I obtained Pd nanoplates with an average edge length of 18 ± 1 nm. These results suggest that the acidic environment could slow down the reaction kinetics to favorably support the formation of nanoplates. Also, the slightly bigger size of the nanoplates also suggest a slower reduction, because less seeds would be formed at the beginning of reaction and thus bigger particles. However, similar to CA, ascorbic acid might be interacting with the surface of the Pd nanocrystals too,[23] and it could also be serving as a reducing agent, making it very difficult to isolate the precise roles of the individual additives.

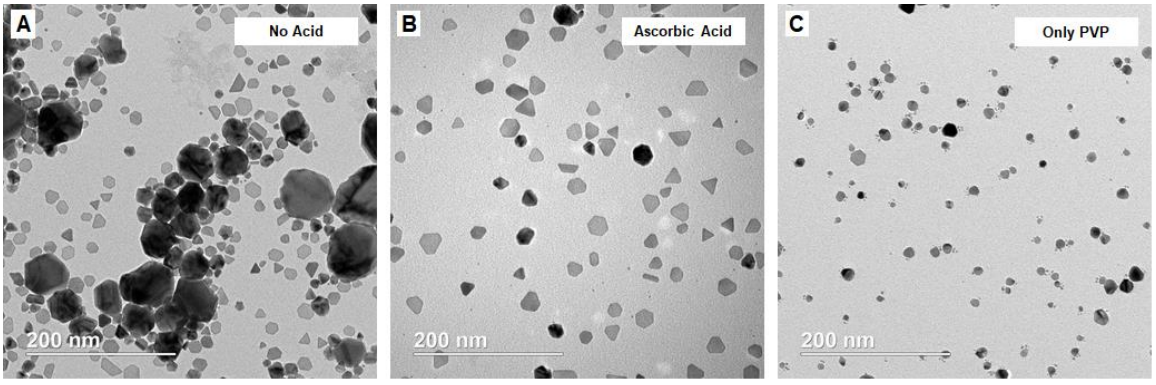

Figure 2.7 Control experiments where (A) CA was not added to reaction, (B) ascorbic acid was used instead of CA, and (D) only PVP was used in the absence of hydroxylamine.

Despite the evident impact of hydroxylamine and the different acids had on the formation of Pd nanoplates, I are still uncertain about the exact reduction mechanism. The

PVP introduced as a colloidal stabilizer could also act as a reducing agent itself.[24] Therefore, I conducted the reaction in the absence of hydroxylamine. As shown in Figure 2.7C, a mix of different Pd nanocrystals were formed with sizes around 14 ± 2 nm, but with clearly no control over the shape and internal twin structure. This result indicates that PVP does have reducing power, but it cannot be used solely as a reducing agent for the formation of Pd nanoplates in the experiments. As shown in the UV-vis spectra of Figure 2.8, the introduction of PVP or CA did not cause significant changes to the absorption peak position of the Pd(II) complex, suggesting their negligible role in coordinating to Pd(II) ions relative to other ligands such as chloride and water. Taken together, I believe that PVP mainly served as a co-reductant and a colloidal stabilizer during the formation of the Pd nanoplates.

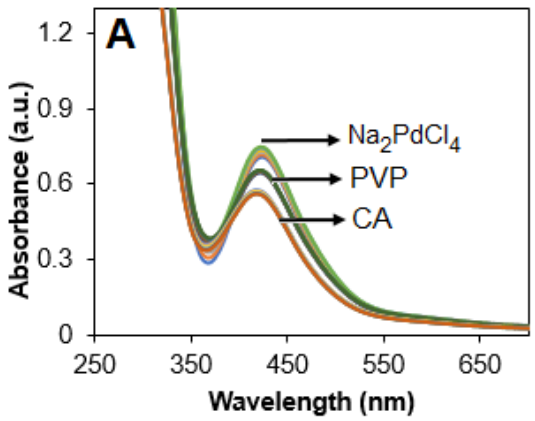

Figure 2.8. Control experiment where aliquots of aqueous PVP and CA were sequentially added into an aqueous solution of Na_2PdCl_4. The spectra were recorded up to 20 min after the introduction of each solution. The drop in peak intensity could be attributed to the dilution effect.

The method I developed for the synthesis of Pd nanoplates does not require organic solvents. It is also simple and robust, making it ideal to explore its scalability for high-volume production. To date, there are no reports on the synthesis of Pd nanoplates using a continuous flow system. Here I successfully extended the synthesis to a continuous flow

reactor and obtained Pd nanoplates with quality compatible to those obtained in a batch reactor. Both the syntheses in batch and continuous flow reactors were conducted at a lower temperature of 80 °C than the standard protocol. As shown in Figure 2.9, Pd nanoplates could be obtained at this lower temperature and in a completely different reaction batches.

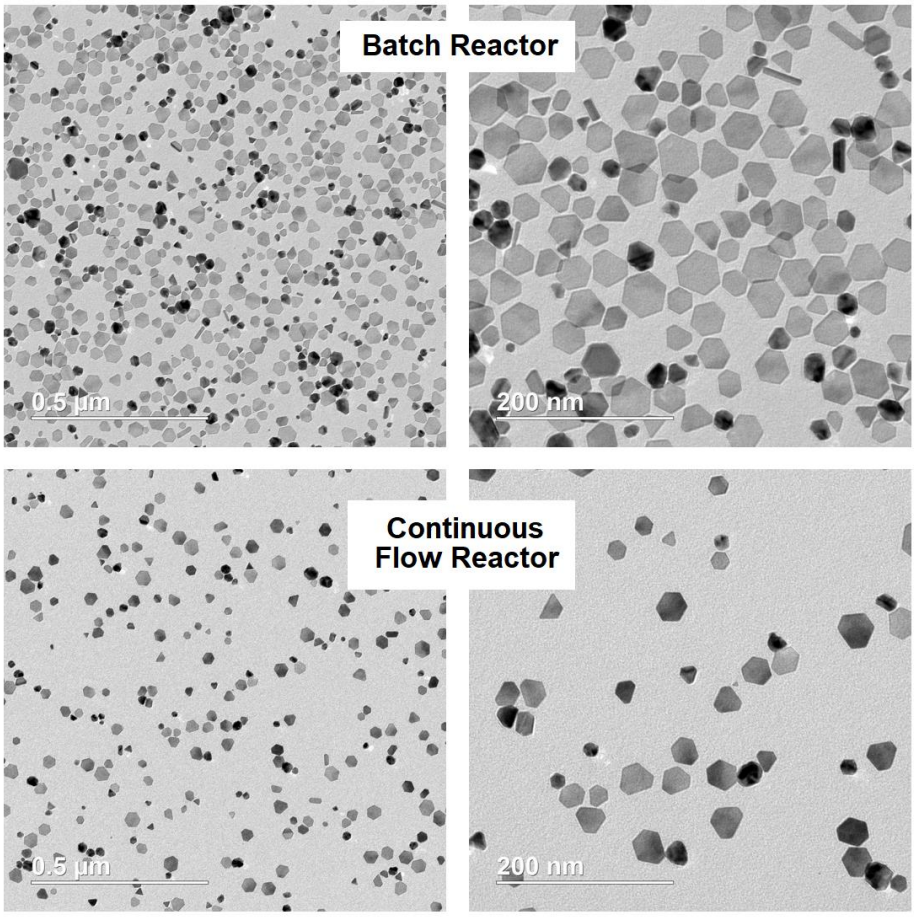

Figure 2.9. TEM images of Pd nanoplates obtained in a batch reactor (vial) and a continuous flow system (PTFE tube), respectively. Note that the protocol was slightly modified to accommodate the continuous flow synthesis by reducing the temperature from 100 to 80 °C.

2.3 Conclusion

I have demonstrated a robust synthesis of Pd nanoplates using hydroxylamine as the reducing agent. By characterizing the products obtained at different time points, I found

that the internal defect structure of the Pd nanoplates was formed at the early stage of a synthesis, which provided seeds with stacking-faults for the subsequent growth into highly anisotropic, planar, well-defined hexagonal nanoplates. It is reasonable to consider this synthesis a *robust* one because I found that rather drastic changes to the experimental parameters such as pH, temperature, and chemical environment did not significantly alter the nucleation process (*e.g.*, formation of internal defect structure) and overall shape (*e.g.*, hexagonal) of the final products. In addition, the protocol could even be adapted for use in a continuous flow reactor to scale up the production of high quality Pd nanoplates. Taken together, I strongly believe that this particular system can serve as a model reaction for future experiments with an aim to elucidate the mysterious mechanisms occurring during the homogeneous nucleation of both stacking-fault-lined structures and other unique defect containing nanocrystals.

2.4 Experimental Section

Chemicals. Sodium tetrachloropalladate(II) (Na_2PdCl_4, 99.99%, Acros Organics), hydroxylamine hydrochloride ($NH_2OH{\cdot}HCl$, 99% Sigma-Aldrich), poly(vinyl pyrrolidone) (PVP, MW≈55,000, Sigma-Aldrich), and citric acid (CA, 99.5%, Sigma-Aldrich). De-ionized (DI) water with a resistivity of 18.2 MΩ·cm at room temperature was used throughout the experiments.

Synthesis of Pd Nanoplates in a Batch Reactor. In a standard protocol, an aqueous solution containing 100 mg PVP, 50 μL of $NH_2OH{\cdot}HCl$ (30 mM), and 1.0 mL of CA (100 mM) was prepared to a total volume of 8.0 mL. Subsequently, 1.0 mL of an aqueous solution of Na_2PdCl_4 (12 mM) was added in one shot at room temperature under magnetic

stirring. The reaction was placed in an oil bath at 100 ºC and allowed to proceed for 3 h. The final product was collected by centrifugation using the Eppendorf Centrifuge 5430 at 17,000 rpm for 20 min, and then re-dispersed in water. The final product was washed three times by repeating the centrifugation protocol.

Synthesis of Pd Nanoplates in Continuous Flow. Similar to the standard protocol, an aqueous solution containing 100 mg PVP, 50 μL of $NH_2OH{\cdot}HCl$ (30 mM), and 1.0 mL of CA (100 mM) was prepared to a total volume of 8.0 mL. Subsequently, 1.0 mL of an aqueous solution of Na_2PdCl_4 (12 mM) was added in one shot at room temperature under magnetic stirring. The prepared reaction solution was injected using a syringe pump (2 mL min^{-1}) to a PVC tubing system preheated at 80 ºC (see references [24] and [25] for a visual description of the system, and the dimensions of the tubing). Once the reaction solution was completely injected in the tubing, it was allowed to proceed for 3 h. The final product was collected by injecting air to the PVC tubing and place in centrifugation vials for washing. I used the Eppendorf Centrifuge 5430 operated at 17,000 rpm for 20 min. The product was then re-dispersed in water and washed three times following the same parameters.

Kinetic Studies. The reduction kinetics were determined by measuring the concentration of Pd(II) ions remaining in the reaction solution at different time points of a synthesis. Two methods were used to determine the kinetics: *i*) analyzing a number of identically prepared vials, and *ii*) analyzing aliquots sampled from a single vial. In the first method, a number of identically prepared reaction vials were placed simultaneously in the same oil bath. Then, one reaction vial was removed from the oil bath at a specific time point (*e.g.*, 15, 30, 60 min) and the reaction was quenched by placing the vial in an ice bath. Aliquots of 0.2

mL were taken from the quenched reaction solution and injected into 0.8 mL of aqueous KBr (500 mg/mL). In the second method, aliquots of 0.2 mL were taken from a single vial (note: the vial was frequently uncapped in this case) and injected into 0.8 mL of cold KBr solution (500 mg/mL) to quench the reaction. Because of the high concentration of bromide ions, the unreacted Pd(II) ions quickly undergo ligand exchange to generate the complex of $PdBr_4^{2-}$ for UV-vis analysis.[12] The aliquot obtained from both methods were centrifuged at 55,000 rpm for 30 min to remove all the Pd nanoparticles, and the supernatants were used to measure the concentrations of $PdBr_4^{2-}$ ions by UV–vis spectroscopy. The measured absorbance at 332 nm and a calibration curve (see reference [12] for the procedure) were used to determine the concentrations of the remaining Pd(II) ions at different reaction times. Each data point represents two repeated measurements.

Characterization. Samples were characterized using a transmission electron microscope (Hitachi HT7700) operated at 120 kV. High-resolution transmission electron microscopy (HRTEM) was performed on an aberration-corrected FEI Titan S 80-300 STEM/TEM microscope equipped with a Gatan OneView camera at an acceleration voltage of 300 kV. All samples for HRTEM were prepared by drop casting 8 µL of the as-prepared aqueous dispersions of Pd nanoplates on lacey carbon-coated copper grids. The X-ray diffraction (XRD) analysis was performed using the Empyrean PANalytical system with an K-Alpha1 radiation source of wavelength 1.54 Å, operated at 45 kV. The sample was prepared by drop casting the washed aqueous suspension of Pd nanoplates onto a silica wafer and then dried at room temperature overnight. The data was analyzed using Origin software, a background subtraction was performed to present the XRD data in this report. The analysis of the reduction kinetics was performed using an UV-vis spectrophotometer (Cary 60,

Agilent Technology) in the spectral region of 200−800 nm. The pH measurements were performed using a Fisher Scientific Accumet Basic AB15 pH meter.

2.5 Notes to Chapter 2

This chapter was adapted from "Facile, Robust, Scalable Synthesis of Pd Nanoplates with Hydroxylamine as a Reducing Agent and the Mechanistic Insights from Kinetic Analysis" submitted to the *Journal of Materials Chemistry C*. [26]

2.6 References

[1] C. Langhammer, Z. Yuan, I. Zoric and B. Kasemo, *Nano Lett.*, 2006, 6, 833.

[2] J. R. Krenn, *Nature Mater.*, 2003, 2, 210.

[3] M. B. Kimmey, X. Li and Y. Xia, *Nano Lett.*, 2005, 5, 473.

[4] D. M. Schaadt, B. Feng and E. T. Yu, *Appl. Phys. Lett.*, 2005, 86, 063106.

[5] E. M. Larsson, C. Langhammer, I. Zoric and B. Kasemo, *Science*, 2009, 326, 1091.

[6] Y. Xia, Y. Xiong, B. Lim and S. E. Skrabalak, *Angew. Chem. Int. Ed.*, 2009, 48, 60.

[7] Y. Xiong, J. M. McLellan, J. Chen, Y. Yin, Z.-Y. Li and Y. Xia, *J. Am. Chem. Soc.*, 2005, 127, 17118.

[8] Y. Xiong, I. Washio, J. Chen, H. Cai, Z.-Y. Li and Y. Xia, *Langmuir*, 2006, 22, 8563.

[9] X. Huang, S. Tang, X. Mu, Y. Dai, G. Chen, Z. Zhou, F. Ruan, Z. Yang and N. Zheng, *Nat. Nanotechnol.*, 2011, 6, 28.

[10] Y. Xiong and Y. Xia, *Adv. Mater.*, 2007, 19, 3385.

[11] T.-H. Yang, K. D. Gilroy and Y. Xia, *Chem. Sci.*, 2017, 8, 6730.

[12] Y. Wang, H.-C. Peng, J. Liu, C. Z. Huang and Y. Xia, *Nano Lett.*, 2015, 12, 1445.

[13] W. Niu, L. Zhang and G. Xu, *ACS Nano*, 2010, 4, 1987.

[14] K. D. Gilroy, H.-C. Peng, X. Yang, A. Ruditskiy and Y. Xia. *Chem. Commun.*, 2017, 53, 4530.

[15] K. D. Gilroy, A. O. Elnabawy, T.-H. Yang, L. T. Roling, J. Howe, M. Mavrikakis and Y. Xia, *Nano Lett*., 2017, 17, 3655.

[16] K. D. Gilroy, J. Puibasset, M. Vara and Y. Xia, *Angew. Chem.*, 2017, 129, 8773.

[17] H. Li, G. Chen, H. Yang, X. Wang, J. Liang, P. Liu, M. Chen and N. Zheng, *Angew. Chem. Int. Ed.*, 2013, 52, 8368.

[18] J. Zeng, J. Tao, W. Li, J. Grant, P. Wang, Y. Zhu and Y. Xia, *Chem. Asian J.*, 2011, 6, 376.

[19] T.-H. Yang, S. Zhou, K. D. Gilroy, L. Figueroa-Cosme, Y.-H. Lee, J.-M. Wu and Y. Xia, *Proc. Natl. Acad. Sci*. *USA,* 2018, **114**, 13619.

[20] G. Bengtsson, S. Fronæus and L. Bengtsson-Kloo, *J. Chem. Soc.*, *Dalton Trans.*, 2002, 2548.

[21] J. Li and X. Lin, *Sensor Actuat. B-Chem.*, 2007, **126**, 527.

[22] M. D. Johnson and B. J. Hornstein, *Inorg. Chem.*, 2003, **42**, 6923.

[23] J. Yue, Z. Du and M. Shao, *Chem. Phys. Lett.*, 2016, **659**, 159.

[24] L. Zhang, Y. Xia, *Adv. Mater*. 2014, **26**, 2600.

[25] L. Zhang, G. Nui, N. Lu, J. Wang, L. Tong, L. Wang, M. Kim, Y. Xia, *Nano Lett*. 2014, **14**, 6626.

[26] L. Figueroa-Cosme, Z. D. Hood, K. D. Gilroy, Y. Xia, *J. Mater. Chem. C*, 2018, Accepted.

CHAPTER 3

SYNTHESIS OF PALLADIUM NANOSCALE OCTAHEDRA THROUGH A ONE-POT, DUAL-REDUCTANT ROUTE AND THE KINETIC ANALYSIS

3.1 Introduction

Noble-metal nanocrystals are central to a wide variety of applications ranging from photonics to catalysis, energy harvesting/conversion, and medicine.[1-9] An excellent example can be found in Pd nanocrystals, which are currently used in the catalytic converters to assist the conversion of hazardous gases such as CO and NO into less harmful products such as CO_2 and N_2.[10-11] They are also used for catalyzing a myriad of organic reactions, including those involved in hydrogenation, dehydrogenation, carbon-carbon bonding formation (*e.g.*, Heck/Suzuki coupling), and petroleum cracking, as well as for the next-generation hydrogen storage and sensing devices.[12-16]

It is well-known that reducing the size of a metal to the nanoscale can significantly alter its properties and even generate new features.[17,18] In a bulk crystal, the relative contribution of surface atoms is minimal, but when shrunk to the nanoscale, the surface-to-volume ratio increases so drastically that the participation of surface atoms becomes dominant and invaluable.[17,18] However, simply reducing the size of a metal to the nanoscale may not be the most efficient way to tailor its properties. Experimental and theoretical studies have established that the shape of a nanocrystal can greatly affect its electronic, optical, mechanical, and magnetic properties.[19-22] For example, Liu and coworkers demonstrated that Pd octahedra enclosed by {111} facets were more efficient than Pd cubes enclosed by {100} facets for the aerobic oxidation of 5-hydroxymethyl-2-

furfural.[23] In another example, Guo and coworkers discovered that Pd nanocrystals covered by {111} facets were active toward the oxidative coupling of CO to dimethyl oxalate, while those encased by {100} facets were largely inactive for the same reaction.[24] These and many other examples clearly demonstrate the unique correlation between the properties of nanocrystals and their shapes.[23-25]

Wet-chemical methods for generating nanocrystals with controlled shapes have traditionally involved the reduction of a metal precursor by a single reductant in the presence of a capping agent and/or colloidal stabilizer.[26,27] For Pd, Huang and coworkers developed a one-pot method for the seedless growth of nanosheets, concave tetrahedra, and tetrahedra by leveraging on a unique combination of reductant and water.[28-30] Similarly, Zou and coworkers were able to generate nanorods without involving pre-formed seeds by using ascorbic acid as a reductant in the presence of two different capping agents.[28-30] Despite the remarkable progress in synthesizing Pd nanocrystals with different shapes, it remains a challenge to produce Pd octahedral nanocrystals using a one-pot approach. In an early study, Xia group demonstrated the synthesis of Pd octahedra in one pot by reducing a Pd(II) precursor with PVP, and a similar approach was also reported by Zhao and coworkers.[31,32] As one of the major problems, a relatively long reaction times (up to 26 h) had to be used and both studies only reported octahedra with edge lengths in the range of 20−23 nm. Also, in both syntheses, the nucleation and growth processes tended to be mixed in the same reaction solution, making it difficult to separately optimize the reduction kinetics necessary for controlling nucleation and for directing the shape evolution during a growth process.

To minimize the variations and, at the same time, avoid the complicated nucleation step, many groups have adopted the seed-mediated approach.[33-36] In this route, atoms are deposited onto the surface of pre-formed seeds under specific experimental conditions to promote the formation of a particular shape. Although seed-mediated growth allows for a good control over the nanocrystal shape, it has several intrinsic limitations. From the perspective of experimental design, seed-mediated growth requires at least two steps: *i*) preparation and purification of seeds and *ii*) growth of the seeds into nanocrystals, followed by further purification. The throughputs of most seed-mediated syntheses are limited to *ca.* 1−2 mg per batch, which is barely enough for extensive characterization, and far from the amount necessary for industrial use. In addition, the resultant nanocrystals are always larger than the seeds, making it impractical to obtain nanocrystals smaller than the seeds. Taken together, it would be advantageous to have a simple method that can tightly control both the nucleation and growth processes in a one-pot setting.

To address the aforementioned issues associated with seed-mediated growth, several groups have explored the concept of co-reductants in a one-pot setting.[37,38] To this end, Han and coworkers reported the use of ascorbic acid and hydrazine as co-reductants to synthesize trimetallic core-shell nanoparticles. In this work, they suggested that the metal-ligand complexes, together with the co-reductants, played an important role in controlling the formation of well-defined trimetallic structures.[37] However, the complicated reduction kinetics involving different metal precursors and reductants imposes a challenge to elucidate the formation mechanism of the nanocrystals.

Herein, I report a one-pot approach to the synthesis of Pd octahedra by introducing both strong and weak reductants in proper proportions to manipulate the temporal profile

of reduction. My central hypothesis is that the strong reductant can take care of the initial nucleation process to generate single-crystal seeds, while the weak reductant will provide the slow reduction necessary for the growth of the single-crystal seeds into octahedra. Figure 3.1 shows a schematic of the concept. In essence, I aim to produce Pd octahedra using judicially selected dual reductants to ensure optimal reduction kinetics for both the nucleation and growth processes in a one-pot setting. I illustrate this concept using a number of different combinations of strong and weak reductants to achieve the production of Pd octahedra in high yields.

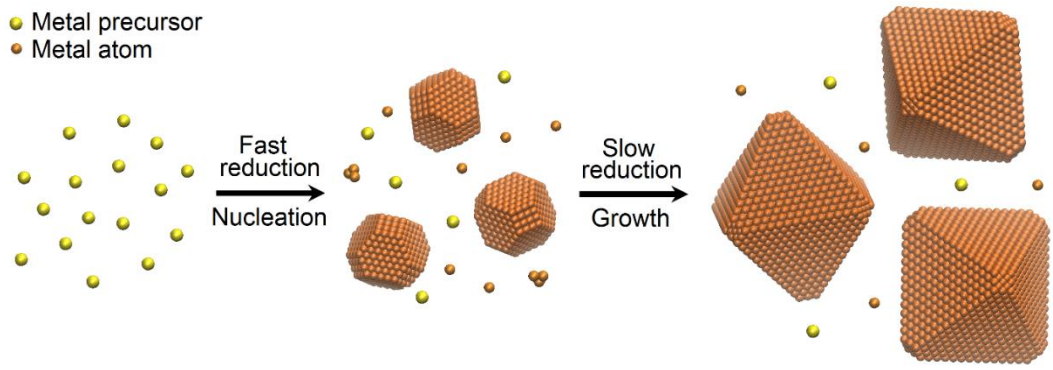

Figure 3.1. Schematic illustration of the two major steps involved in a dual-reductant approach: *i*) quick reduction of a Pd(II) precursor by the strong reductant for the production of Pd atoms that undergo nucleation to produce the seeds, and *ii*) slow reduction of the same precursor by the weak reductant to generate Pd atoms for their deposition onto the seeds.

3.2 Results and Discussion

I decide to use a metal precursor based on tetrachloropalladate ($PdCl_4^{2-}$) because it has been extensively explored in literature for the synthesis of Pd nanocrystals with a broad range of shapes and sizes.[39,40] More importantly, this precursor has also been used for the elucidation of reduction pathways and reaction kinetics in both aqueous and polyol media.[41-44] In addition, the $PdCl_4^{2-}$ complex has a well-known complexation chemistry

with solvent molecules such as water and other ligands, and it is feasible to quantitatively measure the concentrations of these complexes using ultraviolet-visible (UV/vis) spectroscopy.[41-45] I rely on the use of citric acid (CA) as both a weak reductant and a capping agent to promote the formation and stabilization of Pd(111) surface.[46,47] As for the strong reductant, I concentrate on ascorbic acid (HAsc), sodium ascorbate (NaAsc), hydroquinone (HQ), and ethanol (EtOH). All of them have been successively applied to the syntheses of Pd nanocrystals.[48-50] Sodium citrate is also a possible choice for the strong redundant, but I cannot use it in the present work because of the involvement of its conjugate acid, CA, in all the protocols. The built-in equilibrium between these two species makes it very challenging to separately adjust their concentrations.

It was recently reported that the production of single-crystal, multiply twinned, and stacking-fault-lined seeds could be controlled by tuning the initial reduction rate of a Pd(II) precursor from fast to moderate and slow.[41-45] With these results in mind, my strategy is to introduce a strong reductant in a limited quantity so that a fixed number of single-crystal seeds will be generated at the initial stage of a synthesis. Once the seeds have been formed and the strong reductant has been depleted, the remaining precursor will be reduced by the weak reductant to ensure the necessary growth kinetics for the formation of Pd octahedra. In a typical synthesis, I pre-heated an aqueous solution containing a strong reductant (*e.g.*, HAsc), a weak reductant (*e.g.*, CA), and a colloidal stabilizer such as poly(vinyl pyrrolidone) (PVP). After 10 min of pre-heating, a specific amount of aqueous Na_2PdCl_4 is added into the reaction mixture by a one-shot injection. The reaction is allowed to continue for 3 h. The specific concentrations of the reagents are summarized in Table 3.1.

Table 3.1. Summary of experimental conditions for the synthesis of Pd octahedra through the combination of a strong reductant with citric acid.

Protocol	Strong reductant	CA (mM)	PVP (mg)	Precursor Na_2PdCl_4	Total Vol (mL)	Temp (°C)
1	1.0 mL (5 mM HAsc)	400	65	1.0 mL (68 mM)	6	80
2	1.0 mL (5 mM NaAsc)	400	65	1.0 mL (68 mM)	6	80
3	0.1 mL (30 mM HQ)	100	100	1.0 mL (12 mM)	13	100
4	3 mL EtOH (200 proof)	85	100	3.0 mL (68 mM)	11	80

As shown in Figure 3.2, Pd octahedra were indeed formed in high purity using each one of the strong-weak pairs. When using HAsc-CA, NaAsc-CA, HQ-CA, and EtOH-CA pairs, the resultant Pd octahedra had average edge lengths around 9, 8, 12, and 6 nm, respectively. In the current setting, the throughputs of the syntheses involving HAsc, NaAsc, and HQ were comparable to the typical synthesis involving seed-mediated growth (1−2 mg of Pd metal), while the throughput of the EtOH-based system was about nine times as high as (*ca.* 18 mg of Pd metal). Since the nucleation and growth steps are separated from each other, it should be much easier to increase the throughput of a dual-reductant protocol than the conventional methods.

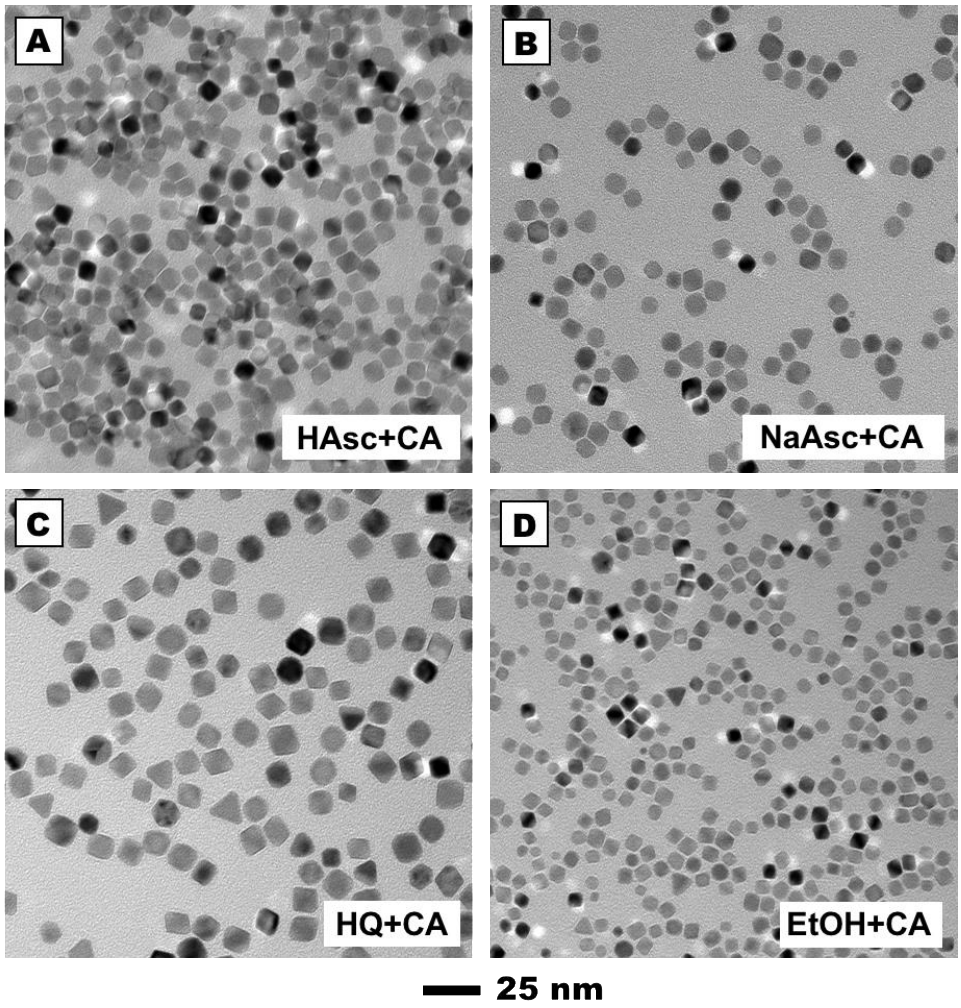

Figure 3.2. TEM images of Pd octahedra synthesized using four different pairs of strong and weak reductants, including (A) ascorbic acid and citric acid (HAsc + CA); (B) sodium ascorbate and citric acid (NaAsc + CA); (C) hydroquinone and citric acid (HQ + CA); and (D) ethanol and citric acid (EtOH + CA).

As stated in my hypothesis, I believed the strong reductant was responsible for the formation of single-crystal seeds. To further corroborate the internal defect structure of the seeds, I used high-angle annular dark-field scanning TEM (HAADF-STEM) to analyze the products at 10 min and 3 h into the synthesis. Figure 3.3 shows the data for the HAsc-CA pair while a detailed analysis of the Pd seeds involved in all other combinations of reductants can be found in Figure 3.4.

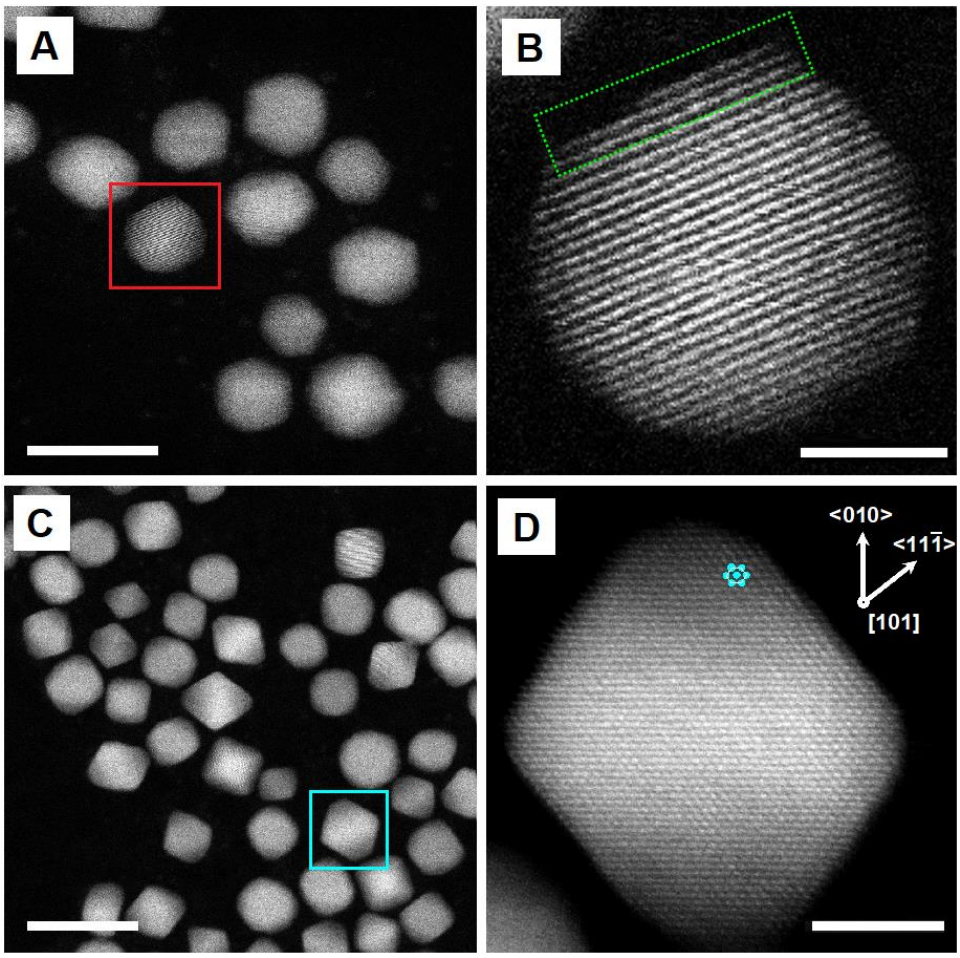

Figure 3.3. HAADF-STEM images showing the Pd nanocrystals generated using the HAsc + CA system: (A) Pd seeds formed after 10 min into the synthesis (scale bar: 10 nm); (B) an individual Pd seed from (A), as marked by the red box, at a higher magnification (scale bar: 2 nm); (C) octahedral nanocrystals formed after 3 h into the synthesis (scale bar: 20 nm); and (D) an individual Pd octahedron in (C), as marked by the blue box, oriented along its [110]-zone axis (scale bar: 5 nm). The particle shown in (D) was slightly rotated clockwise relative to the particle boxed in (C). The green box in (B) shows an incomplete layer formed along the <111> direction. The blue dots in (D) mark the positions of the atoms to demonstrate that the octahedron was oriented along the [101] direction.

As shown by the low magnification image in Figure 3.3A, Pd nanocrystals with a more or less spherical shape were formed in the early stage of the synthesis. I further examined an individual Pd seed, as highlighted in the red box, to gain a more detailed understanding of the structure (Figure 3.3B). A single-crystal lattice is observed in the

STEM image. Interestingly, the HAADF-STEM image also suggested that the formation of the {111} facets followed the Frank-van der Merwe or layer-by-layer growth mode, as highlighted by the green box in Figure 3.3B. This image not only offers experimental evidence as to how the Pd octahedra were formed in my syntheses but also supports the aforementioned argument in terms of growth mode for the formation of octahedra.

Figure 3.3C show a STEM image of the final product obtained at 3 h into the synthesis. I further analyze a single nanocrystal as highlighted in the blue box. The Pd octahedron in Figure 3.3D was oriented along the [101] direction, allowing for the calculation of the *d*-spacing for both (111) and (100) planes. By averaging more than 10 lattices spacing (Figure 3.5A), I found that the $d_{(111)}$ and $d_{(100)}$ values were 2.22 Å and 1.91 Å, respectively. To further validate these results, I recorded XRD patterns from both the seeds and octahedra (Figure 3.5B) and obtained consistent values for the $d_{(111)}$ and $d_{(200)}$ spacing (2.25 Å and 1.95 Å, respectively).

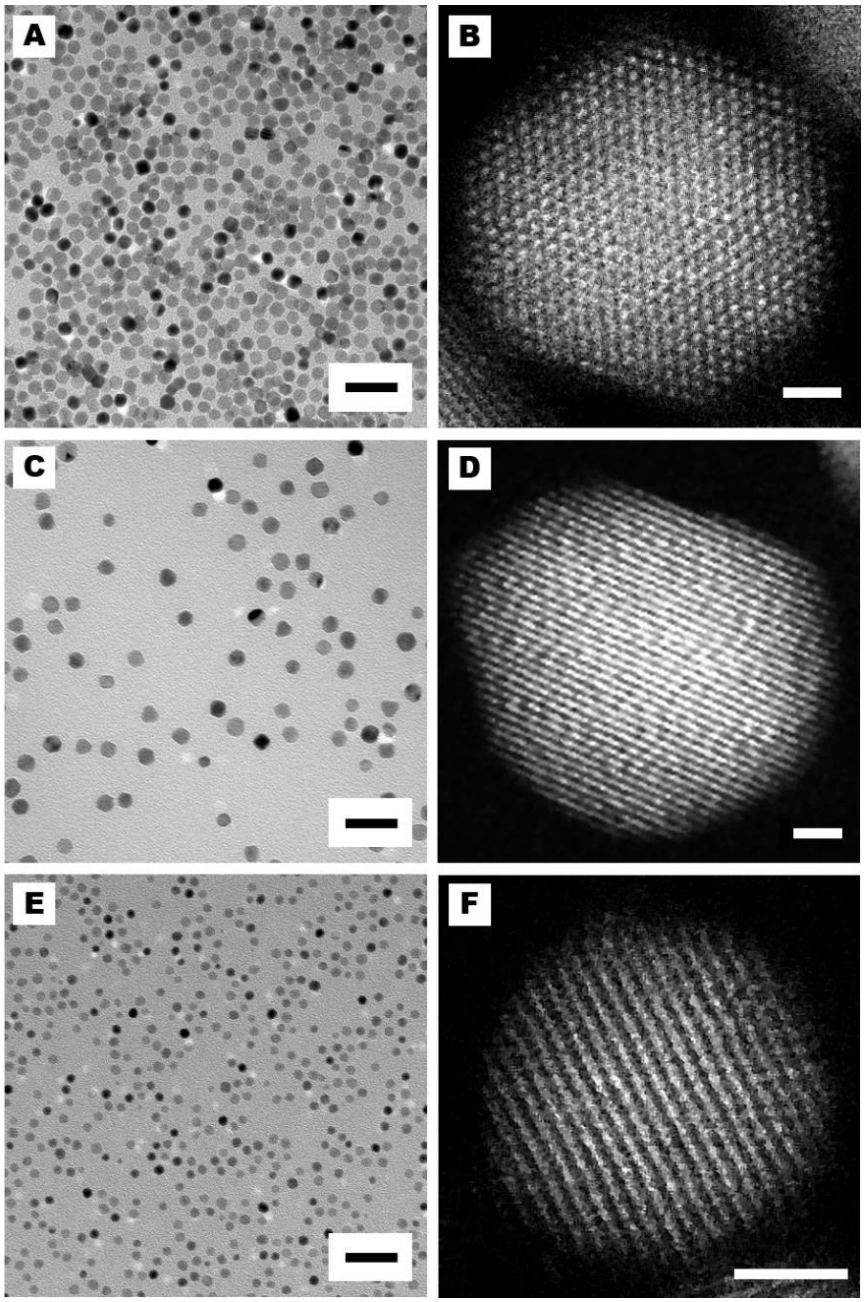

Figure 3.4. TEM and HAADF-STEM images showing Pd seeds formed after 10 min into the syntheses that involve: (A, B) sodium ascorbate, (C, D) hydroquinone, and (E, F) ethanol, respectively, with citric acid serving as a weak reductant. The scale bars are 20 nm in (A), (C) and (E), and 1 nm in (B), (D) and (F).

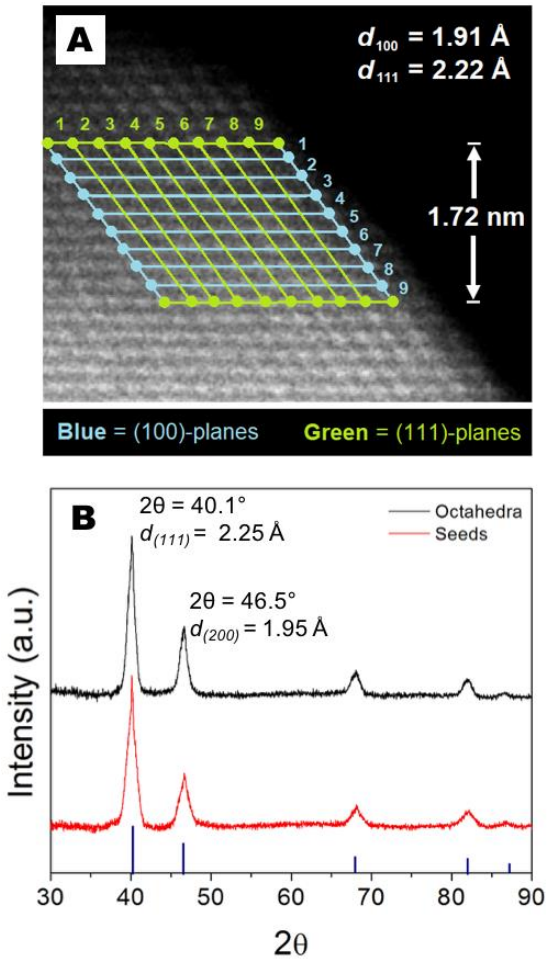

Figure 3.5. Measurements of the *d*-spacing for Pd octahedra obtained using HAsc + CA pair. (A) High-magnification HAADF-STEM image of a Pd octahedron oriented along the [101] zone axis. The green dots and lines represent atoms and planes respectively, along the [111] direction. The blue dots and lines represent atoms and planes respectively, along the [100] direction. (B) X-ray diffraction pattern of the Pd seeds (red) and the final octahedra (black).

I was curious to know if both reductants were needed to form the Pd octahedra. For this reason, I attempted the synthesis using each one of the individual reductants and then compared the results with the dual-reductant approach. For consistency, I selected the HAsc-CA system as a case study and summarized the results in Figure 3.6. In simple terms, I performed control experiments with the use of: *i*) HAsc as a single reductant at a concentration of 5 mM, *ii*) CA as a single reductant at a concentration of 400 mM, and *iii*)

a combination of HAsc (5 mM) and CA (400 mM). I monitored the progress of each synthesis using UV/vis spectroscopy and imaged the products by TEM. When HAsc was used as the sole reductant (case *i*, Figure 3.6A), the UV/vis spectra showed continuous decrease in peak intensity with the reaction time. The change started to occur within the first few minutes of the synthesis and it could be attributed to the reduction of Pd(II) by HAsc. However, 1.6 h after the reaction had been initiated, there was no longer any major change to the absorbance of the solution, suggesting the termination of reduction. This result was kind of expected because of the depletion of HAsc that was used at a relatively low concentration. Figure 3.6B shows TEM image of the Pd nanocrystals formed in the presence of HAsc only, which displayed neither shape nor size control for this synthesis. Figure 3.6, C and D, shows the results for CA when it was used as a sole reductant. The UV/vis spectra showed no significant changes even over a course of 6 h, confirming that the reduction power of CA is significantly weaker than HAsc. The Pd nanocrystals exhibited a spherical shape. Remarkably, when HAsc and CA were used simultaneously, the reaction reached completion after about 3 h (Figures 3.6E) and Pd octahedra were obtained (Figure 3.6F). These results strongly suggest that the simultaneous use of both strong and weak reductants is necessary for the formation of Pd octahedra. Figure 3.7 further supports this argument by demonstrating the missing of shape and size controls over the Pd nanocrystals when the rest of the strong reductants, NaAsc, HQ, and EtOH, were used alone without involving CA.

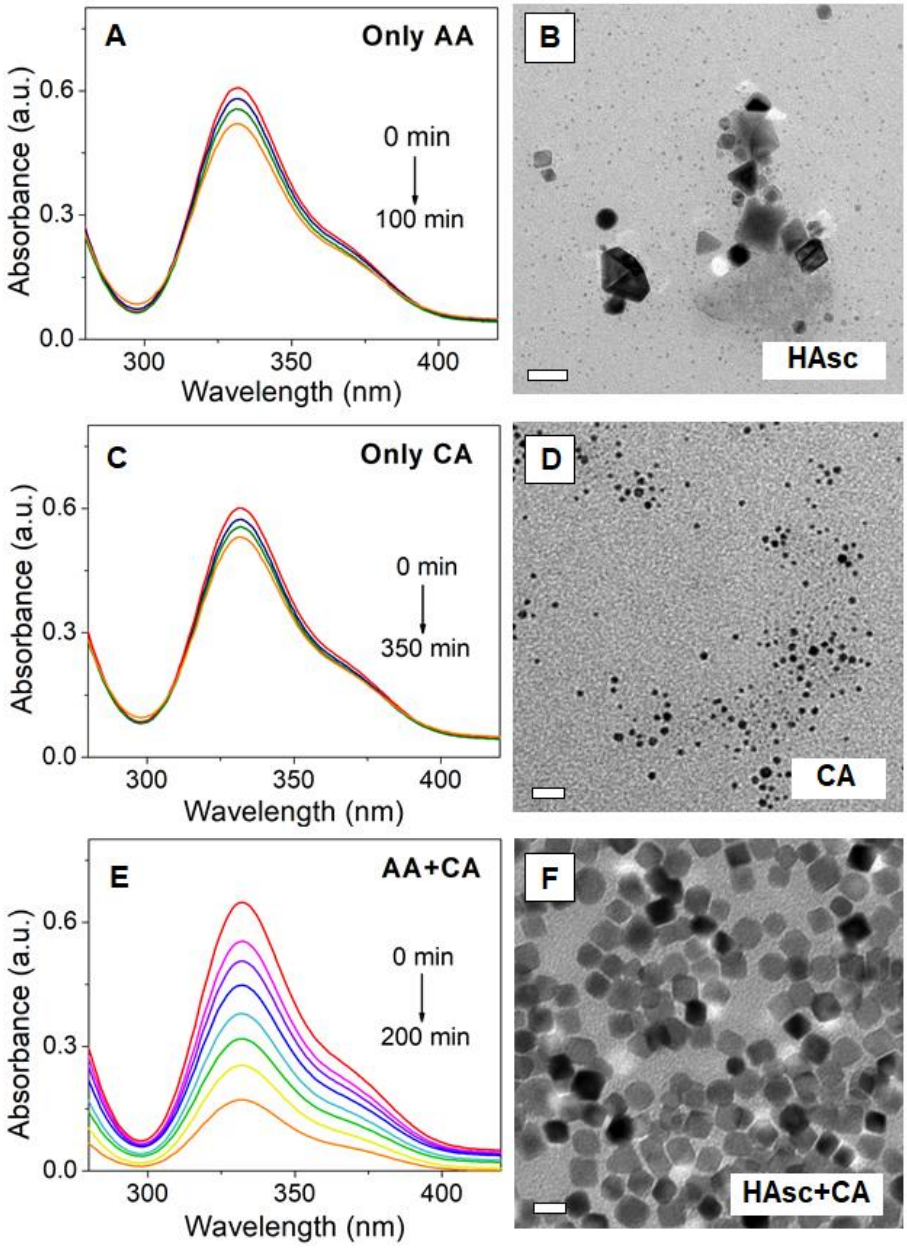

Figure 3.6. (A) UV/vis spectra tracking the changes in absorbance for the Pd(II) precursor over the course of 100 min when HAsc was used as the sole reductant and (B) the corresponding products of polydispersed Pd nanoparticles with no shape control (scale bar: 25 nm). (C) UV/vis spectra showing the changes in absorbance over the course of 350 min when CA was used as the sole reductant and (D) the corresponding products of Pd nanoparticles with moderately good uniformity but with no shape control (scale bar: 100 nm). (E) UV/vis spectra showing a large drop in absorbance over the course of 200 min when HAsc and CA were used simultaneously and (F) the corresponding products of Pd octahedra with an excellent shape control (scale bar: 10 nm).

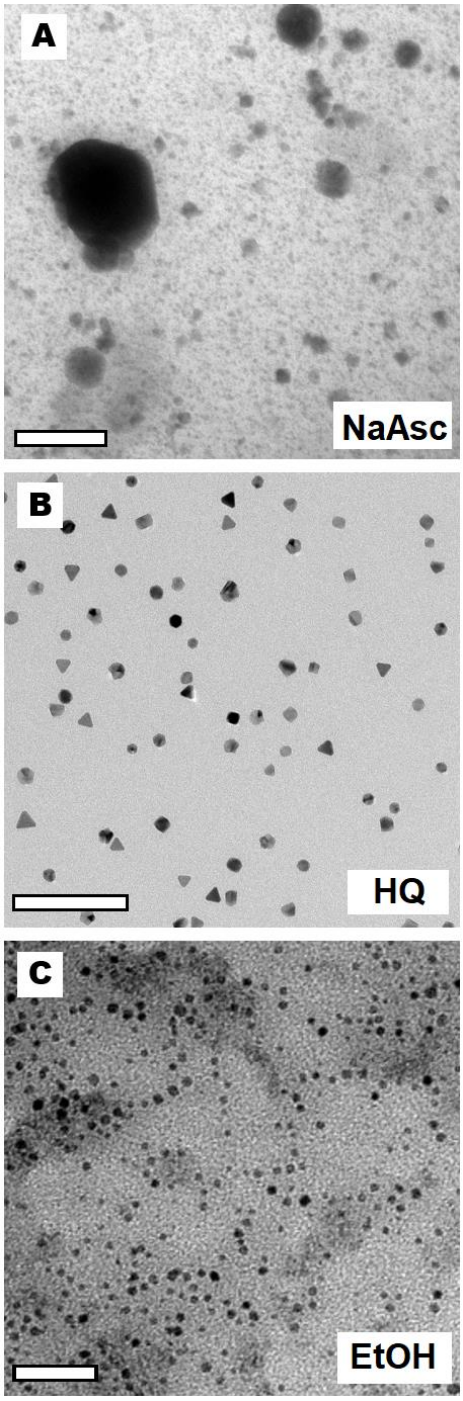

Figure 3.7. TEM images of Pd nanocrystals obtained when (A) NaAsc, (B) HQ, and (C) EtOH were used alone as the reductant in absence of citric acid. The scale bars are 100 nm in (A) and (B), and 200 nm in (C), respectively.

It should be pointed out that "strong" and "weak" are relative terms. These descriptions become relevant when the reductants under comparison show different tendencies toward the reduction of a metal precursor. With this in mind, I wanted to quantitatively validate that one reductant was acting more strongly than the other one. To do so, I performed kinetic measurements on the individual reductants under similar conditions and measured their reduction rate constants to compare their relative reducing powers at three different temperatures (50, 60, 70 ºC). The raw data presented in Figure 3.8 and 3.9, and Table 3.2, were analyzed in the form of Arrhenius log plot, which was obtained by taking the natural logarithm of the Arrhenius equation:

$$k = Ae^{-E_a/RT} \qquad (1)$$

where k is the reduction rate constant, A is a pre-factor sometimes referred to as the collision frequency factor, E_a is the activation energy of the reaction, R is the gas constant, and T is the temperature in Kelvin.

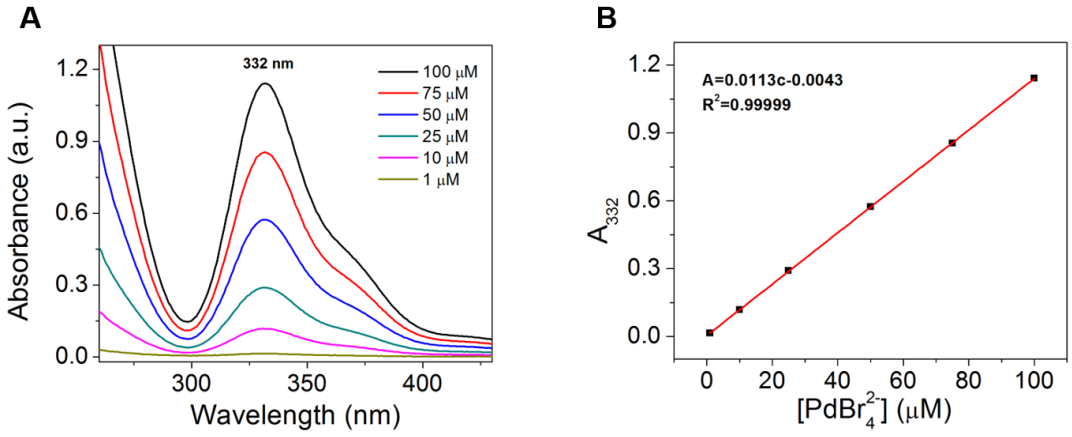

Figure 3.8. (A) UV/vis spectra of $PdBr_4^{2-}$ stock solutions prepared with different concentrations. (B) Plot showing the linear dependence between the absorbance at 332 nm and the concentration of $[PdBr_4]^{2-}$. This calibration curve was used to determine the concentration of Pd(II) in the kinetic measurements.

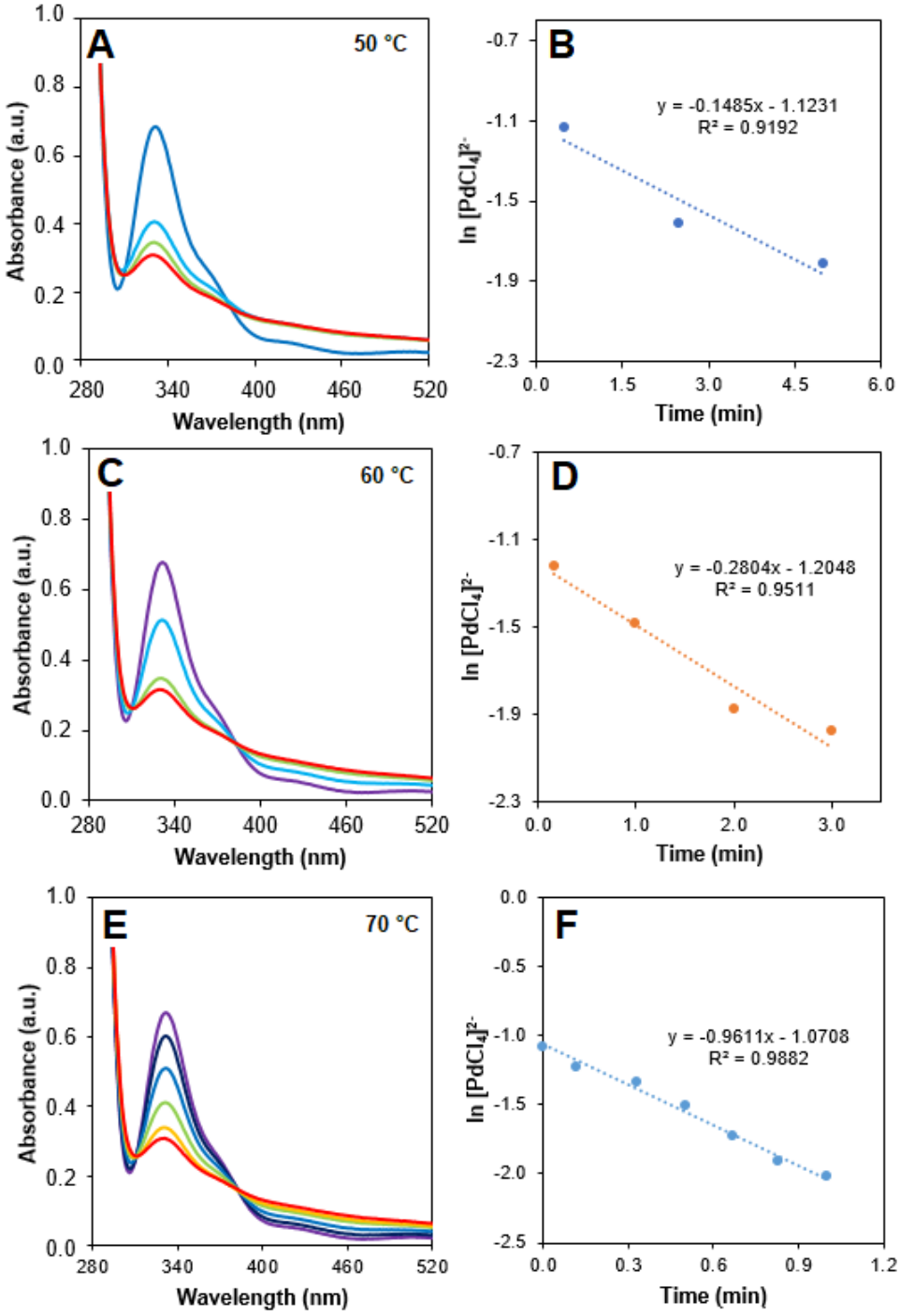

Figure 3.9. UV/vis spectra showing the change in absorbance due to the reduction of Pd(II) ions by HAsc (left-side panels), and the log-plot showing the concentration of the remaining Pd(II) precursor as a function of time (right-side panels) recorded at (A and B) 50, (C and D) 60, and (E and F) 70 °C.

Table 3.2. Kinetic parameters for each of the strong reductants.

Reductant	Temp (°C)	$\ln[PdCl_4]^{2-} = mt + b$	R^2
Sodium L-Ascorbate	50	$-0.275t - 0.8882$	0.9357
	60	$-0.707t - 0.8206$	0.9397
	70	$-0.415t - 0.9708$	0.9625
Hydroquinone	50	$-0.016t - 0.9954$	0.9785
	60	$-0.029t - 0.9954$	0.9277
	70	$-0.142t - 0.9138$	0.9442
Ethanol	50	$-0.005t + 4.9734$	0.9933
	60	$-0.011t + 5.2894$	0.9903
	70	$-0.029t + 5.866$	0.9594

As shown in Figure 3.10 and Table 3.3, NaAsc, HAsc, and HQ exhibited similar behavior toward the reduction of Na_2PdCl_4, while EtOH presented significantly smaller *k* values at all the temperatures. These results are consistent with what was observed in the dual-reductant approach: an excess amount of EtOH was needed in order to obtain Pd octahedra. In the case of CA, the reduction kinetics was extremely slow at all the tested temperatures. As shown in Figure 3.11, there was essentially no change to the concentration of the metal precursor even after 25 h of reaction, suggesting that CA was indeed the weakest reducing agent. I also did a control experiment with surfactant PVP, to evaluate possible complexation with metal precursor. However, I did not see change in the UV/vis spectra of the metal precursor in solution (Figure 3.12)

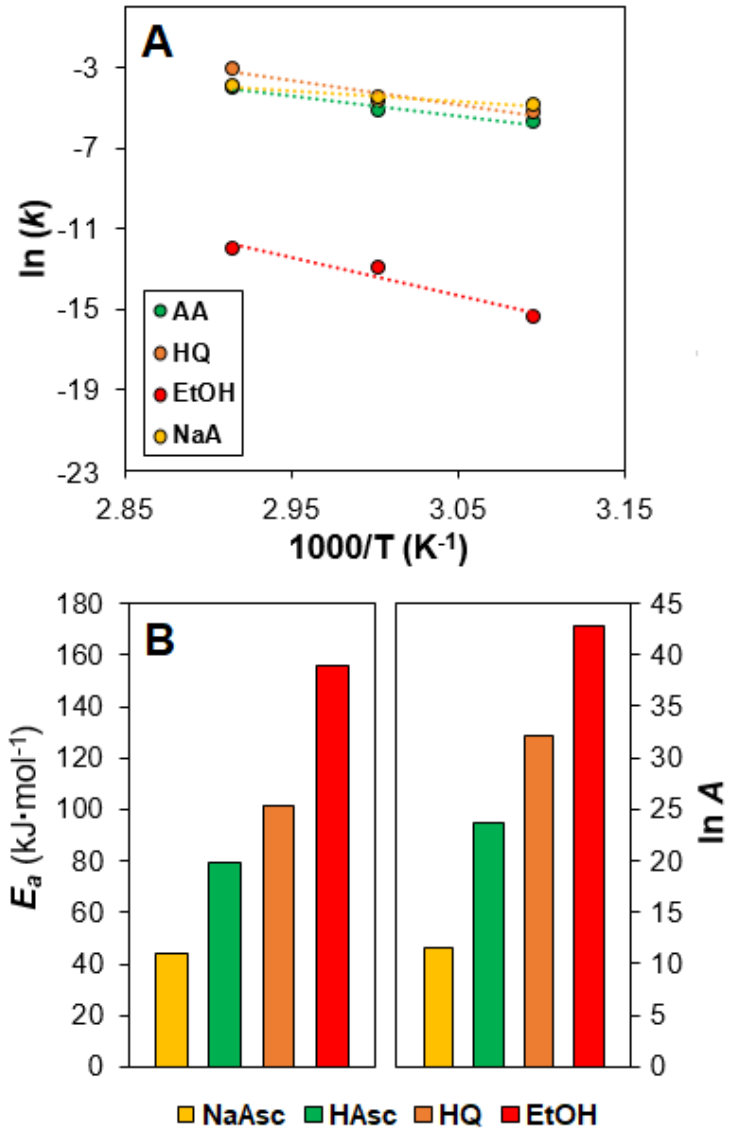

Figure 3.10. (A) Arrhenius log-plot showing the correlation between the rate constant and the reaction temperature. (B) Bar graphs comparing the activation energies and changes in entropy for the different reducing agents.

Table 3.3. The reduction rate constants and initial reduction rates for the strong reductants.

Reductant	Temp (°C)	k (min^{-1})
Sodium L-Ascorbate	50	7.3×10^{-3}
	60	1.1×10^{-2}
	70	1.9×10^{-2}
Ascorbic Acid	50	3.3×10^{-3}
	60	5.9×10^{-3}
	70	2.8×10^{-2}
Hydroquinone	50	5.2×10^{-3}
	60	9.6×10^{-3}
	70	4.73×10^{-2}
Ethanol	50	2.2×10^{-7}
	60	2.4×10^{-6}
	70	6.2×10^{-6}

Useful information can be obtained from the aforementioned Arrhenius plot. By taking the slope and intercept of the line, I derived the activation energy and pre-factor for the individual reduction reaction, see the bar graph in Figure 3.10. As presented in the plot, E_a increased in the order of NaAsc, HAsc, HQ, and EtOH, suggesting that the electron transfer between the reductant molecules and metal ions is energetically much less expensive for NaAsc than for EtOH. It is worth mentioning that in the area of nanocrystal syntheses, the E_a of reaction has not been widely reported. A recent report showed that the E_a for the reduction of K_2PdBr_4 by HAsc varies from 43.4 to 131.1 kJ/mol depending on the exact reaction pathway (surface reduction *vs.* solution reduction).[42] For the reduction of Na_2PdCl_4 by HAsc, my obtained value was 79.1 kJ/mol.

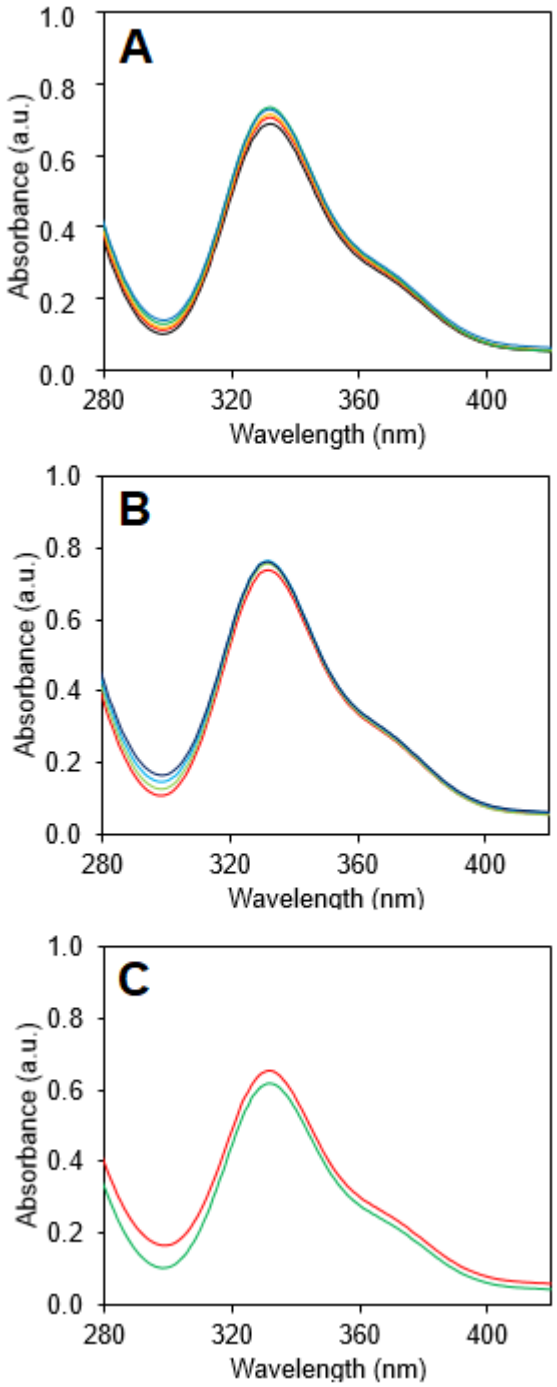

Figure 3.11. UV/vis spectra of a reaction solution containing CA only as the reductant at (A) 50, (B) 60, and (C) 70 ºC. All the reactions were allowed to proceed for up to 25 h.

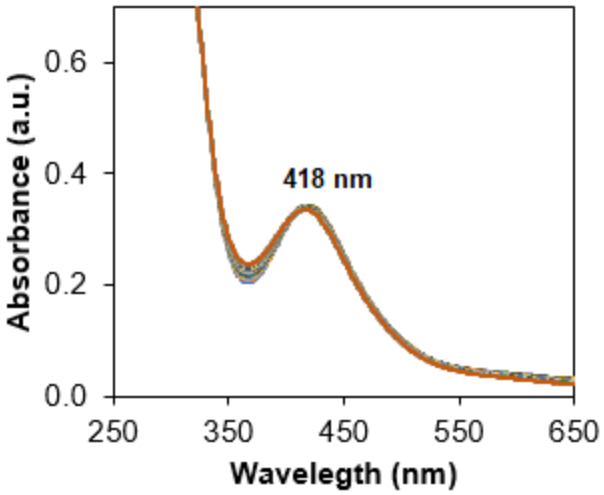

Figure 3.12. UV/vis spectra of a solution containing Na_2PdCl_4 (0.35 mg/mL) and PVP (10 mg/mL). The UV/vis spectra were recorded over a period of 1 h to demonstrate the stability of the Pd(II) precursor in a PVP solution. The absorbance peak at 418 nm suggested the presence of both $[PdCl_3(H_2O)]^-$ and $[PdCl_2(H_2O)_2]^-$. [51,52]

The Arrhenius plot shows a noteworthy trend for the intercept values of the lines. The intercepts correspond to the natural logarithm of the pre-factor, *A*, in the Arrhenius equation (1). In absolute rate theory, the pre-factor is related by equation (2) to the difference in entropy from the initial state to the transition state of a given chemical reaction. This change in entropy is known as the activation entropy (ΔS_a).[53,54]

$$\Delta S_a \propto \ln A \qquad (2)$$

The proportionality between ΔS_a and *A* depends on various factors among them is the type of reaction (*e.g.*, unimolecular, bimolecular, etc.) and the translational, vibrational, and rotational partition functions that describe the state of the system.[53,54] Even though my system is far from simple to be accurately described by the transition state theory, equations (2) offers an interesting perspective about the energetics of the individual reduction reaction. Whereas the activation energy is a temperature dependent term, the pre-factor also plays an important role in determining the overall rate. I can see that the

intercept differs significantly from one reductant to another, increasing in the order of NaAsc, HAsc, HQ, and EtOH. Interestingly, I also visually observed that the reduction involving EtOH and HQ were the fastest reaction because it exhibited the fastest color change upon the introduction of the Pd(II) precursor (the reaction solution changed from light yellow to dark brown within 3 and 5 s!). By equation (2), I can suggest that these reduction reactions involved significant differences in terms of change in activation entropy, with EtOH showing the biggest change. I believe that all terms involved in the Arrhenius equation play an important role in determining the rate of a chemical reaction. These terms can potentially help us elucidate the reaction pathway (surface *vs.* solution), as well as the nanocrystal growth mode. Recently, I discovered that the activation energy to autocatalytic surface reduction was dependent on a number of factors, including the twin boundaries and the type of facet, and ultimately controls the growth pattern and final shape of the products.[44] However, the exact role of the pre-factor in describing the pathway or outcome of a synthesis is yet to be explored.

Based on the dual-reductant concept and the importance of relative reduction powers, I was also interested to see if this strategy could be extended to other strong-weak pairs. To this end, I substituted CA with formic acid (FA), another relatively weak reductant that has been previously used in the seed-mediated growth of Pd octahedra.[34] When FA was paired with one of the strong reductants such as HAsc, I indeed obtained Pd octahedra of 6 nm in edge length, see Figure 3.13A. As shown in Figure 3.13B, I also obtained Pd octahedra of 12 nm in edge length when FA was paired with another strong reductant based on $NaBH_4$.

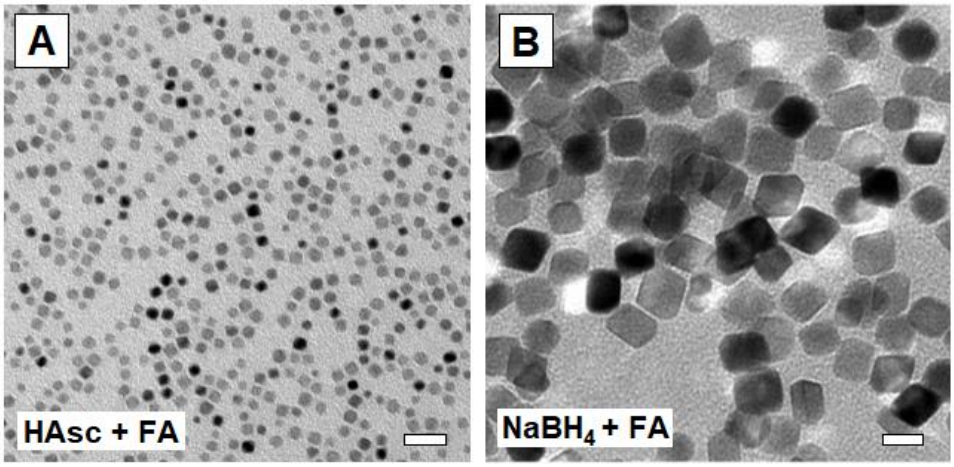

Figure 3.13. TEM images of Pd nanocrystals synthesized through a dual-reductant approach that utilizes formic acid (FA) as a weak reductant: (A) the pair of ascorbic and formic acids (HAsc + FA) that gave Pd octahedra (scale bar: 20 nm), and (B) the pair of sodium borohydride and formic acid ($NaBH_4$ + FA) that also gave Pd octahedra (scale bar: 10 nm).

The data presented above encourages the development of new one-pot approaches to the synthesis of metal nanocrystals with controlled shapes. However, extensive work remains to be done to elucidate the mechanisms of the dual-reductant approach. The reduction mechanism of sole reductants will be altered when several reductants are present simultaneously within the same reaction system. Therefore, in-depth kinetic studies should be conducted in the future to gain a quantitative understanding of the system, and to optimize experimental parameters to reduce the amount of multiple twinned particles. Moreover, given the complexity of the system, the redox reactions between the metal precursor and both reducing agents could exhibit second, third or even higher order kinetics, which invalidates commonly used approximations such as the pseudo-first order approximation. Therefore, additional studies and more complex data analysis methods (*e.g.*, the Finke-Watzky mechanism)[42,55,56] should be developed and/or employed to accurately determine the kinetic and thermodynamic parameters. In some cases, UV/vis

cannot be used alone to track the concentration of a given metal precursor, so inductively-coupled plasma mass spectrometry (ICP-MS) may be necessary to quantify the reduction kinetics.

3.3 Conclusion

In summary, I have validated a strategy for effectively separating the growth of nanocrystals from the nucleation step in a one-pot setting. I intentionally introduced two reductants with very different reducing powers to regulate both the production of seeds, and the necessary growth to produce Pd octahedra. The strong reductant was used to control the initial reduction and nucleation to form single-crystal seeds, while the weak reductant was used for both the slow reduction of unreacted precursor and the stabilization of the resultant {111} facets. To illustrate the generality of this approach, I selected four pairs of strong-weak reducing agents and demonstrated that Pd octahedra could be obtained in good quality for all cases. In contrast, when each of the selected reducing agents was used individually, the products were polydispersed in terms of both size and shape. In all, I expect that this strategy can be expanded to other systems that include metals other than Pd. I hope that this method not only opens the door to new and interesting syntheses, but also enriches the growing understanding regarding the fundamental nucleation and growth processes.

3.4 Experimental Section

Materials and Methods. All chemicals were obtained commercially and were used without further purification. Sodium tetrachloropalladate(II) (Na_2PdCl_4, 99.998%, Acros

Organics), poly(vinyl pyrrolidone) (PVP, MW≈55,000, Sigma-Aldrich), ascorbic acid (HAsc, 99%, Sigma), ethanol (EtOH, 200 proof, Koptec), hydroquinone (HQ, 99%, Sigma-Aldrich), sodium ascorbate (NaAsc, 98%, Sigma-Aldrich), and citric acid (CA, 99.5%, Sigma-Aldrich). All aqueous solutions were prepared using de-ionized (DI) water with a resistivity of 18.2 MΩ cm at room temperature. All the samples were characterized using transmission electron microscopes Hitachi HT7700 operated at 120 kV and Hitachi HD2700 operated at 200kV. The quantitative analysis of reduction kinetics was performed using an ultraviolet-visible spectrophotometer (UV-vis) (Cary 60, Agilent Technology) in the spectral region 200-800 nm. The metal content of the samples was determined using an inductively coupled plasma–mass spectrometer (ICP-MS, NexION 300Q, PerkinElmer).

Syntheses of Pd Octahedra. I used four protocols to synthesize Pd octahedra using four pairs of strong and weak reducing agents. For details regarding concentration of reagents and specific experimental conditions, refer to Table 3.1. In a standard protocol, an aqueous solution containing PVP, a strong reducing agent (HAsc, NaAsc, HQ, or EtOH) and CA was prepared and preheated at a given temperature under magnetic stirring. After 10 min, an aqueous solution of Na_2PdCl_4 was added. The reaction was allowed to proceed for 3 h. The final product was collected by centrifugation and re-disperse in water. Final product was washed three times.

Reduction Kinetics. The reaction kinetics and rate constants for each reducing agent were determined by measuring the concentration of $PdCl_4^{2-}$ ions at different time points in the reaction solution through UV–vis spectroscopy. An 8 mL aqueous solution containing 100 mg PVP and a strong reducing agent (around 30 mM for HAsc, NaAsc, HQ, CA, and 4 M for EtOH) was prepared and mixed using magnetic stirring at a specific temperature (50,

60, or 70 °C) for 10 min. Simultaneously, 2 mL aqueous solution containing 1 mg of Na_2PdCl_4 was prepared and added by one-shot injection to the preheated solution. The timer started running after complete addition of precursor solution. Aliquots of 0.2 mL were taken from the reaction solution at different time points (0.5, 1.0, 2.0, 3.0 min, etc.) and immediately injected into 0.8 mL of aqueous KBr (500 mg/mL) to quench the reduction. Due to the high concentration of bromide ions the $PdCl_4^{2-}$ ions remaining in solution undergo ligand exchange to form the UV-Vis active complex $PdBr_4^{2-}$. The aliquot solutions were centrifuged at 17,500 rpm for 60 min to separate all the Pd nanoparticles formed, and use the supernatant to measure the concentration of $PdBr_4^{2-}$ ions by UV–vis spectroscopy. The measured absorbance of $PdBr_4^{2-}$ at 332 nm and a calibration curve were used to calculate the time-dependent concentration of $PdBr_4^{2-}$ ions.

3.5 Notes to Chapter 3

This chapter was adapted from "Synthesis of Pd Nanoscale Octahedra Through a One-Pot, Dual-Reductant Route and the Kinetic Analysis" published in *Chemistry – European Journal*. [57]

3.6 References

[1] C. Burda, X. Chen, R. Narayanan, M. A. El-Sayed, *Chem. Rev.* 2005, *105*, 1025–1102.

[2] Y. Li, G. A. Somorjai, *Nano Lett.* 2010, *10*, 2289–2295.

[3] X. Wang, L. Figueroa-Cosme, X. Yang, M. Luo, J. Lui, Z. Xie, Y. Xia, *Nano Lett.* 2016, *16*, 1467–1471.

[4] J. Park, L. Zhang, S. I. Choi, L. Roling, N. Lu, J. Herron, S. Xie, J. Wang, M. Kim, M. Mavrikakis, Y. Xia, *ACS Nano* **2015**, *9*, 2635–2647.

[5] D. V. Talapin, J. -S. Lee, M. V. Kovalenko, E. V. Shevchenko, *Chem. Rev.* 2010, *110*, 389–458.

[6] J. N. Anker, W. P. Hall, O. Lyandres, N. C. Shah, J. Zhao, R. P. Van Duyne, *Nat. Mater.* 2008, *7*, 442–453.

[7] M. E. Stewart, C. R. Anderson, L. B. Thompson, J. Maria, S. K. Gray, J. A. Rogers, R. G. Nuzzo, *Chem. Rev.* 2008, 108, 494–521.

[8] N. L. Rosi, C. A. Mirkin, *Chem. Rev.* 2005, *105*, 1547−1562.

[9] X. Yang, M. Yang, B. Pang, M. Vara, Y. Xia, *Chem. Rev.* **2015**, *115*, 10410–10488.

[10] J. Kapar, P. Fornasiero, N. Hickey, *Catal. Today* 2003, 77, 419–449.

[11] M. Zhang, M. Jin, Y. Xia, Chem. Soc. Rev. 2012, 41, 8035–8049.

[12] M. Crespo-Quesada, A. Yarulin, M. Jin, Y. Xia, L. Kiwi-Minsker, *J. Am. Chem. Soc.* 2011, *133*, 12787–12794.

[13] L. Yin, J. Liebscher, *Chem. Rev*. 2007, *107*, 133–173.

[14] M. T. Reetz, E. Westermann, *Angew. Chem. Int. Ed.* 2000, *112*, 170–173.

[15] J. Zhang, Q. Jiang, D. Yang, X. Zhao, Y. Dong, R. Liu, *Chem. Sci.* 2015, *6*, 4674–4680

[16] M. Yamauchi, R. Ikeda, H. Kitagawa, M. Takata, *J. Phys. Chem. C* 2008, *112*, 3294–3299.

[17] M. A. Boles, D. Ling, T. Hyeon, D. V. Talapin, *Nature Mater.* 2016, *15*, 141–153.

[18] Y. Xia, Y. Xiong, B. Lim, S. E. Skrabalak, *Angew. Chem. Int. Ed.* 2009, *48*, 60–103.

[19] W. P. Halperin, *Rev. Mod. Phys.* 1986, *58*, 533–606.

[20] E. Hutter, J. H. Fendler, *Adv. Mater*. 2004, *16*, 1685−1706.

[21] N. L. Okamoto, S. Fujimoto, Y. Kambara, M. Kawamura, Z. M. T. Chen, H. Matsunoshita, K. Tanaka, H. Inui, E. P. George, *Sci. Rep.* 2016, *6*, 1–10.

[22] Y. -W. Jun, Y. -M. Huh, J.-S. Choi, J.-H. Lee, H.-T. Song, S. Kim, S. Yoon, K. -S. Kim, J.-S. Shin, J.-S. Suh, J. Cheon, *J. Am. Chem. Soc.* **2005**, *127*, 5732–5733.

[23] D. Lei, K. Yu, M.-R. Li, Y. Wang, Q. Wang, T. Liu, P. Liu, L-L. Lou, G. Wang, S. Liu. *ACS Catal.* 2017, *7*, 421–432.

[24] Z.-N. Xu, J. Sun, C.-S. Lin, X.-M. Jiang, S.-Y. Peng, M.-S. Wang, G.-C. Guo, *ACS Catal.* 2013, *3*, 118–122.

[25] G. Li, H. Kobayashi, S. Dekura, R. Ikeda, Y. Kubota, K. Kato, M. Takata, T. Yamamoto, S. Matsumura, H. Kitagawa, *J. Am. Chem. Soc.* 2014, *136*, 10222–10225.

[26] M. Jin, H. Liu, H. Zhangm Z. Xie, J. Liu, Y. Xia, *Nano Res.* 2011, *4*, 83–91.

[27] W. Niu, L. Zhang, G. Xu, *ACS Nano* 2010, *4*, 1987–1996.

[28] Y. Zhang, M. Wang, E. Zhu, Y. Zheng, Y. Huang, X. Huang, *Nano Lett.* 2015, *15*, 7519–7525.

[29] Y. Tang, R. E. Edelmann, S. Zou, *Nanoscale* 2014, *6*, 5630–5633.

[30] Y. Sun, L. Zhang, H. Zhou, Y. Zhu, E. Sutter, Y. Ji, M. H. Rafailovich, J. C. Sokolov, *Chem. Mater.* 2007, *19*, 2065–2070.

[31] B. Lim, Y. Xiong, Y. Xia, *Angew. Chem. Int. Ed.* 2007, *119*, 9439–9442.

[32] R. Wang, H. He, L.-C. Liu, H.-X. Dai, Z. Zhao, *Catal. Sci. Technol.* 2012, *2*, 575–580.

[33] Y. Xia, K. Gilroy, H.-C. Peng, X. Xia, *Angew. Chem. Int. Ed.* 2017, *56*, 60−95.

[34] S. Bao, X. Yang, M. Luo, S. Zhou, X. Wang, Z. Xie, Y. Xia, *Chem. Commun.* 2016, *52*, 12594–12597.

[35] M. Jin, H. Zhang, Z. Xie, Y. Xia, *Energy & Environ. Sci.* 2012, *5*, 3652−6357.

[36] W. Niu, L. Zhang, H. Xu, *ACS Nano* 2010, 4, 1987–1996.

[37] S. W. Kang, Y. W. Lee, Y. Park, B.-S. Choi, J. W. Hong, K.-H. Park, S. W. Han, *ACS Nano* 2013, *7*, 7945–7955.

[38] E. G. Wrigglesworth, J. H. Johnston, *RCS Adv.* 2017, *7*, 45757–4562.

[39] H. Zhang, M. Jin, Y. Xiong, B. Lim, Y. Xia, *Acc. Chem. Res.* 2013, *46*, 1783–1794.

[40] S. Xie, S.-I. Choi, N. Lu, L. T. Roling, J. A. Herron, L. Zhang, J. Park, J. Wang, M. J. Kim, Z. Xie, M. Mavrikakis, Y. Xia, *Nano Lett.* 2014, *14*, 3570−3576.

[41] Y. Wang, H.-C. Peng, J. Liu, C. Z. Huang, Y. Xia, *Nano Lett.* 2015, *15*, 1445–1450.

[42] T.-H. Yang, H.-C. Peng, S. Zhou, C.-T. Lee, S. Bao, Y.-H. Lee, J.-M. Wu, Y. Xia, *Nano Lett.* 2017, *17*, 334–340.

[43] T.-H. Yang, K. D. Gilroy, Y. Xia. *Chem. Sci.* 2017, *8*, 6730–6749.

[44] T.-H. Yang, S. Zhou, K. D. Gilroy, L. Figueroa-Cosme, Y.-H. Lee, J.-M. Wu, Y. Xia. *Proc. Natl. Acad. Sci. USA* 2017, *114*, 13619–13624.

[45] L. I. Elding, L. F. Oisson, *J. Phys. Chem.* 1978, *82*, 69–74.

[46] B. Lim, M. Jiang, J. Tao, P. H. C. Camargo, Y. Zhu, Y. Xia, *Adv. Funct. Mater.* 2009, *19*, 189–200.

[47] J. Tue, Z. Du, M. Shao, *Chem. Phys. Lett.* 2016, *659*, 159–163.

[48] Z. Shao, W. Zhu, H. Wang, Q. Yang, S. Yang, X. Liu, G. Wang, *J. Phys. Chem. C.* 2013, *117*, 14289–14294.

[49] A. G. M. da Silva, T. S. Rodrigues, L. S. K. Taguachi, H. V. Fajardo, R. Balzer, L. F. D. Probst, P. H. C. Camargo, *J. Mater. Sci.* 2016, *51*, 603–614.

[50] M. Shao, T. Yu, J. H. Odell, M. Jin, Y. Xia, *Chem. Commun.* 2011, *47*, 6566–6568.

[51] L. I. Elding. *Inorganica Chim. Acta*, **1972**, *6*, 647–651.

[52] C. J. le Roux, R. J. Kriek. *Hydrometallurgy*, **2017**, *169*, 447–455.

[53] J. Zeng, Q. Zhang, J. Chen, Y. Xia. *Nano Lett.* 2010, *10*, 30–35.

[54] R. Narayanan, M. A. El-Sayed, *Nano Lett.* 2004, *4*, 1343–1348; c) T. Bligaard, K. Honkala, A. Logadottir, J. K. Nørskov. *J. Phys. Chem. B.* 2003, *107*, 9325–9331.

[55] M. A. Watzky, R. G. Finke. *J. Am. Chem. Soc.* 1997, *119*, 10382−10400.

[56] M. A. Watzky, E. E. Finney, R. G. Finke. *J. Am. Chem. Soc.* 2008, *130*, 11959−11969.

[57] L. Figueroa-Cosme, K. D. Gilroy, T.-H. Yang, M. Vara, J. Park, S. Bao, A. G. M. da Silva, Y. Xia, *Chem. Eur. J.* **2018**, Accepted, DOI: 10.1002/chem.201705720

CHAPTER 4

SEED-MEDIATED GROWTH OF COLLOIDAL METAL NANOCRYSTALS: SCALING UP THE PRODUCTION THROUGH GEOMETRIC AND STOICHIOMETRIC ANALYSES

4.1. Introduction

Noble-metal nanocrystals have found widespread use in applications ranging from catalysis to photonics, sensing, imaging, and biomedical research.[1-3] In particular, Pd and Pt nanoparticles can serve as excellent catalysts for many industrially important or environmentally relevant reactions. Notable examples include the production of pharmaceutical compounds, the oxidation of fuels as well as reduction of oxygen in proton-exchange membrane fuel cells (PEMFCs), and the oxidation of harmful gases like carbon monoxide produced by the partial combustion of carbon-containing fuels.[4-6] Most of the catalysts currently used in the industry are based on nanoparticles with poorly defined shapes with a broad size distribution. Extensive studies, both experimental and theoretical, have demonstrated that the performance of such catalysts can be greatly enhanced by tuning the size, chemical composition, structure, and shape of the nanoparticles involved.[7-9] The use of catalysts based on nanocrystals with well-controlled shapes and uniform sizes will greatly improve the catalytic performance while significantly reducing the amount of materials needed. This strategy not only lowers the cost of a product but also offers a solution to achieving the highest possible utilization efficiency of the scarcest metals in the Earth's crust.

Seed-mediated growth is an attractive approach to the synthesis of nanocrystals with well-defined shapes and/or structures because it can circumvent the complicated and poorly controlled initial nucleation step.[10-11] This approach is particularly powerful for the synthesis of octahedral and core-shell nanocrystals. As reported in literature, a typical synthesis of Pd octahedra relies on the use of Pd nanocubes as seeds for the heterogeneous nucleation of the newly formed Pd atoms and thus the formation of octahedra (Figure 4.1). Specifically, an aqueous suspension containing Pd nanocubes (seeds), formaldehyde (HCHO, reducing agent), and poly(vinyl pyrrolidone) (PVP, a colloidal stabilizer), is pre-heated in an oil bath, followed by the injection of a solution containing Na_2PdCl_4 (a precursor to Pd atoms). Upon the injection of the salt precursor, the concentration of Pd atoms will quickly increase due to the reduction of $PdCl_4^{2-}$ by HCHO. As illustrated in Figure 4.1 the newly formed Pd atoms will be deposited onto the {100} facets of a cubic seed, forcing it to gradually evolve into an octahedron enclosed by {111} facets.[12,13] A slightly modified approach can be applied to conformally coat the surface of Pd octahedra to generate Pd@$Pt_{3\text{-}4L}$ (L: atomic layers) octahedra with enhanced catalytic activity toward the oxygen reduction reaction (ORR).[14-18]

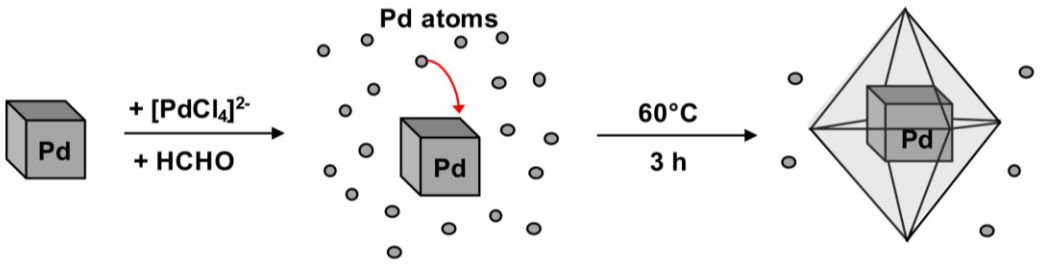

Figure 4.1. Illustration of the seed-mediated growth of a Pd cube into a Pd octahedron. The Pd atoms derived from $PdCl_4^{2-}$ are preferentially deposited on the {100} facets of the Pd cube, which eventually evolves into an octahedron.

Despite the efforts reported in literature, it is still challenging to apply the Pd octahedra and Pd@Pt$_{nL}$ core-shell octahedra to industrial evaluation due to the limited quantity of sample produced. For example, it takes about 6–7 h to produce *ca.* 2 mg of Pd octahedra in each batch of synthesis.[19-20] This amount is barely enough for initial bench testing and characterization, and is insufficient for a pilot study, which is the very first step toward any industrial use. When attempting to scale up the synthesis, I encountered issues such as loss of uniformity and control over both size and shape. This occurs because the formation of nanocrystals is extremely sensitive to experimental conditions, such as the concentrations of reagents, reaction temperature, and reaction volume, among others. When the volumes or concentrations of reagents are scaled up in a synthesis, issues such as the spatial heterogeneity of temperature and chemical composition will be altered, negatively impacting the formation of nanocrystals with uniform and well-defined size, shape, and composition.[21] Alternative methods have been developed to address these issues. For example, continuous flow and droplet reactors have been demonstrated as practical platforms for the scalable synthesis of metal nanocrystals.[19,20] These techniques have enabled the production of shape-controlled nanocrystals typically on a scale of 1–10 g per hour via continuous operation. Nevertheless, the successful operation of these new techniques still requires optimization of the reagents needed for the formation of the nanocrystals.

For the synthesis of Pd octahedra, both the batch and continuous-flow methods rely on the same approach to grow Pd cubic seeds into octahedra through the reduction of a Pd precursor by HCHO. However, these approaches have not been optimized in terms of the ratio between reagents despite their widespread use. The reagents used in significant excess

will lead to unwanted waste and, at the same time, increase the cost of catalyst production. To this end, a detailed understanding of the stoichiometric relationship between the number of cubic seeds and the amount of precursor needed for the formation of octahedra could offer immediate benefits for scaling up the production. Similarly, all reported protocols for conformally coating Pt shells on Pd templates involve the excessive use of reagents, resulting in issues such as the formation of small particles through homogeneous nucleation. In some cases, the formation of such small particles may even compromise the deposition of Pt in terms of thickness control.

In this work, I apply simple geometric and stoichiometric analyses to optimize the experimental conditions for scaling up the seed-mediated synthesis of Pd octahedra and Pd@$Pt_{3–4L}$ octahedra by 250-fold. Through the geometric analysis, I estimate the amount of Pd^{II} precursor required for the complete growth of a Pd cubic seed into a Pd octahedron. The amount of reducing agent is then determined based upon the stoichiometry for the reduction of Pd^{II} to Pd^{0} atoms. Through simple calculations, I can quickly identify the optimal conditions for increasing the volume of production in the synthesis of Pd octahedra to obtain over 500 mg of sample with uniform size and shape, together with purity approaching 100%. The Pd octahedra can then be used as seeds for the synthesis of Pd@$Pt_{3–4L}$ core–shell octahedra. Again, by scaling up the Pt deposition protocol using a similar approach, I could prepare Pd@$Pt_{3–4L}$ core–shell octahedra at a scale of over 200 mg of Pd+Pt. Furthermore, the electrocatalytic measurements indicate that the high ORR activity of the Pd@$Pt_{3–4L}$ octahedra can be well-maintained despite the increased volume of production.

4.2. Results and Discussion

My goal was to obtain nanometer-sized Pd octahedra on a scale of 0.5 gram and above in a single preparation. I accomplished this goal by scaling up the volume of production per batch from *ca.* 2 mg to *ca.* 10 mg by simply increasing the concentrations of reagents while keeping the same total reaction volume. I further increased the volume of production to *ca.* 480 mg by running multiple syntheses under identical conditions in parallel as illustrated in Figure 4.2.

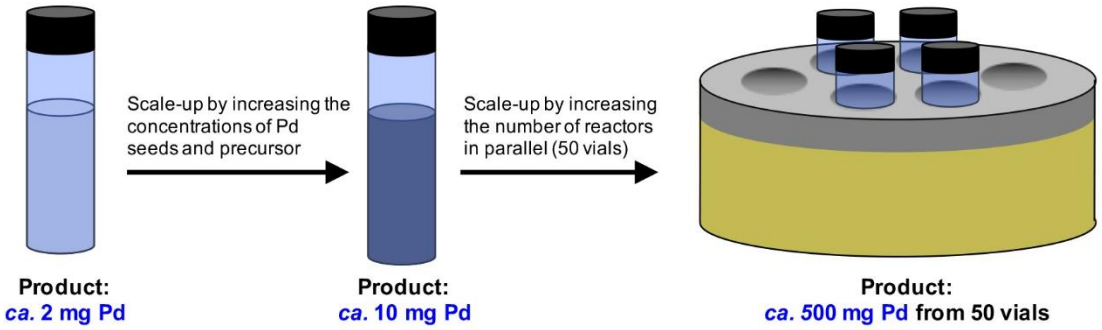

Figure 4.2. Schematic illustration of an approach to scaling-up the synthesis of Pd octahedra. An initial 5x scale-up was achieved by increasing the concentrations of reagents while maintaining the reaction volume constant and another 50x scale-up was accomplished by running 50 identical syntheses in parallel. Through these two steps of scale-up, over 500 mg of Pd octahedra could be obtained with uniform size and shape in a single preparation.

Figure 4.3A shows a typical transmission electron microscopy (TEM) image of the 10nm Pd cubic seeds. When I increased the concentrations of the Pd cubic seeds and all other reagents by 5-fold relative to the previously reported protocol, [10,11] I observed a significant amount of small particles in addition to the Pd octahedra growing from the cubic seeds, as indicated by red circles in Figure 4.3B. Evidently, increasing the concentrations of precursor and reducing agent would lead to acceleration of reduction kinetics and

thereby increase the concentration of the Pd atoms present in solution.[21,24] As a result, homogeneous nucleation would also occur in the reaction solution in addition to the expected heterogeneous nucleation and growth. These particles formed through secondary nucleation are very difficult to remove from the products by centrifugation. It has been reported that the homogeneous nucleation in a seed-mediated synthesis could be minimized by slowing down the reduction kinetics or slowly introducing the reactants.[25,26] However, such an approach would compromise the volume of sample that could be produced within a certain period of time. In this work, I employed geometric and stoichiometric calculations to optimize the amounts of reagents needed for a synthesis and thus eliminate the chance of generating particles through homogeneous nucleation.

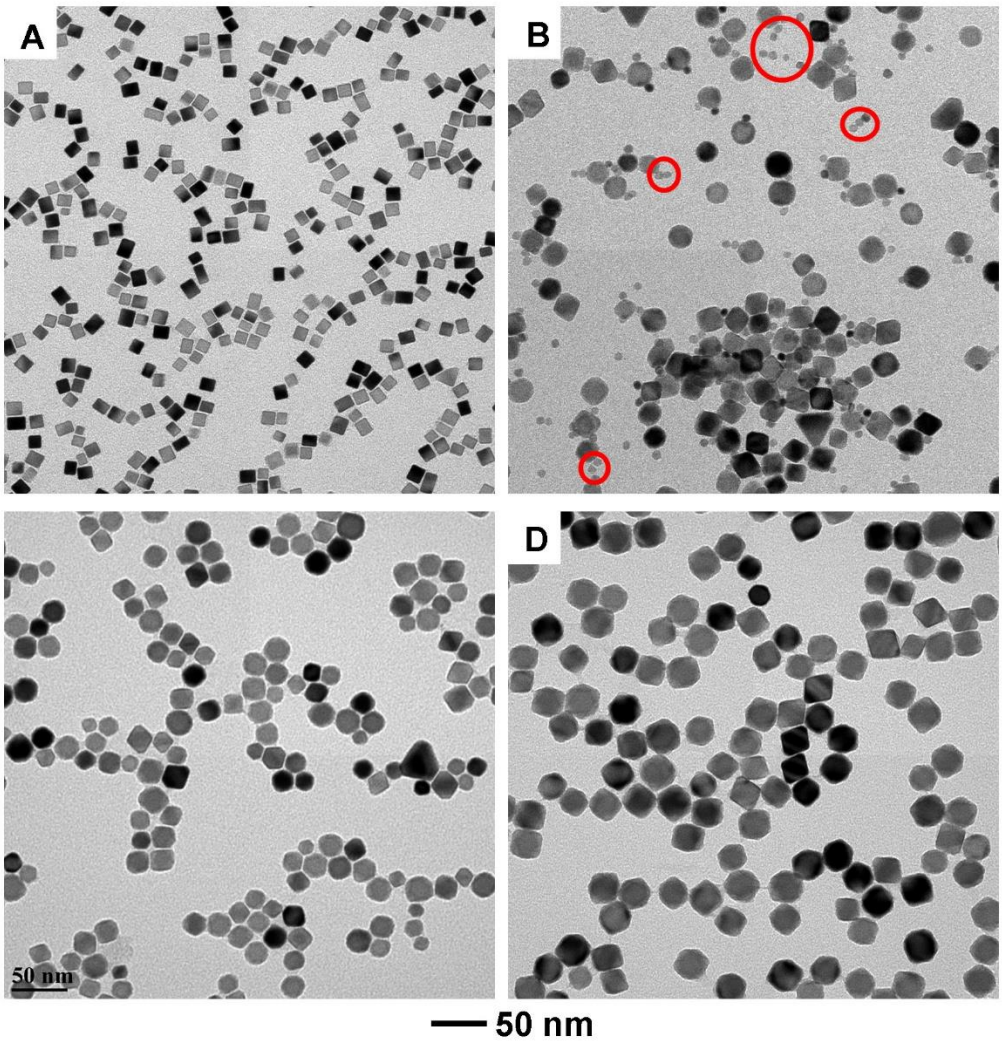

Figure 4.3. TEM images of (A) Pd cubic seeds (10 nm in edge length) and (B-D) Pd nanocrystals obtained through seed-mediated growth from the cubic seeds using different protocols: (B) scale-up protocol by increasing the concentrations of all reagents involved in the standard protocol by 5-fold, (C) scale-up protocol by making adjustments to the concentrations of all reagents involved in the standard protocol, including Pd cubic seeds (5x), Na_2PdCl_4 (5x), HCHO (0.5x), PVP (3x), and (D) the protocol reported in literature.

I first conducted a simple geometric analysis to calculate the exact amount of Pd atoms needed to fully grow a Pd cubic seed into a Pd octahedron by applying the duality principle of platonic polyhedra. According to this mathematical principle, every polyhedron can be described as dual polyhedra, in which their faces and vertices occupy

complementary locations (see an illustration in Figure 4.4).[22] For the objects under study, the center of each face of the octahedron intersects a vertex of the inner cube. I determined the relationship between an initial cubic seed and the final octahedron by using the 2-dimensiomnal projection along the <110> direction of the dual polyhedral system.

In this model, *c* and *o* represent the edge length of the cubic seed and the octahedral product, respectively. Figure 4.4A highlights the face of the octahedron that will be dissected by the [110] plane used to construct the 2D projection. This face is an equilateral triangle with height *b* described by equation (1). In the same way, Figure 4.4B highlights the cross-section of the cube that is dissected by the [110] plane. This projection is represented by a rectangle with edge lengths *c* and *a*, as described by equation (2). Figure 4.4C was constructed based on the drawings in (A) and (B). Using similar triangles and algebraic manipulation, I calculated the ratio between *a* and *b*, which can be expressed in terms of *c* and *o*, as described by equations (3) and (4). This relationship was used to calculate the volume ratio, equations (5-7) between the octahedron (Vo) and cube (Vc). Since the cube and octahedra are both made of Pd, the volume ratio equals the mass ratio. Finally, with the obtained mass ratio, I calculated the mass of Pd (m_{add}) needed to grow a perfect octahedron from a cube.

$$o^2 = \left(\frac{o}{2}\right)^2 + b^2 \rightarrow b = \frac{\sqrt{3}}{2}o \quad (1)$$

$$a^2 = c^2 + c^2 \rightarrow a = \sqrt{2}c \quad (2)$$

$$\frac{b}{a} = \frac{\sqrt{3}}{2\sqrt{2}}\left(\frac{o}{c}\right) \quad (3)$$

$$\frac{o}{c} = \frac{3\sqrt{2}}{2} \quad (4)^*$$

$$V_c = c^3 \quad (5)$$

$$V_o = \frac{\sqrt{2}}{3} o^3 \quad (6)$$

$$\frac{V_o}{V_c} = \frac{m_o}{m_c} = \left(\frac{\sqrt{2}}{3}\right)\left(\frac{o}{c}\right)^3 = 4.5 \quad (7)$$

$$m_{add} = m_o - m_c = 3.5 m_c \quad (8)$$

Since the Pd cubes and the final octahedra are made of the same metal, the calculated volume ratio (V_o/V_c) equals the mass ratio (m_o/m_c) of the dual polyhedral system. The obtained value was 4.5. It is important to clarify that these calculations only apply to the seed-mediated growth of Pd octahedra under the assumption that all the newly formed atoms were added onto the {100} facets with no growth along the <111> direction.

Using ICP-MS, I obtained the total mass of Pd metal in the suspension of cubic seeds, and based upon the calculated m_o/m_c, we estimated the minimum amount of precursor needed for the formation of complete octahedra from the cubic seeds. The minimum amount of reducing agent was then derived from stoichiometry for the reduction of Pd^{II} precursor to Pd^0 atoms by considering the donation of two electrons per HCHO molecule.[28,29] Through this simple analysis, I could achieve a 5-fold increase in the output of a single batch by increasing the Pd^{II} precursor by 5 times and halving the amount of HCHO. Under this new set of conditions, I could obtain *ca.* 10 mg of Pd octahedra with an average edge length of 21 nm (Figure 4.3C) without homogeneous nucleation. It is important to note that homogeneous nucleation was avoided by minimizing the amount of Pd atoms formed during the growth process due to the lower amount of reducing agent used. The size and quality of the Pd octahedra obtained using this scale-up protocol was comparable to the product prepared using the original protocol at a scale of *ca.* 2 mg per batch (Figure 4.3D).[10,11]

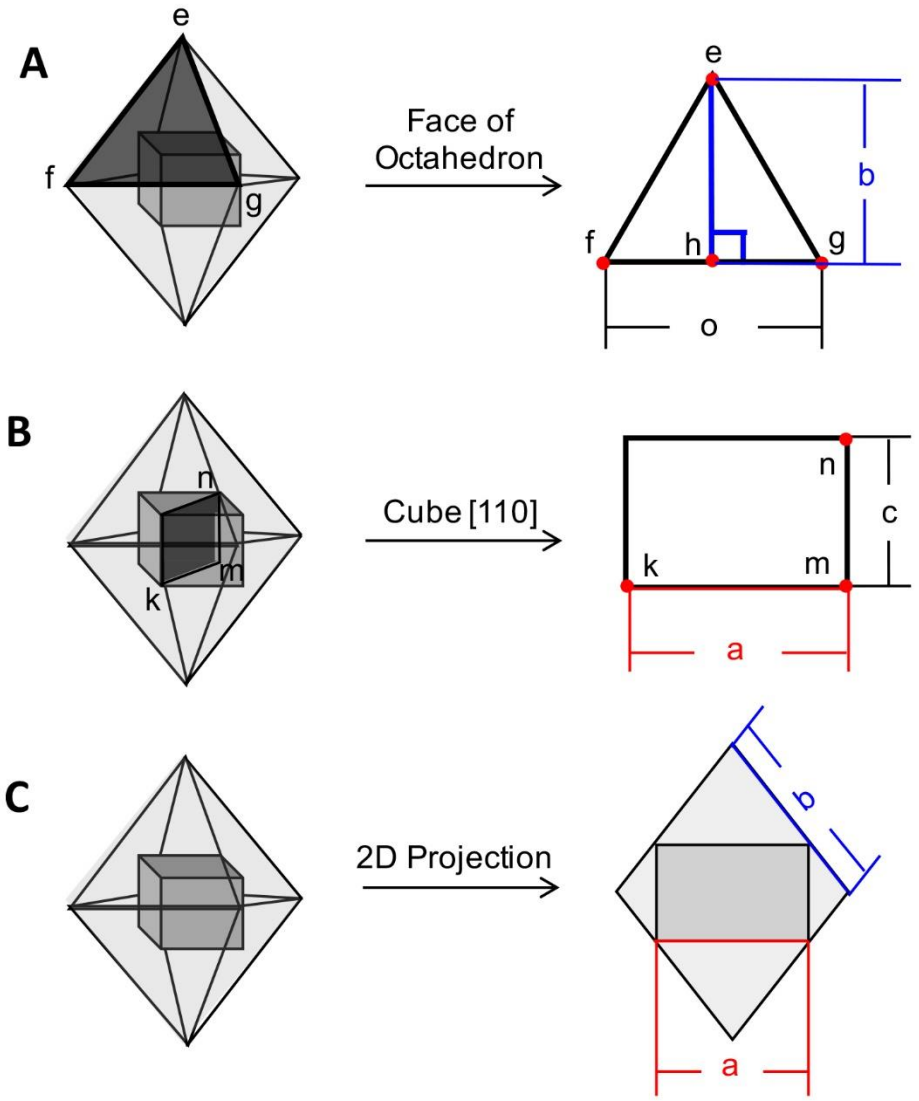

Figure 4.4. Model showing the 2D planes obtained when evaluating the dual polyhedral system along the <110> direction: (A) the octahedron face is represented by an equilateral triangle, (B) the cross-section of the cube is represented by a rectangle, and (C) the overall 2D projection of the system.

I further extended the scaled-up synthesis to multiple batches conducted in parallel. In a typical setup, a thermocouple was immersed in an oil bath hosted in a crystal dish, which was placed on a temperature-controlled stirring hotplate (Figure 4.5). A custom-made vial holder was designed to rest on top of the crystal dish to hold up to 11 glass vials (see Figure 4.6, A and D, for top-view illustrations of the vial holder). I used five oil baths

held at 60°C, and conducted ten parallel syntheses in each oil bath to scale-up the volume of production by another 50-fold from *ca.* 10 mg to *ca.* 500 mg. To evaluate the quality and reproducibility of the syntheses, I analyzed samples obtained at random locations in the oil baths. As shown in Figure 4.6, the samples obtained from two different locations in the same oil bath (marked with blue and red colors) were almost identical to each other and both were comparable to the samples prepared in different oil baths. This combined scale-up approach allowed us to obtain at least 0.5 g of Pd octahedra of 21 nm in edge length within 3 h, which were further employed for the synthesis of Pd@Pt$_{nL}$ octahedra.

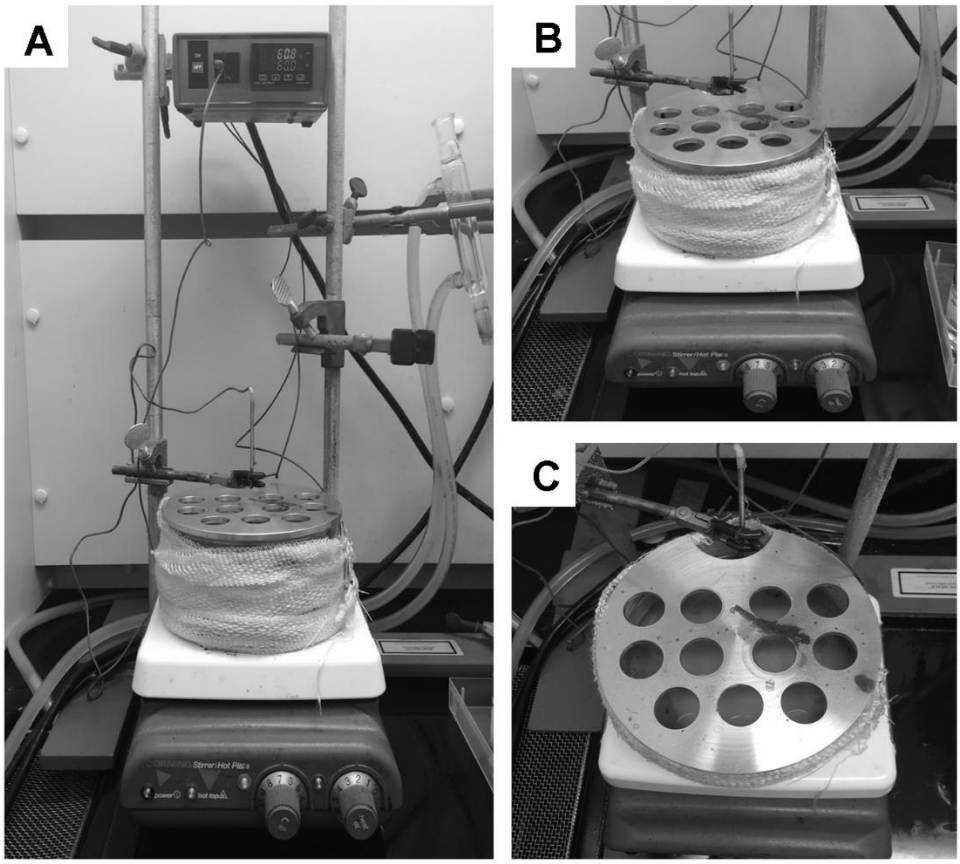

Figure 4.5. Photographs of the experimental setup used for scaling up the synthesis of both Pd octahedra and Pd@Pt$_{3\text{-}4L}$ octahedra. (A) The setup contains a thermo-couple immersed in the oil bath and a temperature-controlled stirring hotplate. (B) Close-up of the oil-containing crystal dish and stirring hotplate (C) Top-view of a custom-made vial holder designed to rest on top of the crystal dish. It can hold up to 11 glass vials.

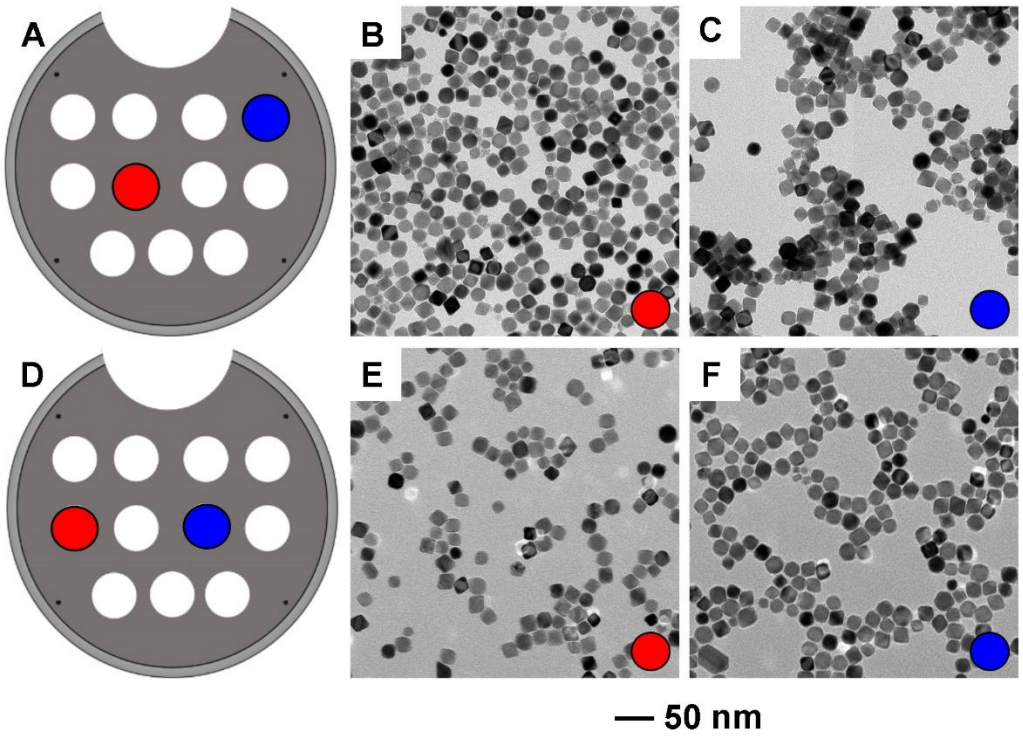

Figure 4.6. TEM images of the Pd octahedra synthesized in the vials placed at different locations of (B and C) Oil Bath 1 and (E and F) Oil Bath 2 under the same experimental conditions. The locations are marked in (A) and (D) with different colors, respectively.

I have also applied the aforementioned geometric and stoichiometric analyses to seed-mediated syntheses of Pd octahedra with different sizes. To my knowledge, no effective method has been reported in literature for the preparation of Pd octahedra with different sizes regardless of the volume of production. The seed-mediated growth has been an effective method for the synthesis of Pd octahedra with uniform shapes and well-controlled sizes. In this case, one can control the size of the final Pd octahedra by simply varying the size of the Pd cubic seeds involved. The overgrowth will be self-terminated once the dual polyhedron has been formed.[10,11] Since the calculated m_o/m_c is independent of the size of the cubic seed, the same set of calculations can be applied to synthesize Pd octahedra with different sizes. The Pd cubic seeds were all prepared by

following a protocol previously reported by our group, in which the size of the cubes could be controlled by varying the amounts of KBr and KCl involved in the synthesis,[23] as summarized in Table 4.1. Figure 4.7, A and B, shows TEM images of Pd cubic seeds with average edge lengths of 6 nm and 15 nm, respectively. Using these seeds, I performed 5-fold scale-up syntheses of Pd octahedra with average edge lengths of 15 nm (Figure 4.7C) and 31 nm (Figure 4.7D), respectively.

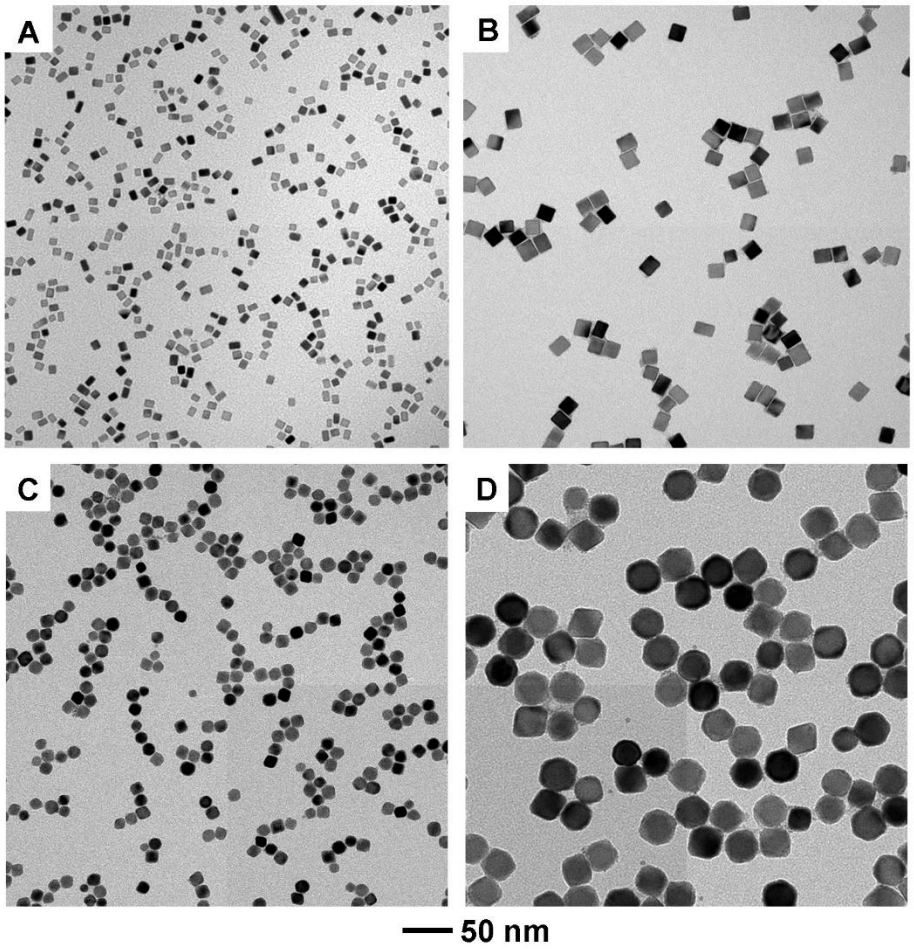

Figure 4.7. TEM images of (A and B) Pd cubes and (C and D) Pd octahedra with different edge lengths of (A) 6 nm, (B) 15 nm, (C) 15 nm, and (D) 31 nm, respectively. The Pd octahedra in (C) and (D) were obtained through growth from the Pd cubic seeds in (A) and (B), respectively.

Table 4.1. List of reagents used in the syntheses of Pd nanocrystals.

Pd nanocrystals (ave. edge length)	Reagents		
Pd cubes (6 nm)	PVP KBr KCl AA	105 mg 5 mg 185 mg 60 mg	57 mg Na_2PdCl_4
Pd cubes (10 nm)	PVP KBr KCl AA	105 mg 300 mg --- mg 60 mg	57 mg Na_2PdCl_4
Pd cubes (15 nm)	PVP KBr AA	105 mg 400 mg 60 mg	57 mg Na_2PdCl_4
Pd octahedra (21 nm) low-scale	PVP HCHO Pd cubes (10 nm)	105 mg 100 μL 0.3 mL (1.81 mg mL^{-1})	29 mg Na_2PdCl_4
Pd octahedra (15 nm)	PVP HCHO Pd cubes (6 nm)	315 mg 50 μL 0.75 mL (3.64 mg mL^{-1})	145 mg Na_2PdCl_4
Pd octahedra (21 nm)	PVP HCHO Pd cubes (10 nm)	315 mg 50 μL 0.75 mL (3.64 mg mL^{-1})	145 mg Na_2PdCl_4
Pd octahedra (31 nm)	PVP HCHO Pd cubes (15 nm)	315 mg 50 μL 0.75 mL (3.64 mg mL^{-1})	145 mg Na_2PdCl_4

A similar stoichiometric approach was further extended to the synthesis of Pd@Pt_{nL} octahedra in an aqueous system. Although I have developed a protocol for the synthesis of Pd@Pt_{nL} octahedra through epitaxial, conformal deposition of Pt shells on Pd octahedra in an aqueous solution, the volume of production has been limited to *ca.* 2 mg per batch based on the mass of Pd.[7-9] Here I scaled up the synthesis by increasing the concentration of Pd octahedral seeds by 10-fold. In order to avoid self-nucleation of the newly formed Pt atoms, I increased the concentration of K_2PtCl_4 (Pt precursor) by only 3-fold while keeping the concentration of citric acid (CA, reducing agent) the same as in the previously reported protocol.[16] Figure 4.8A shows a TEM image of Pd octahedral seeds with an average edge length of 21 nm and Figure 4.8B shows a TEM image of the Pd@$Pt_{3–4L}$ octahedra obtained through conformal deposition of Pt shells at a scale of *ca.* 21 mg of Pd per batch. As shown by the image, I could successfully avoid the generation of Pt nanoparticles through homogeneous nucleation even though the concentration of Pt precursor was increased by 3-fold. This success can be attributed to the slow reduction kinetics of the Pt precursor due to the use of a mild reducing agent like CA.

I evaluated the electrocatalytic performance of the Pd@$Pt_{3–4L}$ octahedra toward ORR using the rotating disk electrode method. Before electrocatalytic measurements, I dispersed the Pd@$Pt_{3–4L}$ octahedra of 21 nm in edge length on carbon black (Ketjenblack EC-300J, AkzoNobel) to obtain Pd@$Pt_{3–4L}$ /C catalyst (Figure 4.8C). In order to remove potential residues such as PVP from the surface of the nanocrystals, I treated the Pd@$Pt_{3–4L}$/C catalyst by incubating in acetic acid at 60 °C for 2 h. To benchmark the electrocatalytic properties of Pd@$Pt_{3–4L}$/C, I also carried out similar measurements with a commercial Pt/C catalyst (20 wt% Pt, 3.2 nm particles on Vulcan XC-72, Premetek).

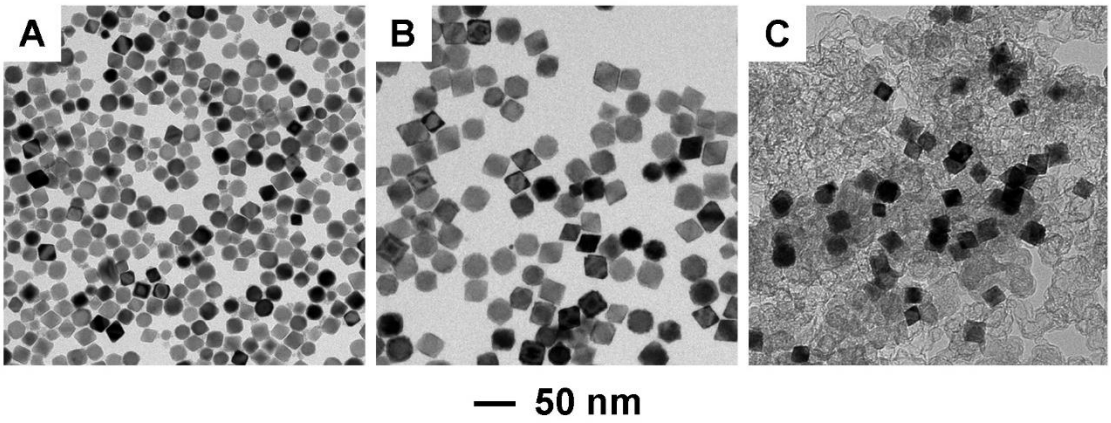

Figure 4.8. TEM images of (A) Pd octahedra, (B) Pd@$Pt_{3–4L}$ octahedra, and (C) Pd@$Pt_{3–4L}$/C catalyst. For the synthesis of Pd@$Pt_{3–4L}$ octahedra, Pd octahedra with an edge length of 21 nm were used as the seeds for Pt deposition.

I obtained the cyclic voltammograms (CVs, Figure 4.9A) and ORR polarization curves (Figure 4.9B) of the catalysts by sweeping the potentials between 0.08 and 1.1 V_{RHE} in N_2-saturated and O_2-saturated $HClO_4$ solutions, respectively. Based on the CVs, I calculated the electrochemical surface areas (ECSA) of the catalysts from the total charges associated with both adsorption and desorption of underpotentially deposited hydrogen on a Pt surface. As presented in Figure 4.9C, the specific ECSA of the Pd@$Pt_{3–4L}$ (61 m^2 g_{Pt}^{-1}) was comparable to that of the commercial Pt/C (56 m^2 g_{Pt}^{-1}) in spite of the significant difference in particle size (21 nm vs. 3.2 nm). This result indicates that the Pt atoms were well-dispersed on the surface of Pd octahedra as ultrathin shells. From the ORR polarization curve, I derived the kinetic current (i_k)of the catalyst using the Koutecky-Levich equation and then normalized it against the ECSA and Pt mass to obtain the specific ($j_{k,specific}$) and mass activities ($j_{k,mass}$), respectively. For a quantitative comparison of the catalytic activities between the Pd@$Pt_{3–4L}$/C and commercial Pt/C catalysts, I selected $j_{k,specific}$ and $j_{k,mass}$ at 0.9 V_{RHE} and plotted them in Figure 4.9, D and E, respectively. The

results are summarized in Table 4.2. The Pd@$Pt_{3–4L}$/C exhibited a 3-fold enhancement in both the specific and mass activities relative to the commercial Pt/C catalyst. The enhancement in specific activity of the Pd@$Pt_{3–4L}$/C could be attributed not only to its well-defined Pt{111} facets, but also to ligand and lattice strain effects arising from the Pd sub-surfaces. I have provided an in-depth discussion with regard to the enhanced ORR activity with the Pd@$Pt_{n\mathrm{L}}$ octahedra catalysts in a recent publication.[16] Although the Pd@$Pt_{3–4L}$/C catalyst showed a mass activity comparable to Pt/C in terms of platinum group metals (Pt+Pd, Table 4.2), the former should be much less expensive due to the lower market price of Pd relative to Pt ($660 vs. $1049 per troy oz.). As an additional alternative to further minimize material use and cost, recent work performed by our group also demonstrated that the Pd cores could be selectively removed to obtain Pt-based nanocages with a mass activity of more than three times higher than the commercial Pt catalyst.[14-18]

Table 4.2. Specific ECSA, specific activity, and mass activity for the Pt/C and Pd@$Pt_{3–4L}$/C catalysts used in the ORR measurements. The mass activity is presented with respect to both platinum and platinum group metal (PGM, Pt+Pd).

Catalysts	Specific ECSA ($m^2\ g_{Pt}^{-1}$)	Specific Activity ($mA\ cm^{-2}_{Pt}$)	Mass Activity ($A\ mg_{Pt}^{-1}$)	Specific ECSA ($A\ mg_{PGM}^{-1}$)
Commercial Pt/C	56	0.54	0.3	0.3
Pd@$Pt_{3–4L}$/C	61	1.64	1.0	0.3

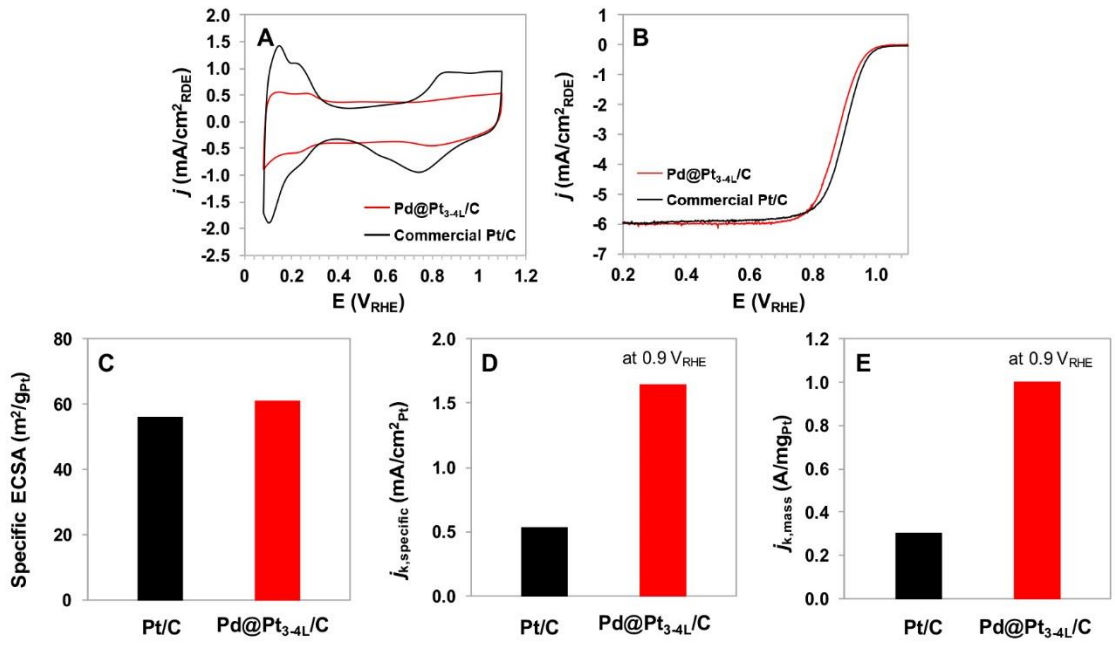

Figure 4.9. (A) Cyclic voltammograms and (B) ORR polarization curves for the Pd@$Pt_{3–4L}$/C (red) and commercial Pt/C (black) catalysts. The current densities (*j*) were normalized against the geometric area of the RDE (0.196 cm^2). (C) Specific ECSAs obtained with the total charges generated from both the adsorption and desorption of underpotentially deposited hydrogen. (D) Specific and (E) mass activities (normalized against the masses of Pt) at 0.9 V_{RHE} for the catalysts.

4.3 Conclusion of Chapter 4

In summary, I have successfully developed a method to increase the production of Pd octahedra from *ca.* 2 mg to over 500 mg. The work presented here also offers a new perspective for increasing the production of other types of noble-metal nanocrystals. By taking advantage of stoichiometry, I have demonstrated the capability to increase the volume of production of Pd octahedra with different sizes via seed-mediated growth. A geometric and stoichiometric analysis was performed to calculate the minimum amount of reagents needed for the complete growth of a Pd cubic seed into its dual polyhedron. I could avoid homogeneous nucleation by minimizing the amount of Pd atoms formed

during growth process while retaining good control over the shape of the nanocrystals. The approach was also successfully extended to the synthesis of Pd@$Pt_{3–4L}$ octahedra, which were subsequently tested as catalysts toward oxygen reduction. The Pd@$Pt_{3–4L}$ octahedra prepared using a 10-fold scaled-up synthesis demonstrated a 3-fold increase in both the specific and mass activity toward ORR relative to the commercial Pt/C catalyst. The ability to achieve higher throughput in the synthesis of noble-metal nanocrystals will provide an opportunity to fully evaluate their potential use for industrial applications.

4.4 Experimental Section

Materials. All the chemicals were used as received, including sodium tetrachloropalladate(II) (Na_2PdCl_4, 99.998%, Acros Organics), potassium tetrachloroplatinate(II) (K_2PtCl_4, 99.99%, Sigma-Aldrich), poly(vinyl pyrrolidone) (PVP, MW≈55^000, Sigma-Aldrich), formaldehyde (HCHO, 36.5-38%, Sigma-Aldrich), ascorbic acid (AA, 99%, Sigma-Aldrich), and citric acid (CA, 99.5%, Sigma-Aldrich). All aqueous solutions were prepared using de-ionized (DI) water with a resistivity of 18.2 MΩ cm.

Synthesis of Pd Cubic Seeds. The Pd cubic seeds with different edge lengths were synthesized by following a standard protocol according to Table 2.1. An aqueous solution (8 mL) containing PVP, AA, and a combination of KBr and KCl was preheated at 80 °C for 10 min under magnetic stirring. Meanwhile, 3 mL of an aqueous solution containing Na_2PdCl_4 (57 mg) was prepared and rapidly injected into the preheated solution using a pipet. The reaction solution was kept at 80 °C for 3 h, and the resultant nanocrystals were

collected by centrifugation, washed three times with DI water, and re-dispersed in water for further use.

Scaled-up Synthesis of Pd Octahedra. In a typical procedure, 8 mL of an aqueous suspension containing PVP, HCHO, and Pd cubic seeds was prepared according to Table 4.1 and then pre-heated at 60 °C for 10 min under magnetic stirring. Meanwhile, 3 mL of an aqueous Na_2PdCl_4 (145 mg) solution was rapidly added into the preheated solution using a pipet. The reaction was allowed to proceed at 60 °C for 3 h. The resultant nanocrystals were washed twice with water and re-dispersed in water for further use.

Scaled-up Synthesis of Pd@$Pd_{3–4L}$ Octahedra. For the scaled-up synthesis of Pd@$Pt_{3–4L}$ octahedra, PVP (105 mg) and CA (60 mg) were added into 10 mL of an aqueous suspension of Pd octahedra (20 nm in edge length, 2 mg mL^{-1}) and then preheated at 95 °C for 10 min under magnetic stirring. Meanwhile, 40 mg of K_2PtCl_4 was dissolved in 3 mL of water and was then quickly added into the preheated Pd octahedra solution using a pipet. The reaction solution was kept at 95 °C for 24 h under magnetic stirring and then cooled to room temperature. The products were collected by centrifugation, washed three times with DI water, and re-dispersed in water for further use.

Preparation of Carbon-Supported Pd@$Pd_{3–4L}$ Octahedra Catalyst (Pd@$Pd_{3–4L}$/C). The Pd@$Pt_{3–4L}$ octahedra were collected by centrifugation and redispersed in ethanol. A specific amount of carbon black (Ketjenblack EC-300 J, AkzoNobel) was added into the suspension to obtain a 20 wt% of total metal loading (Pd and Pt). The mixture was then ultrasonicated for 3 h, and the resultant Pd@$Pt_{3–4L}$/C was collected by centrifugation, re-dispersed in acetic acid, and heated at 60 °C for 3 h to remove PVP from the surface of the

nanocrystals. The Pd@Pt_{3-4L}/C catalyst was washed three times with ethanol and dried in an oven at 70 °C for 30 min prior ORR tests.

Morphological, Structural, and Elemental Characterization. All the samples were characterized using a transmission electron microscope (TEM, JEOL-JEM1400) operated at 120 kV. The metal contents of each sample were determined using an inductively coupled plasma-mass spectrometer (ICP-MS, NexION 300Q, PerkinElmer).

Electrochemical Measurements. Electrochemical measurements were performed following previously reported protocol, [14-18] which uses a glassy carbon rotating disk electrode (RDE, Pine Research Instrumentation) connected to a potentiostat (CHI 600E, CH Instruments). The ink for the electrochemical measurement was prepared by adding the Pd@Pt_{3-4L}/C suspension into a solution containing DI water (1 mL), 2-propanol (1 mL, Sigma-Aldrich), and Nafion (5 % solution, Sigma--Aldrich, 40 μL), followed by sonication for 10 min. A working electrode was prepared by loading the ink (20 μL) on the glassy carbon electrode. Another working electrode was prepared from the commercial Pt/C catalyst (20 wt% Pt, 3.2 nm nanoparticles on Vulcan XC-72 carbon support, Premetek) using the same protocol. A reversible hydrogen electrode (RHE, Gaskastel) and a Pt coil (Pine Research Instrumentation) were used as the reference and counter electrodes, respectively. The electrolyte was an aqueous $HClO_4$ solution (70 %, double-distilled, GFS chemicals) with a concentration of 0.1 M. Any residual impurities on surfaces of the catalysts were removed using a nondestructive method at room temperature by keeping the electrode potential at -0.05 V_{RHE} for 1 min. The cyclic voltammograms were measured in a N_2-saturated electrolyte by cycling between 0.08 and 1.1 V_{RHE} at a sweep rate of 0.05 $V^{\wedge}s^{-1}$. To calculate the ECSA, I measured the charges generated from the both adsorption

and desorption peaks of hydrogen between 0.08 and 0.4 V_{RHE} with a reference value of 210 (Pt/C) and 240 μC^cm^{-2} (Pd@Pt_{3-4L}/C) for underpotentially deposited hydrogen on a Pt surface and then divided by the mass of Pt loaded on the working electrode. The ORR test was carried out in an O_2-saturated electrolyte with a scan rate of 0.01 V^s^{-1} and a rotation speed of 1600 rpm. The kinetic current density (j_k) was derived from the Koutecky--Levich equation as follows:

$$\frac{1}{j} = \frac{1}{j_k} + \frac{1}{j_d}$$

where j is the measured current density and j_d is the diffusion-limiting current density.

4.5 Notes to Chapter 4

This chapter was adapted from "Seed-Mediated Growth of Colloidal Metal Nanocrystals: Scaling Up the Production Through Geometric and Stoichiometric Analyses" published in *ChemNanoMat*. [30]

4.6 References

[1] R. Jin, Y. W. Cao, C. Mirkin, K. Kelly, G. Schatz, J. Zheng, *Science* **2001**, *294*, 1901–1903.

[2] J. Anker, W. Paige Hall, O. Lyandres, N. C. Shah, J. Zhao, R. P. Van Duyne, *Nature Materials* **2008**, *7*, 442–453.

[3] X. Lui, D. Wang, Y. Li, *Nano Today* **2012**, *7*, 448–466.

[4] *Y. Li, E. Boone, M. A. El-Sayed, Langmuir* **2002**, 18, 4921–4925.

[5] S. I. Choi, J. Herron, J. Scaranto, H. Huang, Y. Wang, X. Xia, T. Lv, J. Park, H. C.

Peng, M. Mavrikakis, Y. Xia, *ChemCatChem* **2015**, *7*, 2077–2084.

[6] E. Antolini, *Energy Environ. Sci.* **2009**, *2*, 915–931.

[7] T. Ahmadi, Z. Wang, T. Green, A. Henglein, M. A. El-Sayed, *Science* **1996**, *272*, 1924–1926.

[8] R. Narayanan, M. A. El-Sayed, *Nano Lett.* **2004**, *4*, 1343–1348.

[9] M. Shao, T. Yu, J. Odell, M. Jin, Y. Xia, *Chem. Commun.* **2011**, *47*, 6566–6568.

[10] M. Jin, H. Zhang, Z. Xie, Y. Xia, *Energy Environ. Sci.* **2012**, *5*, 6352–6357.

[11] H. Zhang, M. Jin, Y. Xiong, B. Lim, Y. Xia, *Acc. Chem. Res.* **2012**, *46*, 1783–1794.

[12] Y. Xia, Y. Xiong, B. Lim, S. Skrabalak, *Angew. Chem. Int. Ed.* **2009**, *48*, 60–103.

[13] H. Zang, M. Jin, Y. Xia, *Angew. Chem. Int. Ed.* **2012**, *51*, 7656–7673.

[14] X. Wang, L. Figueroa-Cosme, X. Yang, M. Luo, J. Lui, Z. Xie, Y. Xia, *Nano Lett.* **2016**, *16*, 1467–1471.

[15] L. Zhang, L. Roling, X. Wang, M. Vara, M. Chi, J. Liu, S. I. Choi, J. Park, J. Herron, Z. Xie, M. Mavrikakis, Y. Xia, *Science* **2015**, *349*, 412–416.

[16] J. Park, L. Zhang, S. I. Choi, L. Roling, N. Lu, J. Herron, S. Xie, J. Wang, M. Kim, M. Mavrikakis, Y. Xia, *ACS Nano* **2015**, *9*, 2635–2647.

[17] S. Xie, S. I. Choi, L. Ning, L. Roling, J. Herron, L. Zhan, J. Park, J. Wang, M. Kim, Z. Xie, M. Mavrikakis, Y. Xia, *Nano Lett*. **2014**, *14*, 3570–3576.

[18] X. Wang, S. I. Choi, L. T. Roling, M. Luo, C. Ma, L. Zhang, M. Chi, J. Liu, Z. Xie, J. Herron, M. Mavrikakis, Y. Xia, *Nature Communications* **2015**, *6*, 7594.

[19] L. Zhang, Y. Xia, Adv. Mater. 2014, 26, 2600–2606.

[20] L. Zhang, G. Nui, N. Lu, J. Wang, L. Tong, L. Wang, M. Kim, Y. Xia, *Nano Lett.* **2014**, *14*, 6626–6631.

[21] Y. Xia, X. Xia, H. C. Peng, *J. Am. Chem. Soc.* **2015**, *137*, 7947–7966.

[22] H. Steinhaus, *Mathematical Snapshots*, Oxford Oxfordshire, New York: Oxford University Press, **1983**, 194.

[23] M. Jin, H. Liu, H. Zhang, Z. Xie, J. Liu, Y. Xia, *Nano Res.* **2011**, *4*, 83–91.

[24] M. Luty-Błocho, K. Pacławski, M. Wojnicki, K. Fitzner, *Inorganica Chimica Acta* **2013**, *395*, 189–196.

[25] W. Niu, Z. Y. Li, L. Shi, X. Liu, H. Li, S. Han, J. Chen, G. Xu, *Cryst. Growth Des.* **2008**, *8*, 4440–4444.

[26] W. Niu, L. Zhang, *ACS Nano* **2010**, *4*, 1987–1996.

[27] S. Guo, S. Zhang, S. Sun, *Angew. Chem. Int. Ed.* **2013**, *52*, 8526–8544.

[28] J. J. Byerley, W. K. Teo, Canadian Journal of Chemistry **1969**, *47*, 3355–3360.

[29] L. Nie, Y. Zheng, J. Yu, *Dalton Trans.* **2014**, *43*, 12935–12942.

[30] L. Figueroa-Cosme, J. Park, S. Bao, Y. Xia, *ChemNanoMat.* **2016**, *2*, 1033–1039.

CHAPTER 5

FACILE SYNTHESIS OF IRIDIUM NANOCRYSTALS WITH WELL-CONTROLLED FACETS USING SEED-MEDIATED GROWTH

5.1. Introduction

Nanocrystals of the Pt-group metals with a face-centered cubic structure (*i.e.* Pt, Pd, Rh, and Ir) have received particular interest in recent years because of their outstanding performance in a vast variety of industrially important catalytic reactions.[1-8] It is well-documented that the activity and selectivity of such nanocrystals for a structure-sensitive reaction are highly dependent on the arrangement of atoms and thus the type of crystallographic planes on the surface, which has a strong correlation with the shape.[9-12] In the oxygen reduction reaction, for example, the catalytic activity of 6 nm Pd cubes enclosed by {100} facets with a square lattice was found to be 1 order of magnitude higher than that of 6 nm Pd octahedra encased by {111} facets with a hexagonal lattice.[13] In another example, the hydrogenation of benzene catalyzed by 13 nm Pt cubes encased by {100} facets generated only cyclohexene, whereas both cyclohexane and cyclohexene were observed for 13 nm Pt cuboctahedra covered by a mixture of {111} and {100} facets.[14]

It is well-known that the Pt-group metals are very expensive because of the ever-increasing demand and their extremely low contents in the Earth's crust (typically at a ppb level).[15] In order to reduce the loading amount of these precious metals and thus achieve sustainable use, we need to maximize the performance of their nanocrystals by carefully controlling the shape. To this end, a variety of different shapes have been reported for Pt,

Pd, and Rh nanocrystals over the past few decades.[16-19] However, to the best of our knowledge, there is no literature report on Ir nanocrystals with well-defined shapes. Most of the reported Ir nanocrystals are irregular particles with sizes of 1−5 nm and roughly spherical shapes.[20-23] The difficulty in generating Ir nanocrystals with well- controlled facets can be attributed to their small sizes. Because of truncations at the corners and edges, the facets on the side faces are too small to be resolved. The small sizes of Ir nanoparticles can be ascribed to the relatively low energy barrier for homogeneous nucleation compared with that for heterogeneous nucleation during synthesis, as a result of which the newly formed Ir atoms in a synthesis tend to self-nucleate and grow into small particles rather than nucleate on the surface of preformed particles to form larger particles.

Herein we demonstrate that nanocrystals exposing well- defined Ir facets can be synthesized using seed-mediated growth, by which Ir atoms resulting from the reduction of Na_3IrCl_6 by ascorbic acid (AA) and ethylene glycol (EG) were added onto the surface of Pd seeds with well-defined shapes. The key to the success of such a synthesis is to conduct the growth at a high enough temperature (e.g., 200 °C), at which the surface diffusion of the Ir adatoms is greatly accelerated. The fast diffusion of Ir adatoms across the Pd surface ensures a layer-by-layer (LbL) growth mode and thus the formation of a conformal coating of Ir. As long as the Ir shell is smooth at the atomic level, the facets on the resultant Pd@Ir core−shell nanocrystals will replicate those on the initial Pd seeds. Therefore, nanocrystals covered by different Ir facets can be readily obtained simply by using Pd nanocrystals with different shapes as the seeds. Specifically, we have successfully synthesized Pd@Ir cubes and octahedra covered by Ir{100} and Ir{111} facets when Pd cubes and octahedra, respectively, were used as the seeds. The facet- dependent catalytic

properties of these Ir-based nanocrystals were investigated by employing them as catalysts for the selective generation of H_2 from the decomposition of hydrazine.

5.2. Results and Discussion

We started the synthesis with Pd@Ir core−shell cubes enclosed by Ir{100} facets. In a standard procedure, a solution of Na_3IrCl_6 in EG was slowly introduced (2.0 mL/h using a syringe pump) into a mixture containing poly(vinylpyrrolidone) (PVP) as a stabilizer, AA as the reductant, and Pd cubes with an edge length of 6 nm as the seeds, which had been preheated to 200 °C under magnetic stirring. The 6 nm Pd cubes encased by six {100} facets were prepared in the presence of Br^- as a capping agent using a previously reported procedure.[24] As shown by the transmission electron microscopy (TEM) images in Figure 5.1A, the Pd cubic seeds were uniform in terms of both shape and size.

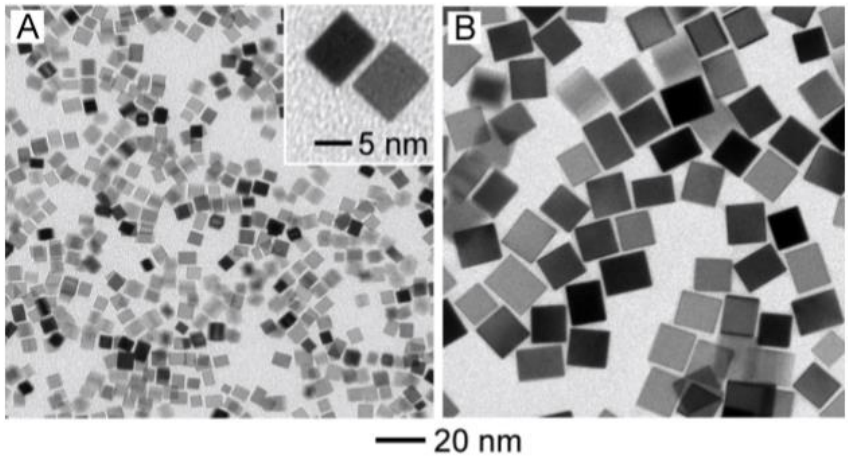

Figure 5.1. TEM images of Pd cubes with an average edge length of (A) 6 nm and (B) 18 nm that served as seeds for the growth of Ir. The inset of (A) shows a TEM image of the 6 nm Pd cube at a higher magnification.

Figure 5.2A shows a typical TEM image of the Pd@Ir core−shell cubes prepared using the standard procedure. A thin, conformal Ir shell was formed on the surface of each Pd cubic seed, and the shell can be clearly resolved due to the good contrast between Pd and Ir. It can be seen that the cubic shape of the Pd seeds was fully retained during the deposition of Ir. Our analyses on a large number of particles (>50) indicated that the Pd@Ir cubes had an average edge length of 7.5 nm, which is 1.5 nm greater than that of the initial Pd cubic seeds. Therefore, the thickness of the Ir shell on each Pd{100} facet was 0.75 nm on average. A closer examination indicates that the Pd@Ir cubes had slight truncations at the corners (red arrows in Figure 5.2A), whose appearance can be attributed to partial desorption of Br^- ions from the side faces of the Pd cubic seeds during the preheating process because of the presence of a reductant.[25] This was validated by the X-ray photoelectron spectroscopy (XPS) data shown in Figure 5.3. Without the passivation by Br^- ions, the surface free energy of Pd{100} is expected to be higher than that of Pd{111}.[16-19,25] Therefore, during the growth, Ir atoms tended to preferentially nucleate and grow on the high-energy Pd{100} facets in an attempt to reduce the total free energy of the system, resulting in truncations at the corner sites. This argument was also supported by the result that these slightly truncated Pd@Ir cubes further grew into truncated Pd@Ir cubes with an enlarged truncation area when additional Na_3IrCl_6 was added to the growth solution (Figure 5.4).

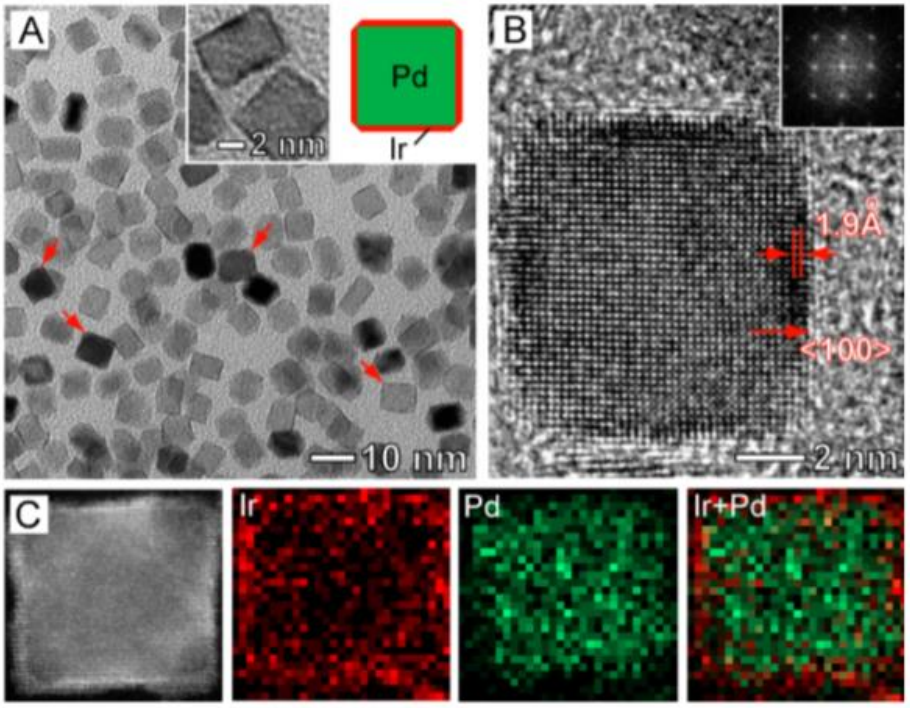

Figure 5.2. (A) TEM image of Pd@Ir core−shell cubes with slight truncations at the corners. The inset shows a TEM image taken from the same sample at a higher magnification and a 2D schematic model. Red arrows indicate slight truncations at the corner sites. (B) HRTEM image of an individual Pd@Ir cube. The inset is the corresponding FT pattern. (C) HAADF-STEM image of an individual Pd@Ir cube and EDX maps (green = Pd, red = Ir).

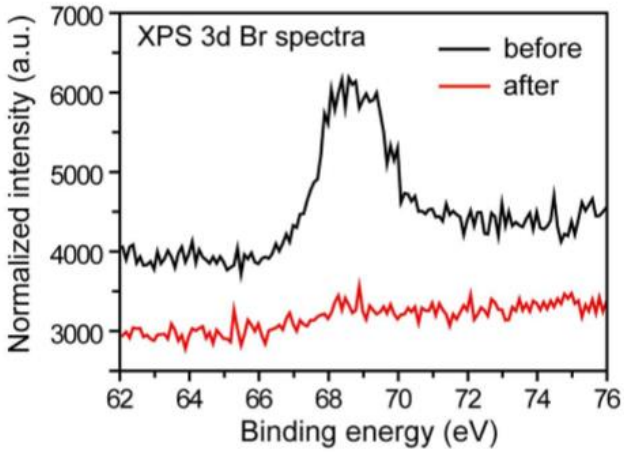

Figure 5.3. A comparison of the XPS intensities of the Br 3d peaks on the 6-nm Pd cubic seeds: the as-synthesized seeds (black curve), and the seeds subjected to pre-heating in ethylene glycol at 200 °C for 1 hour (red curve), showing that most of the Br− ions desorbed from the Pd (100) surface during the pre-heating process.

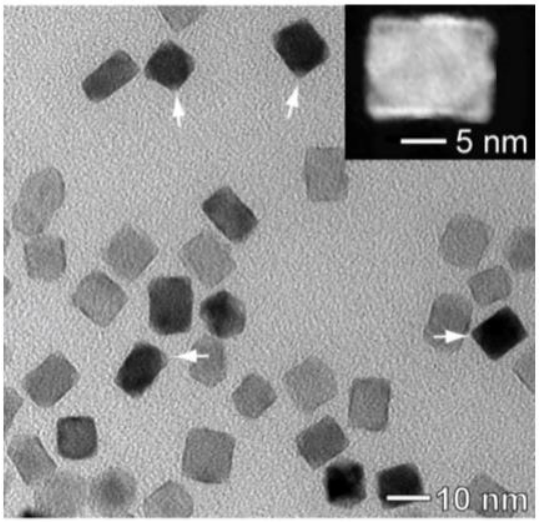

Figure 5.4. TEM image of Pd@Ir truncated cubes synthesized using the standard procedure for preparing the Pd@Ir cubes except that the total volume of the Na_3IrCl_6 solution was increased from 6 to 12 mL. The white arrows indicate the truncations at corners. The inset is a typical HAADF-STEM image taken from an individual particle.

We further characterized the structure and composition of the Pd@Ir cubes in Figure 5.2A by XPS, high-resolution TEM (HRTEM), high-angle annular dark-field scanning TEM (HAADF-STEM), and energy-dispersive X- ray (EDX) mapping. The XPS data (Figure 5.5) confirm that the shell of the Pd@Ir cubes is composed of Ir(0). The typical HRTEM image of an individual Pd@Ir cube along the [100] zone axis and the corresponding Fourier transform (FT) pattern (Figure 5.2B) clearly show the Pd@Ir cube to be bounded by Ir{100} facets. The HRTEM image also reveals the continuous lattice fringes from the Pd core to the Ir shell, indicating an epitaxial relationship between the two metals. As the lattice mismatch between Pd and Ir is only 1.3% (3.89 vs 3.84 Å), it was impossible to resolve the elemental compositions from the lattice spacing, and the interfacial strain caused by lattice mismatch can be neglected. We applied EDX analysis to examine the distributions of Pd and Ir in each core−shell cube. The EDX maps (Figure 5.2C) clearly show a color difference between the core (green = Pd) and the shell (red =

Ir), confirming that the shell was dominated by Ir while the core was essentially made of pure Pd.

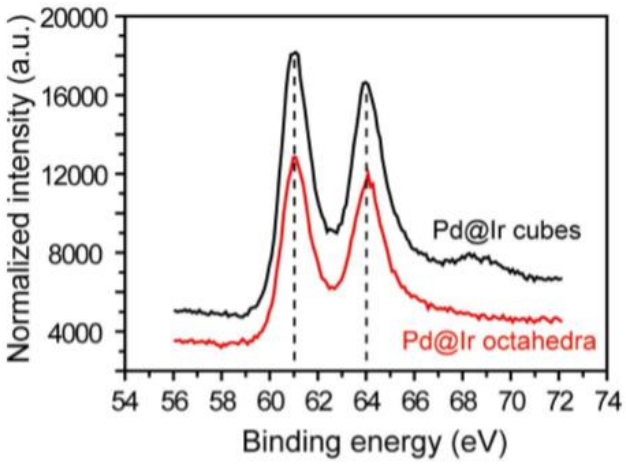

Figure 5.5. Ir 4f XPS spectra recorded from Pd@Ir core-shell cubes (as shown in Figure 5.2) and octahedra (as shown in Figure 5.9), confirming that the shells were composed of Ir(0). [26]

We believe that fast diffusion of the Ir adatoms during growth was responsible for the formation of a smooth Ir coating and thus the appearance of well-defined Ir facets in the final products. Figure 5.6A schematically illustrates two possible modes for the growth of Ir on Pd cubic seeds. The newly formed Ir atoms are expected to deposit onto the Br^--free Pd(100) surface of a cubic seed because of the relatively high surface energy of Pd{100}. Upon deposition, the Ir adatoms can migrate across the Pd surface by surface diffusion.[27] Only if the rate of surface diffusion is higher than that of atom deposition can the growth proceed by the LbL or Volmer−Weber mode, which gives rise to a smooth, conformal coating of Ir. Otherwise, the growth proceeds by the island or Frank−van der Merwe mode, resulting in the formation of irregular Ir particles on the Pd surface and thus a rough Ir shell. For the present synthesis, Na_3IrCl_6 should be immediately reduced to Ir atoms because of the strong reducing power of AA.[27] Therefore, the concentration of the

newly formed Ir atoms in the reaction solution and thereby the deposition rate of Ir is mainly determined by the rate of injection of the Na_3IrCl_6 solution, which can be tightly controlled through the use of a syringe pump.[27-29] On the other hand, the rate of surface diffusion can be conveniently varied by adjusting the reaction temperature.[27-29]

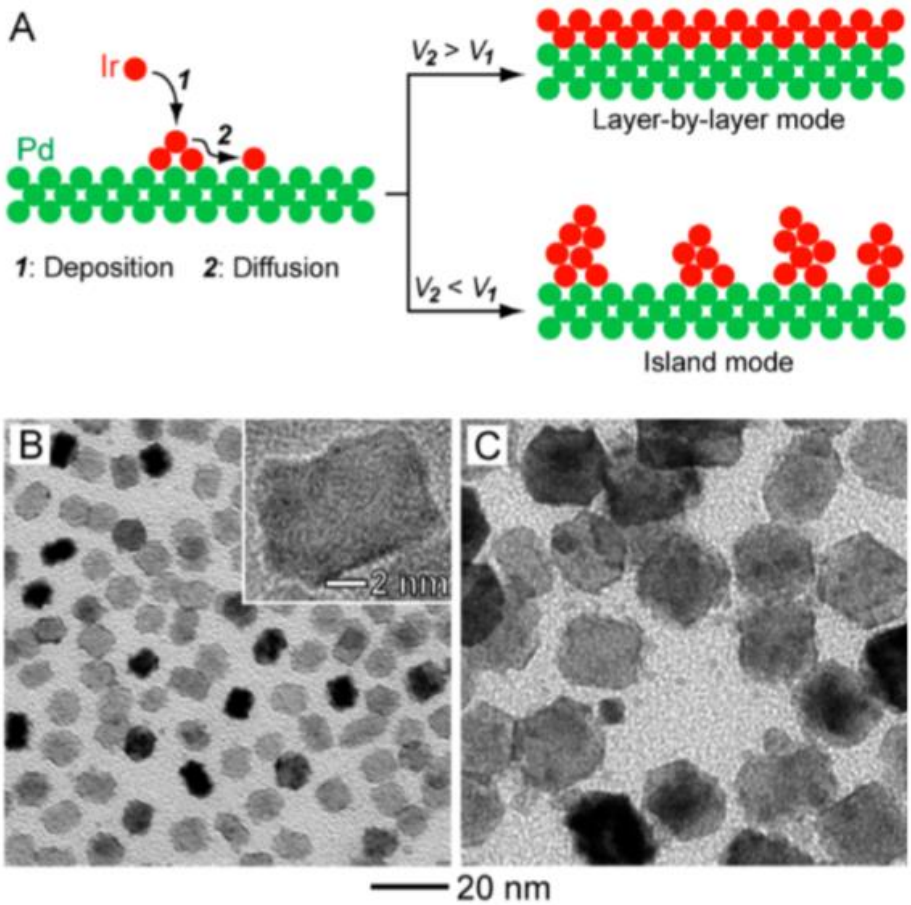

Figure 5.6. (A) Schematic illustrations of two possible modes of deposition of Ir on Pd cubic seeds. (B, C) TEM images of Pd−Ir bimetallic nanocrystals synthesized using the standard procedure for preparing the Pd@Ir cubes except that (B) the reaction temperature was decreased from 200 to 160 °C and (C) the 6 nm Pd cubic seeds were replaced with the same amount of 18 nm cubic seeds and the volume of Na_3IrCl_6 solution injected was increased from 6 to 20 mL. The inset in (B) is an HRTEM image taken from an individual particle shown in (B).

To validate our assumption, we first decreased the reaction temperature from 200 to 160 °C while keeping the Na_3IrCl_6 injection rate the same as in the standard synthesis (2.0 mL/h). In this case, the rate of surface diffusion decreased, and the Ir adatoms were

expected to stay at the deposition sites, facilitating island growth. As expected, Pd−Ir bimetallic nanocrystals with a rough surface were produced as the final products (Figure 5.6B). A similar morphology was observed when the Na_3IrCl_6 injection rate was increased from 2.0 to 8.0 mL/h while the reaction temperature was maintained at 200 °C (Figure 5.7).

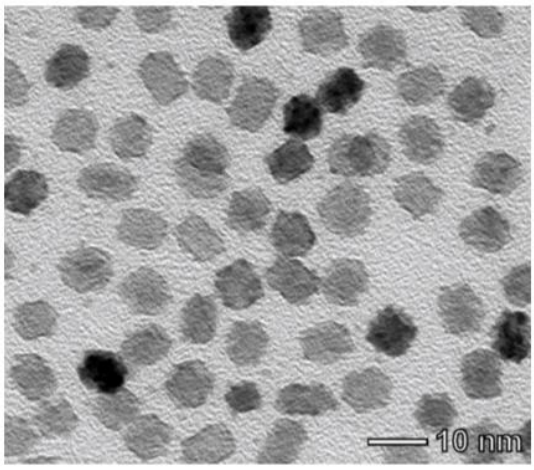

Figure 5.7. TEM images of Pd-Ir bimetallic nanocrystals synthesized using the standard procedure for preparing the Pd@Ir cubes except that the injection rate for the Na_3IrCl_6 solution was increased from 2.0 to 8.0 mL/h.

Besides the relatively high rate of surface diffusion, the small size of the Pd cubic seeds (*i.e.*, 6 nm) was also found to contribute to the LbL growth and thus the formation of a smooth, conformal Ir shell. A larger size for the Pd seeds would impose a longer travel distance for the Ir adatoms.[27] As a result, the Ir atoms could not diffuse across the entire Pd surface, leading to island growth and thus the formation of rough Ir shell. For example, Pd−Ir bimetallic nanocrystals with a rough surface were obtained when the 6 nm Pd cubes were replaced by 18 nm Pd cubes as the seeds while all of the other parameters were kept the same as in the standard synthesis except that the volume of Na_3IrCl_6 solution injected was increased from 6 to 20 mL (Figure 5.6C).

In order to obtain nanocrystals covered by Ir{111} facets, we extended the synthetic strategy from Pd cubes to Pd octahedral seeds encased by eight Pd{111} facets. The procedure for the growth of Ir on Pd octahedral seeds was the same as used for the preparation of Pd@Ir cubes except for the substitution of 6 nm Pd cubes with the same amount of 6 nm Pd octahedra. The uniform 6 nm Pd octahedral seeds (Figure 5.8) were prepared using citric acid as the capping agent for the Pd{111} facets according to a previously reported method.[13]

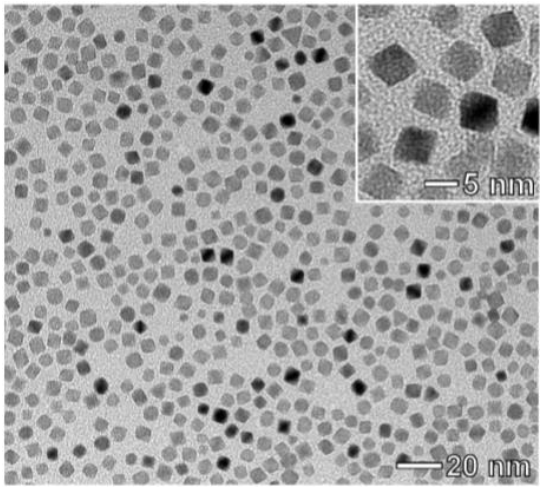

Figure 5.8. TEM images of Pd octahedra with an average edge length of 6 nm that served as the seeds for the growth of Ir. The inset shows a TEM image taken from the same sample at a higher magnification.

Figure 5.9A shows a TEM image of the as-prepared Pd@Ir core−shell octahedra with an average edge length of 7.8 nm. A thin, smooth Ir shell over the octahedral Pd core can be clearly observed (Figure 5.9A inset). The typical HRTEM image taken from an individual Pd@Ir octahedron along the [110] zone axis and the corresponding FT pattern (Figure 5.9B) indicate the exposure of Ir{111} facets on the surface. The core−shell structure was confirmed by the EDX maps (Figure 5.9C; green = Pd, red = Ir). It is worth

pointing out that LbL growth in this case was still maintained even when the reaction temperature was decreased from 200 to 160 °C (Figure 5.10A), which is different from the case of Pd cubic seeds (Figure 5.6B). When the reaction temperature was further decreased to 120 °C, the growth was switched to the island mode (Figure 5.10B).

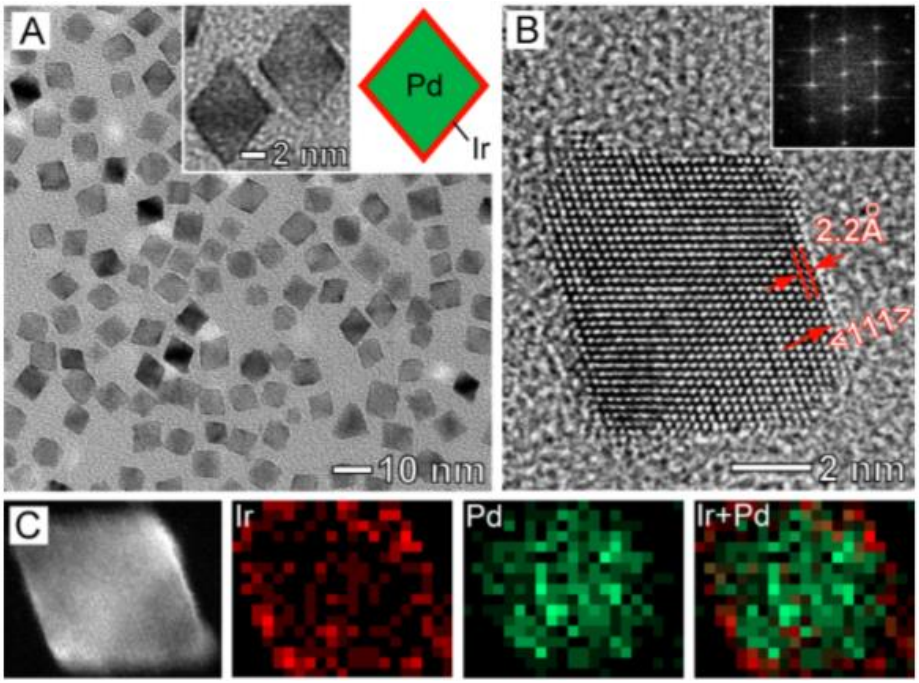

Figure 5.9. (A) TEM image of Pd@Ir core–shell octahedra. The inset shows a TEM image taken from the same sample at a higher magnification and a 2D schematic model. (B) HRTEM image of an individual Pd@Ir octahedron. The inset is the corresponding FT pattern. (C) HAADF-STEM image of an individual Pd@Ir octahedron together with EDX maps (green = Pd, red = Ir).

These results indicate that the diffusion rate of Ir adatoms on the Pd(111) surface was higher than on Pd(100) surface at the same temperature. Such a higher diffusion rate can be ascribed to the relatively lower energy barrier for the diffusion of Ir adatoms (E_{diff}) on the Pd(111) surface. In general, a close- packed crystallographic plane such as (111) has a relatively smoother surface and thus a lower E_{diff} than a loose-packed plane with an open structure such as (100) or (110).[30,31] For example, it was shown that the value of E_{diff}

for the diffusion of Rh adatoms is 0.16 eV on the Rh(111) surface and increases to 0.60 and 0.88 eV for Rh(110) and Rh(100), respectively.[30]

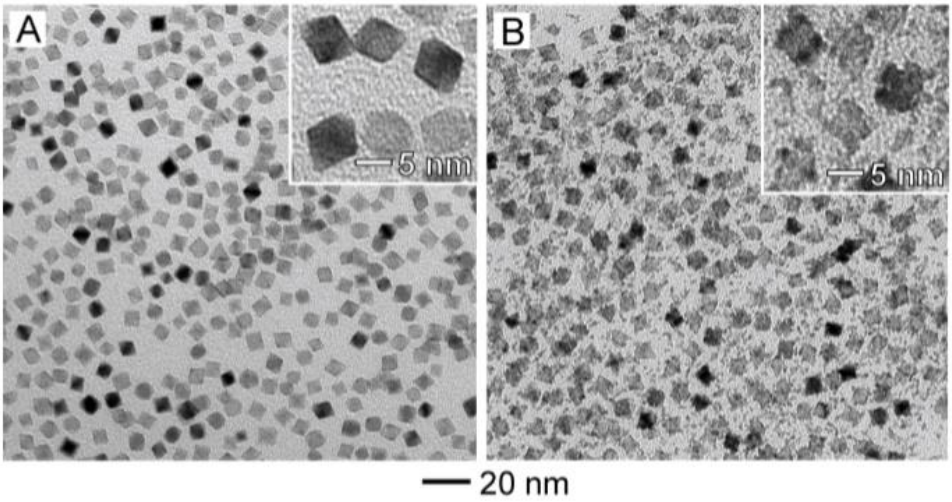

Figure 5.10. TEM images of Pd-Ir bimetallic nanocrystals synthesized using the procedure for preparing the Pd@Ir octahedra except that the reaction temperature was decreased from 200 °C to (A) 160 °C and (B) 120 °C. The insets show TEM images taken from the same samples at a higher magnification.

Another interesting finding for the growth of Ir on Pd octahedral seeds was that further increasing the volume of Ir precursor solution from 6 to 12 mL (Figure 5.11) did not result in an increase in the thickness of the Ir shell. Instead, small Ir particles with irregular shapes due to homogeneous nucleation and growth started to appear in the product. This result implies that in the present system the energy barrier for further deposition of Ir atoms on the Ir{111}-covered octahedra is higher than that for the self-nucleation of Ir. We also observed a similar phenomenon, known as self-termination for the growth of the (111) surface, on Pd and Ag octahedra.[32,33]

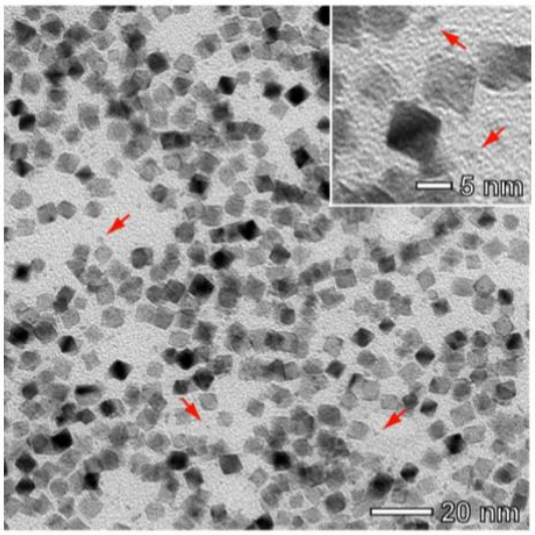

Figure 5.11. TEM images of nanocrystals synthesized using the standard procedure for preparing the Pd@Ir octahedra except that the volume of Na3IrCl6 solution was increased from 6 to 12 mL. In addition to the formation of Pd@Ir octahedra, there were a lot of small Ir nanoparticles 1-2 nm in size (as indicated by the red arrows) that were formed through homogeneous nucleation. The inset shows a TEM image taken from the same sample at a higher magnification.

Finally, we investigated the facet-dependent catalytic properties of the as-prepared Pd@Ir nanocrystals using selective H_2 generation via the decomposition of hydrous hydrazine as a model catalytic reaction. H_2 generation is at the core of hydrogen fuel cell technology. Hydrous hydrazine, $H_2NNH_2 \cdot H_2O$, is one of the safest and most efficient hydrogen storage materials, with a hydrogen content as high as 7.9 wt %. [34] It is known that the decomposition of hydrazine has a strong dependence on the type of catalyst used and the reaction conditions. [35] In general, hydrazine can be decomposed in two ways: completely ($H_2NNH_2 \rightarrow N_2 + 2H_2$) and incompletely ($3\ H_2NNH_2 \rightarrow 4NH_3 + N_2$). Nanoparticles based on Ir were found to be effective in catalyzing the decomposition of hydrazine and the generation of H_2.[37] Obviously, maximizing the H_2 selectivity for Ir nanocrystals by engineering its surface is expected to be an effective approach to reduce the loading of precious Ir and, at the same time, more efficiently utilize the hydrogen

storage material. Nevertheless, it has been extremely difficult to study this subject since essentially none of the reported Ir nanocrystals possess a well-defined shape. The Pd@Ir cubes (Figure 5.2) and octahedra (Figure 5.9) covered by Ir{100} and Ir{111} facets, respectively, enabled us to investigate the facet-dependent catalytic properties of Ir nanocrystals toward the decomposition of hydrazine. For comparison, we also prepared Pd@Ir cuboctahedra encased by a mixture of Ir{100} and Ir{111} facets by coating Pd nanospheres with smooth Ir shells (see Figure 5.12 for details).

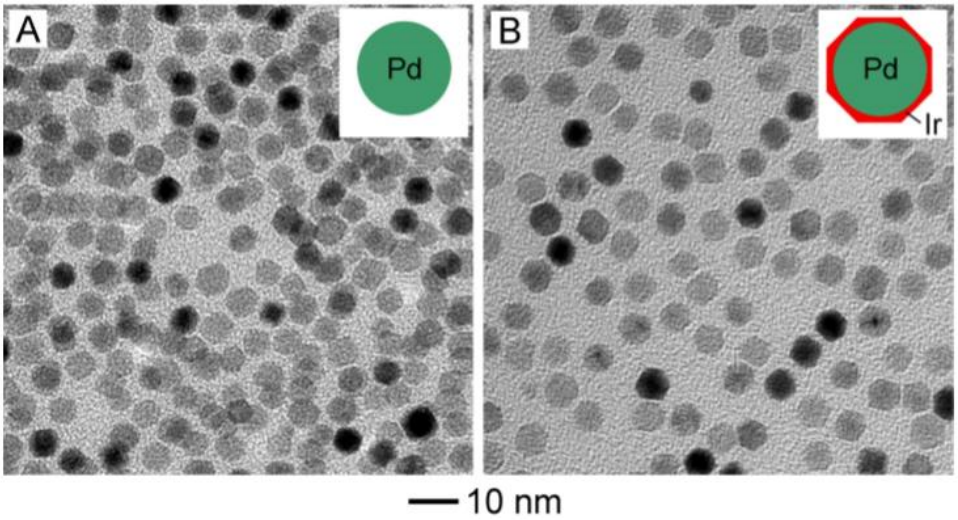

Figure 5.12. TEM images of (A) Pd nanospheres with an average diameter of 5 nm that were used as the seeds and (B) the corresponding Pd@Ir core-shell cuboctahedra grown from the 5-nm spherical seeds. The procedure for the preparation of Pd@Ir cuboctahedra was the same as the standard procedure for the Pd@Ir cubes except for the substitution of 6-nm Pd cubes with the same amount of 5-nm Pd nanospheres as the seeds and the decrease of injection volume for Na3IrCl6 solution from 6 mL to 4 mL. The insets show the corresponding 2D models for each sample.

As shown in Figure 5.13, all the three types of Pd@Ir core–shell nanocrystals showed catalytic activity toward the decomposition of hydrazine, while essentially no activities were observed for the corresponding Pd seeds. The molar ratios of generated H_2 + N_2 to initially added hydrazine were 1.18, 0.73, and 0.57 for the Pd@Ir cubes, cuboctahedra, and octahedra, respectively, corresponding to H_2 selectivities of 31.8%,

14.9%, and 8.9% (see the SI for details). These results indicate that the Ir(100) surface has a much higher H_2 selectivity than the Ir(111) surface toward the decomposition of hydrazine. On the basis of previous reports,[37,38] the decomposition of hydrazine into N_2 and H_2 on the Ir surface involves a series of steps, including decomposition of adsorbed N_2H_4 into NH_2, splitting of NH_2 into N and H atoms, combination of N and H atoms into N_2 and H_2 molecules, respectively, and finally the desorption of N_2 and H_2 molecules from the Ir surface as gas products. Thus, the observed higher H_2 selectivity for the Ir(100) surface might be attributed to its higher efficiency in facilitating the aforementioned reaction steps compared with the Ir(111) surface. In the future, componential calculations might advance our mechanistic understanding of this catalytic reaction.

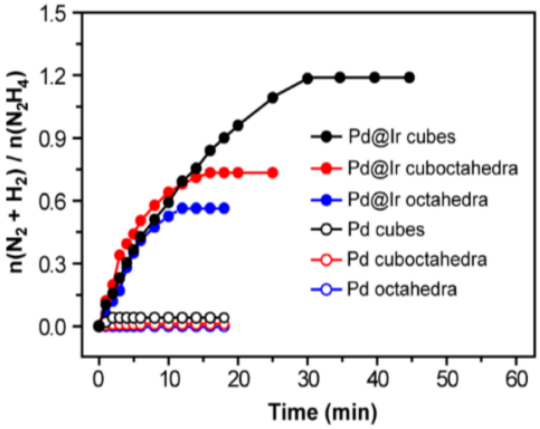

Figure 5.13. Time course plots for the decomposition of hydrous hydrazine catalyzed by different nanocrystals at room temperature. The y axis is the molar ratio of N_2 + H_2 produced from the reaction to the initially added hydrazine. Each data point represents the average of three independent measurements.

5.3 Conclusion to Chapter 5

In summary, we have demonstrated a facile method based on seed-mediated growth for the synthesis of Ir nanocrystals with well-controlled facets. The essence of this approach is to coat Pd seeds having a well-defined shape with conformal Ir shells to ensure

the replication of atomic arrangements on the surface. Both Pd@Ir core–shell cubes and octahedra, enclosed by Ir{100} and Ir{111} facets, respectively, were successfully prepared by using Pd cubes and octahedra as the seeds. The key to the success of this synthesis is to accelerate the rate of surface diffusion for the deposited Ir atoms by increasing the reaction temperature. In comparison with the Ir{111}-covered octahedra, the Ir{100}-covered cubes exhibited a much higher H_2 selectivity toward the decomposition of hydrazine. This work represents the first successful attempt for facet-controlled synthesis of Ir nanocrystals. We believe that the synthetic strategy reported here can also be extended to the synthesis of Ir nanocrystals with other facets by using Pd nanocrystals of different shapes as the seeds.

5.5 Experimental Section

Chemicals and Reagents. Ethylene glycol (EG, lot no. G32B27) was obtained from J. T. Baker. Sodium hexachloroiridate(III) hydrate ($Na_3IrCl_6 \cdot xH_2O$, MW=473.90), citric acid (CA, ≥99.5%), sodium tetrachloropalladate(II) (Na_2PdCl_4, 98%), potassium bromide (KBr, ≥99.0%), L-ascorbic acid (AA, ≥99.0%), and poly(vinyl pyrrolidone) (PVP, MW≈55,000) were all obtained from Sigma-Aldrich. All aqueous solutions were prepared using deionized (DI) water with a resistivity of 18.2 MΩ·cm.

Preparation of Pd seeds. i) 6-nm and 18-nm Pd cubes to be used as seeds. The Pd cubic seeds were synthesized according to a previously reported procedure. [39] In brief, 8.0 mL of an aqueous solution containing 105 mg of PVP, 60 mg of AA, and different amounts of KBr and KCl (5 mg of KBr + 185 mg of KCl for 6-nm cubic seeds; 600 mg of KBr for 18-nm cubic seeds) was hosted in a vial and preheated to 80 °C in an oil bath under magnetic

stirring for 10 min. Subsequently, 3.0 mL of an aqueous solution containing 57 mg of Na_2PdCl_4 was added with a pipette. After the vial had been capped, the reaction was allowed to continue at 80 °C for 3 h. After being washed with DI water three times via centrifugation, the Pd cubic seeds were stored in 5 mL of EG for future use (~4.0 mg/mL in Pd element). ii) 6-nm Pd octahedra to be used as seeds. The 6-nm Pd octahedral seeds were prepared using a previously reported procedure with slight modifications. [38] In a typical synthesis, 8 mL of water/ethanol mixture solution (5 mL water and 3 mL ethanol) containing 105 mg of PVP and 180 mg of CA was hosted in a vial and preheated to 80 °C in an oil bath under magnetic stirring for 10 min. Then, 3.0 mL of an aqueous solution containing 57 mg of Na_2PdCl_4 was added with a pipette. The reaction was allowed to continue at 80 °C for 3 h. After being washed with DI water for three times via centrifugation, the final product was dispersed in 5 mL of EG for future use (~4.0 mg/mL in Pd element). iii) 5-nm Pd nanospheres to be used as seeds. In a typical synthesis, 2 mL of an EG solution containing 30 mg of PVP was hosted in a vial and preheated to 160 °C in an oil bath under magnetic stirring for 10 min. Then, 1.5 mL of an EG solution containing 16 mg of Na_2PdCl_4 was quickly added to the reaction solution with a pipette. The reaction was allowed to continue at 160 °C for 3 h. After being washed with acetone once and DI water for three times via centrifugation, the final product was dispersed in 1.4 mL of EG for future use (~4.0 mg/mL in Pd element).

Standard procedure for the synthesis of Pd@Ir core-shell cubes. In a standard procedure, 10 mL of an EG solution containing 100 mg of PVP and 60 mg of AA was hosted in a 25-mL three-neck flask and preheated to 100 °C in an oil bath under magnetic stirring for 1 h. Then, 0.8 mL of the 6-nm Pd cubic seeds was added to the flask using a

pipette. The reaction temperature was ramped to 200 °C after the addition of seeds. Immediately after the temperature had reached 200 °C, 6.0 mL of $Na_3IrCl_6 \cdot xH_2O$ solution (0.5 mg/mL, in EG) was injected to the flask at a rate of 2.0 mL/h using a syringe pump. The reaction was allowed to proceed for an additional 10 min after the Na_3IrCl_6 precursor had been completed injected. The products were collected by centrifugation, washed once with acetone, three times with water, and finally redispersed in 0.8 mL of DI water. The procedures for preparing other types of Pd-Ir bimetallic nanocrystals were the same as this standard procedure for Pd@Ir cubes except for the minor changes as indicated in the text.

Catalytic decomposition of hydrazine monohydrate. i) Protocol for the catalytic reaction. The catalytic reactions were carried out according to the protocol reported by Xu and coworkers with minor modifications. [36] Typically, 0.4 mL of an aqueous suspension of the Pd-Ir bimetallic nanocrystals and 10 μL of hydrazine monohydrate were sequentially added into a two-neck flask kept at room temperature (ca. 22 °C) under magnetic stirring, with one of the openings connected to a gas burette. The gases produced from the flask were passed through a trap containing 100 mL of hydrochloric acid (1.0 M) to ensure the complete removal of ammonia. The volume of the remaining gases was recorded using the gas burette. ii) Calculation of the H_2 selectivity. [38] In general, hydrazine can be decomposed to generate a mixture of N_2 and H_2 (Eq. 1) or a mixture of NH_3 and N_2 (Eq. 2). Given that *x* represents the H_2 selectivity of a catalyst, the combined reaction for (1) and (2) can be expressed as Eq. (3), from which *x* can be expressed and derived as Eqs. (4) and (5). Since NH_3 is removed from the gas mixture, the molar amount of N_2 and H_2 can be easily calculated using the ideal gas law (Eq. (6)). Collectively, the value of *x* can be experimentally derived from Eq. (5) by measuring the volume of produced H_2 and N_2:

$$N_2H_4 \rightarrow N_2 + H_2 \quad (1)$$

$$3N_2H_4 \rightarrow N_2 + 4NH_3 \quad (2)$$

$$3N_2H_4 \rightarrow 4(1-x)NH_3 + (1+2x)N_2 + 6xH_2 \quad (3)$$

$$n(N_2 + H_2)/n(N_2H_4) = [(1+2x) + 6x]/3 \quad (4)$$

$$x = \left(\left[3n\,(N_2 + H_2)/n(N_2H_4) - 1 \right]/8 \right) \times 100 \quad (5)$$

$$PV = n(N_2 + H_2)RT \quad (6)$$

Characterizations. The transmission electron microscope (TEM) images were taken using a Hitachi-HT7700 microscope (Hitachi, Tokyo, Japan) operated at 120 kV. The X-ray photoelectron microscopy (XPS) data were recorded using a Thermo K-Alpha spectrometer with an Al Kα source (eV). High-resolution TEM (HRTEM) images, high-angle annular dark-field scanning TEM (HAADF-STEM) images and energy dispersive X-ray (EDX) mapping were acquired using a double Cs-corrected JEOL ARM200F TEM at Brookhaven National Laboratory.

5.5 Notes to Chapter 5

This chapter was adapted from "Facile Synthesis of Iridium Nanocrystals with Well-Controlled Facets Using Seed-Mediated Growth" published in the *Journal of the American Chemical Society*. [40]

5.6 References

[1] Ertl, G. *Handbook of Heterogeneous Catalysis*; Wiley-VCH: Weinheim, Germany, **2008**.

[2] Zhang, H.; Jin, M.; Xiong, Y.; Lim, B.; Xia, Y. *Acc. Chem. Res.* **2013**, *46*, 1783.

[3] Tian, N.; Zhou, Z.; Sun, S.; Ding, Y.; Wang, Z. *Science* **2007**, *316*, 732.

[4] Lim, B.; Jiang, M.; Camargo, P. H. C.; Cho, E. C.; Tao, J.; Lu, X.; Zhu, Y.; Xia, Y. *Science* **2009**, *324*, 1302.

[5] Nishihata, Y.; Mizuki, J.; Akao, T.; Tanaka, H.; Uenishi, M.; Kimura, M.; Okamoto, T.; Hamada, N. *Nature* **2002**, *418*, 164.

[6] Kim, S.-W.; Kim, M.; Lee, W. Y.; Hyeon, T. *J. Am. Chem. Soc.* **2002**, *124*, 7642.

[7] Grass, M. E.; Zhang, Y. W.; Butcher, D. R.; Park, J. Y.; Li, Y. M.; Bluhm, H.; Bratlie, K. M.; Zhang, T. F.; Somorjai, G. A. *Angew. Chem., Int. Ed.* **2008**, *47*, 8893.

[8] Vidal-Iglesias, F. J.; Solla- Gulloń , J.; Montiel, V.; Feliu, J. M.; Aldaz, A. J. *Power Sources* **2007**, *171*, 448.

[9] Narayanan, R.; El-Sayed, M. A. *Nano Lett.* **2004**, *4*, 1343.

[10] Langille, M. R.; Personick, M. L.; Zhang, J.; Mirkin, C. A. *J. Am. Chem. Soc.* **2012**, *134*, 14542.

[11] Guo, S.; Zhang, S.; Sun, S. *Angew. Chem., Int. Ed.* **2013**, *52*, 8526.

[12] Xie, S.; Choi, S.-I.; Xia, X.; Xia, Y. *Curr. Opin. Chem. Eng.* **2013**, *2*, 142.

[13] Shao, M.; Yu, T.; Odell, J. H.; Jin, M.; Xia, Y. *Chem. Commun.* **2011**, *47*, 6566.

[14] Bratlie, K. M.; Kilewer, C. J.; Somorjai, G. A. *J. Phys. Chem. B* **2006**, *110*, 17925.

[15] Jin, R. *Nanotechnol. Rev.* **2012**, *1*, 31.

[16] Xia, Y.; Xiong, Y.; Lim, B.; Skrabalak, S. E. *Angew. Chem., Int. Ed.* **2009**, *48*, 60.

[17] Ahmadi, T. S.; Wang, Z. L.; Green, T. C.; Henglein, A.; El-Sayed, M. A. *Science* **1996**, *272*, 1924.

[18] Chen, M.; Wu, B.; Yang, J.; Zheng, N. *Adv. Mater*. **2012**, *24*, 862.

[19] Sneed, B. T.; Kuo, C. H.; Brodsky, C. N.; Tsung, C.-K. *J. Am. Chem. Soc.* **2012**, *134*, 18417.

[20] Stowell, C. A.; Korgel, B. A. *Nano Lett.* **2005**, *5*, 1203.

[21] Fonseca, G. S.; Umpierre, A. P.; Fichtner, P. F. P.; Teixeira, S. R.; Dupont, *J. Chem.*

Eur. J. **2003**, *9*, 3263.

[22] Zhang, Y.; Zhang, H.; Zhang, Y.; Ma, Y.; Zhong, H.; Ma, H. *Chem. Commun.* **2009**, 6589.

[23] Rueping, M.; Koenigs, R. M.; Borrmann, R.; Zoller, J.; Weirich, T. E.; Mayer, *J. Chem. Mater.* **2011**, *23*, 2008.

[24] Jin, M.; Liu, H.; Zhang, H.; Xie, Z.; Liu, J.; Xia, Y. *Nano Res.* **2011**, *4*, 83.

[25] Peng, H.-C.; Xie, S.; Park, J.; Xia, X.; Xia, Y. *J. Am. Chem. Soc.* 2013, *135*, 3780.

[26] Peuckert, M. *Surf. Sci.* **1984**, *144*, 451.

[27] Xia, X.; Xie, S.; Liu, M.; Peng, H.-C.; Lu, N.; Wang, J.; Kim, M. J.; Xia, Y. *Proc. Natl. Acad. Sci. U.S.A.* **2013**, *110*, 6669.

[28] Xie, S.; Peng, H.-C.; Lu, N.; Wang, J.; Kim, M.; Xie, Z.; Xia, Y. *J. Am. Chem. Soc.* **2013**, *135*, 16658.

[29] Xie, S.; Choi, S.-I.; Lu, N.; Roling, L. T.; Herron, J. A.; Zhang, L.; Park, J.; Wang, J.; Kim, M. J.; Xie, Z.; Mavrikakis, M.; Xia, Y. *Nano Lett.* **2014**, *14*, 3570.

[30] Oura, K.; Lifshits, V. G.; Saranin, A.; Zotov, A. V.; Katayama, M. *Surface Science: An Introduction*; Springer: Berlin, **2003**; p 333.

[31] Shustorovich, E. *Metal-Surface Reaction Energetics: Theory and Applications to Heteroge- neous Catalysis, Chemisorption, and Surface Diffusion;* Ed.; Wiley-VCH: Weinheim, Germany, **1991**; p 114.

[32] Jin, M.; Zhang, H.; Xie, Z.; Xia, Y. *Energy Environ. Sci.* **2012**, *5*, 6352.

[33] Wang, Y.; Wan, D.; Xie, S.; Xia, X.; Huang, C. Z.; Xia, Y. *ACS Nano* **2013**, *7*, 4586.

[34] Schmidt, E. W. *Hydrazine and its Derivatives: Preparation, Properties, Applications*, 2nd ed.; Wiley: New York, **1984**.

[35] Singh, S. K.; Zhang, X.-B.; Xu, Q. *J. Am. Chem. Soc.* **2009**, *131*, 9894.

[36] Singh, S. K.; Xu, Q. *J. Am. Chem. Soc.* **2009**, *131*, 18032.

[37] Contour, J. P.; Pannetier, G. J. *Catal.* **1972**, *24*, 434.

[38] Liu, M.; Zheng, Y.; Xie, S.; Li, N.; Lu, N.; Wang, J.; Kim, M. J.; Guo, L.; Xia, Y. *Phys. Chem. Chem. Phys.* **2013**, *15*, 11822.

[39] Jin, M.; Liu, H.; Zhang, H.; Xie, Z.; Liu, J.; Xia, Y. *Nano Research* **2011**, *4*, 83.

[40] X. Xia, L. Figueroa-Cosme, J. Tao, H.-C. Peng, G. niu, Y. Zhu, Y. Xia, *J. Am. Chem. Soc.* **2014**, *136*, 10878.

CHAPTER 6

CONCLUSIONS AND FUTURE DIRECTIONS

6.1 Concluding Remarks

This dissertation covers a number of strategies for controlling the size and shape of noble-metal nanocrystals, as well as explores scale-up strategies for the commercialization of such nanomaterials. In the first project, I developed a simple and robust method for the synthesis of Pd nanoplates using hydroxylamine as the reducing agent. By characterizing the products obtained at different time points, I found that the internal defect structure of the Pd nanoplates was formed at the early stage of a synthesis, which provided seeds with stacking-faults for the subsequent growth into highly anisotropic, planar, well-defined hexagonal nanoplates. It is reasonable to consider this synthesis a *robust* one because I found that rather drastic changes to the experimental parameters such as pH, temperature, and chemical environment did not significantly alter the nucleation process (*i.e.*, formation of internal defect structure) and overall shape (*i.e.*, hexagonal) of the final products. The protocol could even be adapted for a continuous flow reactor to scale up the production of high-quality Pd nanoplates.

In my next project, I developed a strategy that separates the nucleation and growth processes during a one-pot synthesis of Pd nanocrystals. In this work, I intentionally introduced two reductants with very different reducing powers to regulate both the production of seeds, and the necessary growth to produce Pd octahedra. The strong reductant was used to control the initial reduction and nucleation to form single-crystal seeds, while the weak reductant was used for both the slow reduction of unreacted precursor and the stabilization of the resultant {111} facets. To illustrate the generality of

this approach, I evaluated four pairs of strong-weak reductants and demonstrated that Pd octahedra could be obtained in good quality for all cases. In contrast, when the reductants was used individually, the products were polydispersed in terms of both size and shape.

In my third project, I introduced a new perspective on increasing the volume of production during a synthesis of colloidal nanocrystals *via* seed-mediated growth. By taking advantage of stoichiometry, I demonstrated the capability to increase the volume of production of Pd octahedra with different sizes from *ca.* 2 mg to over 500 mg. I performed both geometric and stoichiometric analyses to calculate the minimum amount of reagents needed for the complete growth of a Pd cubic seed into its dual polyhedron. I could avoid homogeneous nucleation by minimizing the amount of Pd atoms formed during the growth process while retaining a good control over the shape of the nanocrystals. I successfully extended the approach to the synthesis of Pd@$Pt_{3–4L}$ octahedra, which were subsequently tested as catalysts toward oxygen reduction. The Pd@$Pt_{3–4L}$ octahedra prepared using a 10-fold scaled-up synthesis demonstrated a 3-fold increase in both the specific and mass activity toward ORR relative to the commercial Pt/C catalyst.

Finally, my coworkers and I have demonstrated a facile method based on seed-mediated growth for the synthesis of Ir nanocrystals with well-controlled facets. The essence of this approach was to deposit conformal Ir shells onto the surface of Pd seeds to replicate the atomic arrangements of the surface and obtain well-defined Ir nanocrystals. Both Pd@Ir core−shell cubes and octahedra, enclosed by Ir{100} and Ir{111} facets, respectively, were successfully prepared by using Pd cubes and octahedra as the seeds. The key to the success of this synthesis was to accelerate the rate of surface diffusion for the deposited Ir atoms by increasing the reaction temperature. We further evaluated the H_2

selectivity toward the decomposition of hydrazine and found that the Ir{111}-covered octahedra exhibited a much higher selectivity than the Ir{100}-covered cubes.

In all, my research has provided both, mechanistic insights into the nucleation and growth of noble-metal nanocrystals, and approaches that could further improve the commercial viability of these nanomaterials. The methods presented here for the synthesis of Pd nanocrystals are simple, robust, and scalable, while allowing a good control over the nanocrystal's shape. Lastly, this work enhances our understanding of structure-property relationship for Ir nanocrystals, where the shape-dependent catalytic properties have not been explored.

6.2 Future Direction

The research described in this dissertation seek to simplify and, to a certain extent, guide the rational design of metal-based nanocrystals, in an effort to scale up the production of these materials. Despite the success in recent years, there are still open questions that need to be investigated.

First, the work presented above encourages the development of new one-pot approaches to the synthesis of metal nanocrystals with controlled shapes. However, extensive work remains to be done to elucidate the mechanisms of the dual-reductant approach. Understanding the reduction kinetics can direct crystal growth to obtain specific morphologies, and lead to the design and synthesis of a myriad of well-controlled shapes for colloidal nanocrystals.[1,2] The reduction mechanism of individual reductants will be altered when several reductants are present simultaneously in the same reaction system. Therefore, in-depth kinetic studies should be conducted in the future to gain a quantitative

understanding of the reduction mechanism, and to optimize experimental parameters to optimize the amount of particles with a specific internal defect structure. Moreover, given the complexity of the system, the redox reactions between the metal precursor and two reductants could exhibit second, third or even higher order kinetics, which invalidates commonly used approximations such as the pseudo-first order approximation. Therefore, additional studies and more complex data analysis methods (*i.e.*, the Finke-Watzky mechanism)[4-5] should be developed and/or employed to accurately determine the kinetic and thermodynamic parameters. In some cases, UV/vis cannot be used alone to track the concentration of a given metal precursor, so inductively-coupled plasma mass spectrometry (ICP-MS) may be necessary to quantify the reduction kinetics.

The mechanisms that govern the homogeneous nucleation of both stacking-fault-lined structures and other unique defect-containing nanocrystals, are yet to be elucidated. Most of the methods for the synthesis of such structures are far from simple due to the involvement of gases like CO, or long reaction times. The method presented here for nanoplates can serve as a model reaction for future experiments, with an aim to elucidate the mysterious mechanisms for the formation of plates. Specifically, elucidating the oxidation mechanism of hydroxylamine and the byproducts such as N_2O generated during the reaction, could lead to insights regarding the mechanism of formation for nanoplates.

I would like to conclude my dissertation by inviting the scientific community to take a step back from their research and reflect on the extent and impact of their results towards our society. The discovery and development of nanotechnology created a new perspective on the world. For instance, we have smaller, faster, and better transistors that are responsible for information storage.[6-9] Ultra-high definition displays and

televisions are now being sold utilizing quantum dots to produce more vibrant colors while being more energy efficient.[6-9] Nanotechnology is improving the efficiency of fuel production from raw petroleum materials through better catalysis, and it is also enabling reduced fuel consumption in vehicles and power plants through higher-efficiency combustion and decreased friction.[6-9] In the field of medicine, nanoparticles are used as therapeutic or imaging agents in clinical trials in an effort to control the biodistribution, enhance the efficacy, or otherwise reduce toxicity of a drug or biologic.[10-12]

Indeed, nanotechnology is helping to considerably improve our lives, yet we could and we should do better. There is still an enormous gap between academic studies and the practical use of shape-controlled nanocrystals. We have developed complex methods to synthesize any shape possible, however these unique materials have not truly been exploited in applications. We should encourage the identification of current problems together with the development of ideas that can promote the utilization of these nanomaterials to improve lives. As a scientific community, we owe this to the tax payers who every year contributes financially to the advancement of science through organizations such as the National Science Foundation, the National Institute of Health, the Department of Energy, and Department of Homeland Security, among many others. After all, the most noble accomplishment that a scientist could ever achieve will always be *to do something useful.*

6.3 References

[1] Gilroy, K. D.; Ruditskiy, A.; Peng, H.-C.; Qin, D.; Xia, Y. *Chem. Rev.* **2016,** *116,* 10414-10472.

[2] Xia, Y.; Gilroy, K. D.; Peng, H.-C.; Xia, X. *Angew. Chem. Int. Ed.* **2017,** *56,* 60-95.

[3] T.-H. Yang, H.-C. Peng, S. Zhou, C.-T. Lee, S. Bao, Y.-H. Lee, J.-M. Wu, Y. Xia, *Nano Lett.* 2017, *17*, 334–340.

[4] M. A. Watzky, R. G. Finke. *J. Am. Chem. Soc.* 1997, *119*, 10382−10400.

[5] M. A. Watzky, E. E. Finney, R. G. Finke. *J. Am. Chem. Soc.* 2008, *130*, 11959−11969.

[6] https://www.nano.gov/you/nanotechnology-benefits

[7] https://www.asme.org/engineering-topics/articles/technology-and-society/10-ways-nanotechnology-impacts-lives

[8] H. Kind, H. Yan, B. Messer, M. Law, P. Yang, Adv. Mater. **2002**, *14*, 158–160.

[9] A. D. Franklin, M. Luisier, S.-J. Han, G. Tulevski, C. M. Breslin, L. Gignac, M. S. Lundstrom, W. Haensch, Nano Lett. **2012**, *12*, 758–762.

[10] D. Bobo, K. J. Robinson, J. Islam, K. J. Thurecht, S. R. Corrie, *Pharmaceutical Research*, **2016**, *33*, 2373–2387.

[11] A. C. Eifler, C. S. Thaxton, *Biomedical Nanotechnology*, **20111**, *726*, 325–338.

[12] https://inchemistry.acs.org/content/inchemistry/en/acs-and-you/el-sayed